POWER TRANSFORMER OVERHEATING DUE TO GEOMAGNETICALLY-INDUCED CURRENTS

A THESIS SUBMITTED TO
THE FACULTY OF GRADUATE STUDIES
IN PARTIAL FULFILLMENT
OF THE REQUIREMENTS FOR THE DEGREE
DOCTOR OF PHILOSOPHY

BY
HOCK CHUAN TAY
DEPARTMENT OF ELECTRICAL ENGINEERING
THE UNIVERSITY OF MANITOBA
WINNIPEG, CANADA

JANUARY 1983

POWER TRANSFORMER OVERHEATING DUE TO GEOMAGNETICALLY-INDUCED CURRENTS

BY

HOCK CHUAN TAY

A thesis submitted to the Faculty of Graduate Studies of the University of Manitoba in partial fulfillment of the requirements of the degree of

DOCTOR OF PHILOSOPHY

ABSTRACT

This thesis concerns power transformer overheating due to (near dc) geomagnetically-induced currents (GIC).

In order to understand how the magnetic field behaves when an iron core is in deep saturation under GIC conditions, the field of a deeply saturated two-dimensional soft-iron ring is examined in detail using the well-known finite-element Newton-Raphson numerical technique. The governing nonlinear vector-potential field equation used in the field calculations is derived from Maxwell's equations. The analysis adopts higher order isoparametric elements for improvement in accuracy of the results. The nonlinearity of the iron characteristic is fully accounted for in this study. This is accomplished by using the cubic spline method for modelling the entire reluctivity curve of the iron. A special feature is also added whereby the field due to the magnetized iron itself can be examined in detail.

The deep saturation condition, the nonlinearity of the iron core under ac plus dc excitation conditions, and the limited applicability of magnetic circuit theory to an iron circuit under deep saturation conditions make quantitative analysis of the problem almost impossible. In view of this difficulty, experimental investigations were emphasized. These include Hall-effect flux probe measurements, true power and true rms exciting current measurements, and temperature measurements. Experimental data are analysed in conjunction with knowledge gained from the study of the field behaviour

of a deeply saturated iron ring.

A device based on the sensing of a unique symptom of power transformer behavior under GIC conditions has also been designed and tested on the Manitoba Hydro System. The demonstration of the slow rate-of-rise of sufficiently high 2nd-harmonic current is also included.

ACKNOWLEDGEMENTS

I wish to express my deep appreciation to Professor G. W. Swift for suggesting this topic as well as his counsel, guidance, patience and encouragement during the course of this work.

The author is indebted to Mr. J. N. Roik and Manitoba Hydro for financial aid and encouragement in this work. The staff at the Dorsey station are thanked for their assistance in the installation of the saturation detector.

It is my great honour to have Professor P. Hammond, Professor R. W. Menzies, and Professor G. R. Smith as my Committee of Examiners. Thanks are due to them for their valuable time, advice and comments.

Professor A. Wexler is thanked for permitting the author to modify and extend the University of Manitoba finite-element linear field solution program MANFEP.

Support from the National Sciences and Engineering Research Council is also acknowledged.

The technicians of the Electrical Engineering department are thanked for much help, and Karen Nedohin is thanked for typing this manuscript.

Finally, I am particularly grateful to my wife Lee-Chang, daughter Wei-Wei, and son Sing-Young for their unwavering support and encouragement over the recent trying times.

TABLE OF CONTENTS

Page

LIST OF FIGURES

LIST OF TABLES

CHAPTER I

INTRODUCTION

1.1 Definition and Causes of GIC

Geomagnetically-induced-currents (GIC, sometimes called solar-induced-currents) are quasi-dc induced currents that can flow in a grounded transmission line system during an upper-atmosphere geomagnetic storm. They are typically 0.001 to 0.1 Hz (i.e. almost dc), last for say, 20 minutes, and may have peak values as high as 200 A per phase. An EPRI study[1] predicted that the Winnipeg-Duluth 500 kV ac transmission line system would be subjected to GIC, and this has proven to be true.

A geomagnetic storm is a result of solar flare activity during which a large number of charged particles are emitted from the sun and captured by the earth. These charged particles, when entering the upper atmosphere, interact with the geomagnetic field resulting in transient field fluctuations of peak values as high as a thousand gammas or more[2] (1 gamma = 1 nanotesla). Electric fields in the earth crust are induced by the variations of the geomagnetic fields. The effect of these electric fields on a transmission system such as that shown in Figure 1.1, can be modelled by a resultant earth-surface potential[3]. The induced earth-surface potential causes the GIC to flow from the earth into the power system via the grounded neutral connection of the transformer, then along the transmission line and back into the earth at the other grounded neutral point.

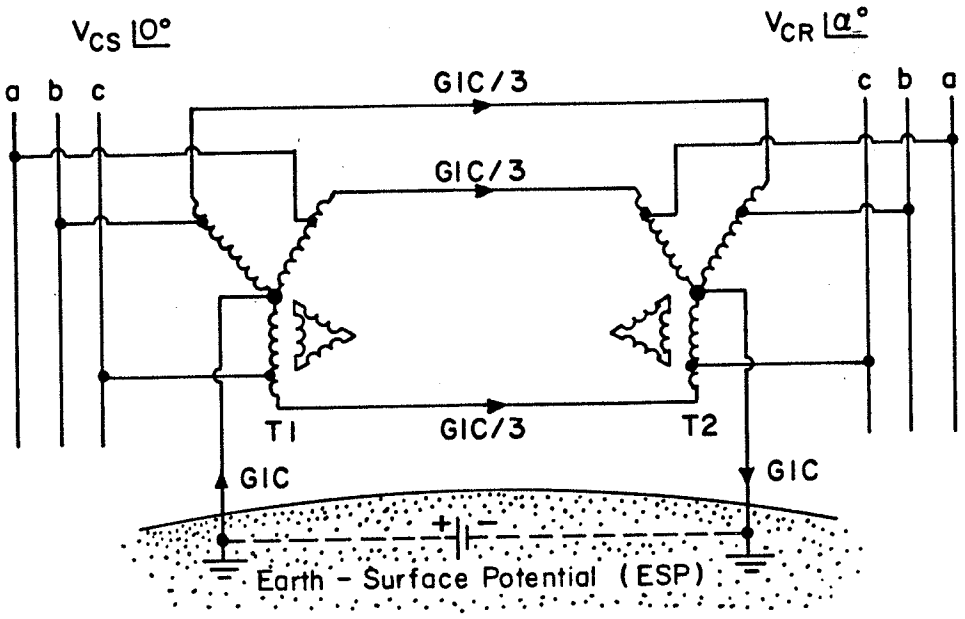

FIGURE 1.1 ESP between grounded-Y autotransformer neutrals and the resultant GIC in an EHV transmission line system.

1.2 Harmful Effects

When such currents enter a power system, they tend to saturate the power transformer core during one-half of each cycle (called asymmetrical core saturation). This condition is similar to that of simultaneous ac and dc excitation. Considerable effort has been recently directed toward the study of the effects of GIC on a power system. The emphasis has been based almost entirely on simulation and modelling of actual systems. A prominent research group in the field has been Albertson et al, and they have published a series of papers[4-9] giving a full account of the effects of GIC on electrical power systems. These harmful effects are: localized overheating in

transformers[5], shifts in real and reactive power flows[6], increased severity of switching transients[7], maloperation of relaying systems[8], and increased distortion in ac system voltage at the HVDC inverter end to prevent normal system operation[9].

From the power transformer user's view-point, the possible localized overheating damage in transformers is of prime concern because if allowed to occur, it would mean loss of system integrity. The other harmful effects mentioned above, on the other hand, can give rise to a system operating problem and are therefore considered as less harmful to the system since there is no system-component damage involved.

1.3 The Causes of Overheating in Transformers

GIC overheating in transformers can be caused by two possible sources, namely 1) excessive exciting current, and 2) excessive ac magnetic field in the oil near a saturated iron core.

Current produces I^2R loss in the windings: a main heating source in a normal fully loaded power transformer. Hence, excessive exciting current could produce overheating in the windings but it is closely monitored by the temperature relays. In general, a moderate overcurrent (say up to 2 pu of rated name-plate current) is an acceptable practice[10] because current overheating is well protected. One type of "localized" overheating in the windings can occur and is mainly due to a high current passing through a bad connection in the transformer: a manufacturing fault which is not the subject of this investigation.

The presence of an excessive ac magnetic field outside the iron core causes eddy current loss in the conductor windings. It also causes eddy current and hysteresis losses in the structural parts (such as the tank wall, tie plates, base plates and other unlaminated steel members which may be present in the transformer). Because these structural parts are not designed for intense ac magnetic fields, they may be subject to "localized" overheating which is in general less likely to be detected by the temperature relays in the transformer. Very often, localized overheating in structural parts will not be detected until it has in turn caused a serious in-zone fault, resulting in a total transformer failure.

There are many different phenomena that might cause overheating in a transformer. One such possible phenomenon is asymmetrical core saturation due to GIC. The next section will present some viewpoints in this area which have been examined by other investigators.

1.4 Prior Research

Various investigators have recently looked into the problem of overheating in transformers under GIC conditions. It would therefore be helpful to review their findings and to examine the motives as to the necessity of carrying out further research.

A paper by Albertson et al[5], in 1973, is the first paper of its kind that examines the problem of localized overheating in transformers under GIC conditions. It is interesting to note that some of the points made in that paper are derived from results which appeared in another paper regarding transformer overheating due to overexcitation (Reference 11, by Alexander et al with the General Electric

Company, U.S.A., 1966). In Albertson et al's view-point, the condition of asymmetrical core saturation is similar to that of overexcitation. Hence, they concluded that "I_{dc} = 2.0 per unit (i.e. GIC = 2.0 pu of normal exciting current) could not exist for more than one minute without excessive ILH (internal localized heating)."

J. Aubin and L. Bolduc[12], in 1978, re-examined the same problem and concluded that GIC would not cause overheating in the transformer core or primary winding (I^2R loss). However, no explanation was given as regards magnetic-field heating effects on structural parts in the transformer.

Aware of the paper of J. Aubin and L. Bolduc and having discussed the problem with them, G. Takeda of General Electric Company, U.S.A. (Manufacturer of the Manitoba 500 kV auto-transformers), in a technical report[13] submitted to Manitoba Hydro in 1979, concluded that asymmetrical core saturation due to a predicted GIC of 200 A per phase could cause magnetic flux densities as high as 0.3 T (ac, rms) in air near the saturated iron core. They then concluded that tie plates and core clamps under such intense flux densities would be subject to overheating damage within five to six seconds in the Manitoba 500 kV auto-transformers. However, there was no back-up explanation as to how the quantity 0.3 T was derived.

The different view-points on the same problem clearly suggest that sound conclusions have yet to be drawn prior to consideration of remedies.

1.5 Some Misconceptions

In examining the magnetic field of a deeply saturated closed

iron core of a power transformer (the word "closed" means "no noticeable air-gap") with concentrated windings, some authors (see discussion in Reference 11) have helped to propagate the idea that a deeply saturated closed iron core behaves like an "air core". Such a notion must be completely dispelled because the interaction between the magnetic force $\bar{H}^m$ due to the magnetized iron and the magnetic force $\bar{H}^c$ due to the magnetizing current always persist no matter how deeply saturated the iron is.

Some authors[1,7] have missed the point that the presence of an "iron" core in a transformer introduces "nonlinearity". Failure to understand this nonlinear phenomenon can lead to very misleading results.

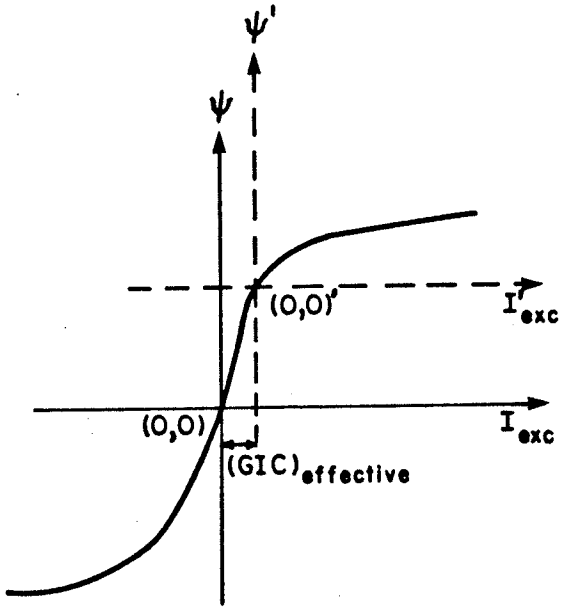

FIGURE 1.2 A magnetization curve from references 1 and 7.

Figure 1.2 is from References 1 and 7. In this figure, an obvious error made is that they have assumed that the dc biasing linkage flux ψ can be readily inferred fom the effective value of the GIC (defined in Reference 1 as (GIC)') flowing through the magnetizing winding. The value of (GIC)' is given in Reference 1, Page 81, as

$$(GIC)' = \frac{N_{ser} I_{ser} + N_{com} I_{com}}{N_{ser} + N_{com}}$$

> where the subscripts ser and com refer to the series and the common windings of an autotransformer, and N and I refer to the number of turns and the corresponding GIC, respectively . . ., all values of (GIC)' . . . are in Amp/phase for the magnetizing branch connected to the high voltage side of the transformer.

For the case of the Manitoba 500 kV autotransformer near the Dorsey inverter station, one has $I_{ser} = I_{com} = I$, and hence $(GIC)' = I$. Note that I_{exc} in Figure 1.2 is referred to the high voltage side of the transformer. Thus for a "predicted" 200 A per phase GIC flowing in the Manitoba 500 kV side of the autotransformer, the application of such a "theory" would lead to disastrous conclusions (see Chapter IV for detailed reasoning).

The rms-voltage-versus-rms-current transformer saturation curve as supplied by the transformer manufacturer consists of two sections which are in practice obtained by two different means. The lower section of the curve where the rms voltage ranges from 0 to

1.2 pu (rated name-plate voltage as base) is first obtained using magnetic circuit theory with the help of the known core configuration and the B-H characteristic of the iron material. This is then confirmed by test. The portion for rms voltages above 1.2 pu is also derived from magnetic circuit theory, but actual testing to confirm it is ignored because the risk involved in such a test is high and is also not called for in the Specifications or Standards. There is no doubt that the curve obtained in this manner can predict quite accurately the behaviours of the transformer under overexcitation conditions because the range of voltage involved is in general from 1 to about 2 pu. Under such a condition, the magnetizing ampere-turns is still small, and hence the saturation curve is still valid.

As long as the magnetizing ampere-turns is small (as it is in practice), there is no need to specify whether the iron core is magnetized by a concentrated winding or by an equal number of turns of a uniformly distributed winding. (Assume that there are no sharp corners so that the winding can be uniformly distributed around the core). The two saturation curves for the same core configurations but with different winding arrangements will be almost identical. Hence under small ampere-turn conditions, magnetic circuit theory can be fully applied to any core configuration, and the winding arrangement is of no consequence . However, the two magnetic fields outside the cores of the same configurations, but for different winding arrangements, will be completely different. These important phenomena, as described in this paragraph, have been elaborated upon by Hammond[14].

If a transformer with concentrated windings is under a

severe GIC condition, a question arises: Can the saturation curve derived from magnetic circuit theory (i.e. the curve that is supplied by the transformer manufacturer) be applied to the study of a deeply asymmetrical-core-saturation phenomenon? Some authors in fact have adopted this type of saturation curve in their investigation[1]. This could lead to a misinterpretation of a physical process.

Another obvious error made by some authors[5] is to treat the condition of asymmetrical core saturation in the same manner as that of overexcitation. Though the iron core in each case is under "saturation conditions", the behaviour of the field due to asymmetrical core saturation is quite different from that due to overexcitation. Misleading conclusions result if one applies the "overexcitation concept" to study the overheating problem due to GIC.

1.6 Research Objectives and Motives

1.6.1 Magnetic Field Investation of a Closed Iron Core

The discussion in Section 1.5 suggests that a sound understanding of the magnetic field behaviour of a deeply saturated closed iron circuit is necessary. Hence, the (partial) objective is to perform detailed magnetostatic field calculations on an iron core by taking into full consideration the nonlinearity of the iron. Numerical results will be presented but emphasis will always be placed on qualitative understanding of the field behaviour of a deeply saturated closed iron core.

1.6.2 Effect of GIC on Power Transformer Overheating

It is conceivable that a metal part excited by a uniform

ac magnetic field of 0.3 Tesla (rms) would be subject to overheating within a few seconds. However, experimental evidence obtained from a laboratory transformer under GIC conditions by this author has failed to indicate any localized overheating problem. Thermo-couples installed at various critical areas in the structural parts of the Manitoba 500 kV auto-transformers also indicate that there is no evidence of a localized overheating problem[15]. In view of this experimental evidence, a further detailed experimental work was necessary. Data obtained from various experimental measurements are analysed. The knowledge that is gained from the studies of a deeply saturated iron core is then applied to explain the experimental evidence in order to try to infer why localized overheating in structural parts of transformers due to GIC is extremely unlikely.

In summary, the (partial) objective described here is "why cannot the ac total field in air near saturated iron be high in a power transformer under a GIC condition?"

1.6.3 Detection of Asymmetrical Core Saturation

A severe asymmetrical core saturation due to GIC can cause a system operating problem. From a system operating view-point, this condition is one that the system operator must be aware of because if allowed to persist, system failure could result. The objective of this part of the author's research is to develop a device for detecting the level of asymmetrical core saturation due to GIC. The device can be used as an alarm to permit the power system operator to take action if necessary to prevent further system disturbances, or as a control signal for inserting a preventive device

designed to eliminate GIC-flow in the system.

1.7 Research Tools Available

1.7.1 Field Calculations

The "tool" that is used in this study for the nonlinear magnetic calculations is the well-known finite-element Newton-Raphson numerical technique.

For numerical analysis, a governing field formulation (derived from Maxwell's equations) must be chosen. A vector-potential field formulation is adopted here because: (1) the vector $\bar{B}$ (Magnetic flux density) derived from $\bar{A}$ (vector potential) through the "curl" operator (i.e. ∇x) is unique and is never a divergence field[16], and (2) the iron-air interface conditions are automatically satisfied when using the vector $\bar{A}$ in the context of the finite-element method, thus resulting in an algorithmic simplicity.

There is no cheaper way of obtaining a nonlinear field solution. Though the Newton-Raphson iterative scheme is adopted here for the reason of rapid convergence, much computer time is still required even for a simple study model.

The heart of success of the Newton-Raphson scheme lies in the modelling of the reluctivity curve of the iron material. This is accomplished using the cubic spline method. This method is attractive because it provides continuous derivatives of the reluctivity, and hence guarantees the convergence of the Newton-Raphson iterative process.

Considerable effort has been spent modifying and extending

the existing University of Manitoba finite-element linear field solution programs MANFEP[17] to adapt them to the nonlinear magnetic field solution. Improvements are made to the programs in order to increase computing efficiency and reduce computer time. Various special features are also included so that the field due to the iron core itself can be examined in detail.

With the numerical tool available, a study model must then be chosen. The logic dictating the choice is described below:

1) Real power transformer, in three dimensions. This model would be the most satisfying, i.e. the closest to reality. However, it is an exceedingly difficult task and would require enormous computer time. Also, the complexity of a real transformer might detract from the possiblity of general conclusions.

2) Real power transformer, in two dimensions. This model is still very difficult because of geometry singularities at the core corners and will only be used as an example in order to verify the programs and compare the results with those obtained by other researchers.

3) Classical iron ring, with uniformly distributed winding. Such a model will never have "stray" field no matter how deeply saturated it is , and is hence too trivial a model.

4) Iron Ring, with concentrated winding (2-dimensional). This is sufficiently easy to solve (although much computer time is still required) and sufficiently close to reality to illustrate the problem:

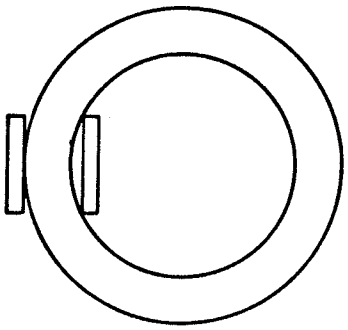

FIGURE 1.3. Two-dimensional iron ring, concentrated winding.

1.7.2 Experiments

The "tools" used in the various experimental measurements are too many to describe here. They will be fully covered in Chapters IV and V.

1.8 Outline of the Thesis

The relevant general discussions that lead to the justification of further research, the research objectives, and the tools that are available for this research have been outlined.

Chapter II briefly describes various mathematical tools for a nonlinear field numerical analysis technique, modification and extension to existing linear field program and the application of the revised program to an example problem.

Chapter III deals with a very detailed investigation on the magnetostatic field behaviour of a deeply saturated closed iron ring with a concentrated winding. Discussion of these important results is also included.

Chapter IV concerns the experimental work on the laboratory transformers with injected dc current, Hall-effect flux probe measurements, true power and true rms exciting current mearsurements, and temperature measurements. Results are analysed with the help of the knowledge gained from Chapter III.

Development of an asymmetrical saturation detector[18] (by sensing 2nd-harmonic current) for detecting a symptom of GIC, and testing of the device at Dorsey station are covered in Chapter V. Discussion of the field result is also included.

Finally, in Chapter VI, the conclusions are presented.

CHAPTER II

NONLINEAR MAGNETIC FIELD DETERMINATION

In this chapter, the finite-element Newton-Raphson numerical method will be shown to apply to the determination of the solution of a nonlinear magnetostatic field problem. The method is adopted here because it is powerful in terms of providing a satisfactory numerical solution to a real problem, and is intended to be used in the next chapter for examining the magnetic field behaviour of a deeply saturated closed iron circuit.

This chapter covers the following:

- derivation of a governing field equation based on Maxwell's equations using a vector potential;
- application of the Galerkin weighted residual process to the field equation for obtaining a set of approximating equations;
- nonlinear field solution determination through the use of the Newton-Raphson iterative process;
- cubic spline modelling of the reluctivity of the iron;
- isoparametric representation of elements;
- refinement and extension of the existing MANFEP program; and
- verification check on the revised program using an example.

2.1 The Magnetostatic Field Equation

The classical problem of magnetostatic field theory begins

with the set of Maxwell's equations[19]:

$$\nabla \times \bar{H} = \bar{J} \tag{2.1a}$$

$$\nabla \cdot \bar{B} = 0 \tag{2.1b}$$

$$\bar{B} = \mu_o \mu_r(H) \bar{H} \ , \tag{2.1c}$$

where

$\bar{H}$ magnetic force in A/m ,

$\bar{B}$ field density in tesla,

$\bar{J}$ current density in A/m^2 ,

μ_r relative permeability which is in general a function of H (capital letter denotes the magnitude of) for soft iron.

The above quantities are vectors (except μ_o and μ_r) with three space components. Hereunder, letter with a bar hat "$\bar{\ }$" denotes a vector. Equation (2.1b) implies that $\bar{B}$ is a solenoidal field. Hence, it can be represented in terms of an auxilliary variable vector potential $\bar{A}$ which defines $\bar{B}$ by its curl as

$$\bar{B} = \nabla \times \bar{A} \ . \tag{2.2}$$

Applying curl to equation (2.2), and upon substitution of (2.1a) and (2.1c), yields the final form of the vector potential equation as

$$\nabla \times (\nu \nabla \times \bar{A}) = \mu_o \bar{J} \ , \tag{2.3}$$

where $\nu = \frac{1}{\mu_r}$ is the reluctivity of the iron material. Note that since the vector $\bar{A}$ is not uniquely defined in (2.3), an additional condition is required which is

$$\nabla \cdot \bar{A} = 0 \ . \tag{2.4}$$

For three-dimensional fields, the numerical computation requires simultaneous solution of (2.3) and (2.4) which turns out to be much more complex. Since the objective of this study is to derive some general conclusions on the field behaviour of a deeply saturated closed iron core, a two-dimensional field investigation will meet the objective and is therefore a logical choice for the study.

For a two-dimensional problem as adopted here, it is assumed that

$$J_x = J_y = 0 \ , \ A_x = A_y = 0$$

and that $A_z = A_z(x,y)$ (subscripts denote components of a vector). With these assumptions, the condition (2.4) is thus automatically satisfied, and (2.3) can now be rewritten as

$$\nabla \cdot \nu \nabla A_z = -\mu_o J_z \ . \tag{2.5a}$$

To solve equation (2.5a), the iron-air interface conditions and the far field condition must be imposed. These conditions are:

$$\bar{n} \cdot (\bar{B}_{iron} - \bar{B}_{air}) = 0 \ , \tag{2.5b}$$

$$\bar{n} \times (\bar{H}_{iron} - \bar{H}_{air}) = 0 \ , \tag{2.5c}$$

$$\bar{A} \to 0 \quad \text{at sufficient far distance from the source field,} \tag{2.5d}$$

where $\bar{n}$ is a unit normal vector pointed outward from iron into air. The set of equations (2.5) gives a unique vector potential distribu-

tion throughout a system if J_z and ν are known, and thus its field $\bar{B}$ is readily obtained using equation (2.2).

An interesting case is the setting of $\nu=1$ (i.e. $\mu_r = 1$) in equation (2.5a). This leads to the solution of the field $\bar{B}^c$ due to the current in the conductor. However, such a method of direct solving (2.5a) to obtain $\bar{B}^c$ is very tedious and is seldom adopted. Should the determination of $\bar{B}^c$ be required, it is usually accomplished using the Biot-Savart law. For instance, the direct application of the Biot-Savart law to a two-dimensional rectangular conductor of uniformly distributed current density J_z (see Figure 2.1) gives the expression $\bar{B}^c$ of the form[20]

$$B_x^c = -\frac{\mu_o J_z}{2\pi}\left[(y+b)\left(\tan^{-1}\frac{x+a}{y+b} - \tan^{-1}\frac{x-a}{y+b}\right) - (y-b)\left(\tan^{-1}\frac{x+a}{y-b} - \tan^{-1}\frac{x-a}{y-b}\right) + \frac{1}{2}\left[(x+a)\ln\frac{r_2}{r_3} - (x-a)\ln\frac{r_1}{r_4}\right]\right], \qquad (2.6a)$$

$$B_y^c = \frac{\mu_o J_z}{2\pi}\left[(x+a)\left(\tan^{-1}\frac{y+b}{x+a} - \tan^{-1}\frac{y-b}{x+a}\right) - (x-a)\left(\tan^{-1}\frac{y+b}{x-a} - \tan^{-1}\frac{y-b}{x-a}\right) + \frac{1}{2}\left[(y+b)\ln\frac{r_2}{r_1} - (x-b)\ln\frac{r_2}{r_4}\right]\right], \qquad (2.6b)$$

where $\bar{B}^c = B_x^c\,\bar{i} + B_y^c\,\bar{j}$,

$r_1 = (x-a)^2 + (y+b)^2$,

$r_2 = (x+a)^2 + (y+b)^2$,

$r_3 = (x+a)^2 + (y-b)^2$,

and $r_4 = (x-a)^2 + (y-b)^2$.

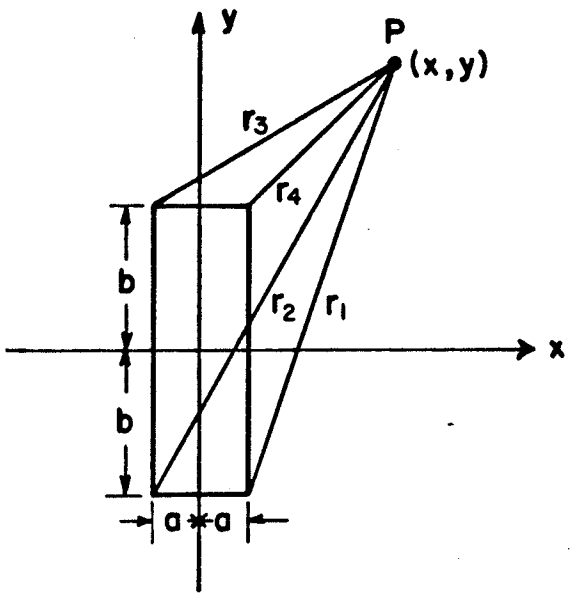

FIGURE 2.1 $\bar{B}^c$ at point (x,y) due to J_z normally out of paper.

2.2 The Finite Element Method

Obviously a closed form analytical solution of equation (2.5) is impossible to accomplish if the nonlinearity of the iron material is to be taken into consideration. The finite element method, on the other hand, provides a powerful means for obtaining the best numerical solution to the problem. The basic idea of the method is the subdivision of the field region into a finite number of subdomains and the approximation of the field in each subdomain in terms of a limited number of parameters.

In general, a finite element discretization of any problem governed by specified differential equations and boundary conditions may be achieved either by a Galerkin weighted residual process or by requiring an approximate stationarity of a suitable functional if such a functional exists. Both procedures lead to identical results[21].

For convenience, the problem discussed here will be dealt with by the Galerkin weighted residual process.

2.2.1 The Galerkin Weighted Residual Process

Consider solving numerically the equation (set $A_z = \phi$ and $-\mu_o J_z = Q$ in (2.5a))

$$\nabla \cdot \nu \nabla \phi = Q \tag{2.7}$$

in a certain region R subject to prescribed values of $\phi = \phi_b$ on the boundary (see Figure 2.2a).

The Galerkin procedure is introduced by subdividing the region R into a finite number p of smaller regions Ω_k, $k = 1, \ldots p$, called elements (see Figure 2.2b). Within each element, the unknown function ϕ in (2.7) is approximated by an appropriate trial function

$$\phi \simeq \phi_a = \sum_{i=1}^{m} \phi_i \alpha_i , \tag{2.8}$$

where ϕ_i etc. are values of ϕ_a at the m number interpolation nodes (see Figure 2.5b), and α_i are the approximating functions. These functions are called "shape functions" and are usually chosen to be polynomials.

Since ϕ_a is a function approximating ϕ, substitution of (2.8) into (2.7) will in general yield a residual error e which is

$$e = \nabla \cdot \nu \nabla \phi_a - Q \neq 0 . \tag{2.9}$$

The best solution of ϕ_a will be one which in some sense reduces the residual error e to a least value at all points in Ω_k. An obvious

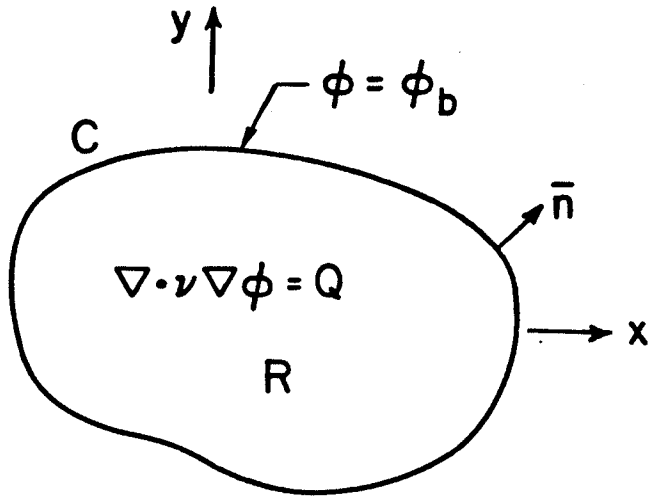

(a) The region R and its field equation.

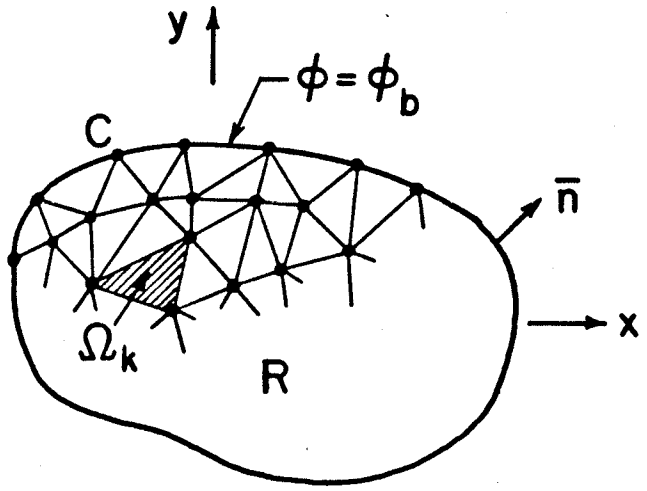

(b) Subdivision of region R into irregular triangles.

FIGURE 2.2 A two-dimensional field problem.

way to achieve this is to make use of the fact that if e is identically zero everywhere in Ω_k, then

$$\int_{\Omega_k} w_i \, e \, d\Omega_k = 0 \, , \quad \begin{matrix} i = 1, \ldots m \\ k = 1, \ldots p \, , \end{matrix} \tag{2.10}$$

where w_i are a set of linearly independent weighting functions, and the integration is to be taken over each Ω_k.

Equation (2.10) involves two sets of functions, namely the shape functions α_i and the weighting functions w_i. The particular choice of indentical sets, i.e.,

$$w_i = \alpha_i \, , \quad i = 1, \ldots m \tag{2.11}$$

leads to a scheme known as the Galerkin weighted residual process.

Substitution of (2.8), (2.9) and (2.11) into (2.10) and applying Green's theorem, yields

$$\int_{\Omega_k} \nu \nabla \alpha_i \cdot \nabla \phi_a \, d\Omega_k + \int_{\Omega_k} \alpha_i \, Q \, d\Omega_k - \int_C \alpha_i \, \frac{\partial \phi_a}{\partial n} \, dl = 0 \tag{2.12}$$

for the k^{th} element Ω_k. The line integral is applied over the far field boundary C (see Figure 2.2b) and is not required when ϕ is specified there[22]. Recognizing that $\phi_a = \sum_{i=1}^{m} \phi_i \alpha_i$ and $Q = -\mu_o J_z$ in (2.12), the set of approximating equations (2.12) for the k^{th} element can be rewritten in matrix form as

$$\begin{bmatrix} s_{11} & s_{12} & \cdot & \cdot & \cdot & s_{1m} \\ \cdot & \cdot & \cdot & \cdot & \cdot & \cdot \\ \cdot & \cdot & \cdot & s_{ij} & \cdot & \cdot \\ \cdot & \cdot & \cdot & \cdot & \cdot & \cdot \\ s_{m1} & s_{m2} & \cdot & \cdot & \cdot & s_{mm} \end{bmatrix} \begin{bmatrix} \phi_1 \\ \cdot \\ \phi_i \\ \cdot \\ \phi_m \end{bmatrix} = \begin{bmatrix} f_1 \\ \cdot \\ f_i \\ \cdot \\ f_m \end{bmatrix} \tag{2.13}$$

where

$$s_{ij} = \int_{\Omega_k} \nu \left[\frac{\partial \alpha_i}{\partial x} \frac{\partial \alpha_j}{\partial x} + \frac{\partial \alpha_i}{\partial y} \frac{\partial \alpha_j}{\partial y} \right] d\Omega_k \ , \tag{2.13a}$$

$$f_i = \int_{\Omega_k} \mu_o \alpha_i J_z d\Omega_k \ . \tag{2.13b}$$

Note that the subsystem matrix [s] is symmetric. For the entire region R containing p elements, the system matrices [S] and [F] can be easily obtained by accumulating respectively the contributions [s] and [f] from each element. The system matrix equation, that results from the accumulating process is

$$[S][\Phi] = [F] \ . \tag{2.14}$$

The orders of [S] , [Φ] and [F] are $\ell x \ell$, $\ell x 1$ and $\ell x 1$ respectively, where ℓ is the <u>total</u> number of unknown interpolation nodes in the entire region R . Once [Φ] is solved, the components B_x and B_y of the field $\overline{B}$ in any element Ω_k at any point in Ω_k can be determined using (2.2) and (2.8), i.e.,

$$B_x = \sum_{i=1}^{m} \phi_i \frac{\partial \alpha_i}{\partial y} \ , \tag{2.15}$$

and

$$B_y = - \sum_{i-1}^{m} \phi_i \frac{\partial \alpha_i}{\partial x} \ . \tag{2.16}$$

Here, ϕ_1 , ϕ_2 . . . ϕ_m are nodal values of element Ω_k . The values of $\frac{\partial \alpha_i}{\partial y}$ and $\frac{\partial \alpha_i}{\partial x}$ at a given point in Ω_k are readily evaluated (see Section 2.2.4).

It would perhaps be appropriate here to give a brief discussion on the handling of various boundary and medium interface conditions when establishing (2.14) in the context of this study.

The homogeneous Neumann boundary condition , if any (i.e. the condition where $\frac{\partial \phi}{\partial n} = 0$ is specified on the boundary of region of interest), is automatically satisfied as can be inferred from (2.12) where the line integral has been dropped.

The prescribed Dirichlet boundary condition (for example, the condition where $\phi = \phi_b$ is specified on C of R in Figure 2.2 or the condition as given by (2.5d)) can be implemented during the accumulating process when establishing (2.14). This is done during the accumulating process by ensuring that the trial function (2.8) must satisfy the Dirichlet condition on the boundary.

The medium interface conditions (2.5b) and (2.5c) are automatically satisfied if the shape functions used possess C° continuity. The proof is given in Reference 23 and will not be elaborated upon here.

2.2.2 The Newton-Raphson Iterative Procedure

In real problems of electromagnetism involving iron which is in a stage of deep saturation, variation of μ_r will need to be considered and the solution will be obtained iteratively. Previous work has indicated most rapid convergence by the Newton-Raphson iterative procedures[24,25]. Based on a similar reason the method is therefore adopted here.

The governing equations in the discretized form of (2.13) for each element are valid for the nonlinear case with [s] being

now implicit functions of $[\phi]$ as

$$[r([\phi])] \equiv [s([\phi])]\,[\phi] - [f] \tag{2.17}$$

Assume that a linear solution $[\phi^o]$ is first determined using an estimated starting value of μ_r. This linear solution $[\phi^o]$ is upgraded in stages using

$$[\phi^{n+1}] = [\Delta\phi^n] + [\phi^n] \ , \tag{2.18}$$

with $[\Delta\phi^n]$ being determined from

$$[J]\,[\Delta\phi^n] = -[r([\phi^n])] \tag{2.19}$$

until convergence is obtained. Here $[r([\phi^n])]$ represents the "residual" error in (2.17) given on the substitution of $[\phi^n]$ values and appropriate reevaluation of $[s([\phi^n])]$ using (2.13a).

The Jacobian matrix $[J]$ in (2.19) is derived by applying differentiation to $[r([\phi])]$ with respect to $[\phi]$ and then evaluating at $[\phi^n]$, i.e.,

$$[J] = \frac{d[r([\phi^n])]}{d[\phi]} \ . \tag{2.20}$$

The process of derivation of $[J]$ is straght-forward but tedious. Its final explicit form is

$$[J] = [s([\phi^n])] + [\hat{s}([\phi^n])] \ , \tag{2.21a}$$

where

$$\hat{s}_{ij} = \int_{\Omega_k} \frac{\nu'[B_x \frac{\partial \alpha_i}{\partial y} - B_y \frac{\partial \alpha_i}{\partial x}][B_x \frac{\partial \alpha_j}{\partial y} - B_y \frac{\partial \alpha_j}{\partial x}]}{B} \, d\Omega_k \tag{2.21b}$$

Again, for the whole region containing p elements, a system matrix equation can be obtained by accumulating the contributions (2.19) from each element and is

$$[J]\ [\Delta\Phi^n] = [F] - [S]\ [\Phi^n] \ . \tag{2.22}$$

The algorithm of the Newton-Raphson iterative procedure can now be briefly described. Assume that the current n^{th} solution $[\Phi^n]$ has been computed. Then the next $(n+1)^{th}$ solution $[\Phi^{n+1}]$ can be determined from the following steps:

(i) Derive the $\bar{B}$ field from the current solution $[\Phi^n]$ using (2.15) and (2.16);

(ii) upgrade the reluctivity ν and its derivative $\nu' = \frac{d\nu}{dB}$ using (2.30) and (2.31) in section 2.2.3 based on B obtained from step 1;

(iii) Establish subsystem matrics $[J]$ and $[r]$ of (2.19);

(iv) Accumulate the contributions of (2.19) to form the system matrix equation (2.22);

(v) Solve for $[\Delta\Phi^n]$ from (2.22); and

(vi) Add $[\Delta\Phi^n]$ to $[\Phi^n]$ to obtain $[\Phi^{n+1}]$.

The iterative process is repeated until a prescribed condition $|\Delta\Phi_j^n| < \varepsilon$, $j = 1, \ldots \ell$, is reached for every node point. ε is a small positive number which takes the value of 1×10^{-4} for an example in section 2.4.

Note that the linear solution $[\Phi^o]$ for the first iterative process can be determined by solving (2.14) based on an estimated starting constant μ_r value.

2.2.3 Modelling of the Reluctivity Curve

The iterative process discussed in section 2.2.2 requires continual reevaluation of the reluctivity ν and its derivative ν' in expressions (2.13a) and (2.21b) respectively. Clearly the consistency of the ν and ν' values plays a vital role in guaranteeing the convergence of the iterative process. The earlier work of Silvester et al[25] indicates that such a consistency in the ν and ν' value can only be achieved if the approximate reluctivity curve is at least continuously differentiable, which appears to be well satisfied if the well-known cubic spline interpolation method is used to model the reluctivity characteristic.

Figure 2.3 shows a typical single-valued magnetization curve which is essentially divided into two main segments: segment I with $0 \leqslant B \leqslant B_s$ and segment II with $B \geqslant B_s$. At or beyond point (H_s, B_s), segment II is a straight line with slope

$$\frac{dB}{dH} = \mu_o \ , \quad B \geqslant B_s \ . \tag{2.23}$$

Below point (H_s, B_s), segment I is a curve and its associated reluctivity curve ν is to be approximated using spline approximation as follows[26].

Assume that n data points $(H_1, B_1), \ldots (H_n, B_n)$ in region I where $0 = B_1 < B_2 < \ldots < B_{n-1} < B_n = B_s$ are given. Then the corresponding $\nu(B_2) \ldots \nu(B_n)$ can be obtained using

$$\nu = \mu_o \frac{H}{B} \ . \tag{2.24}$$

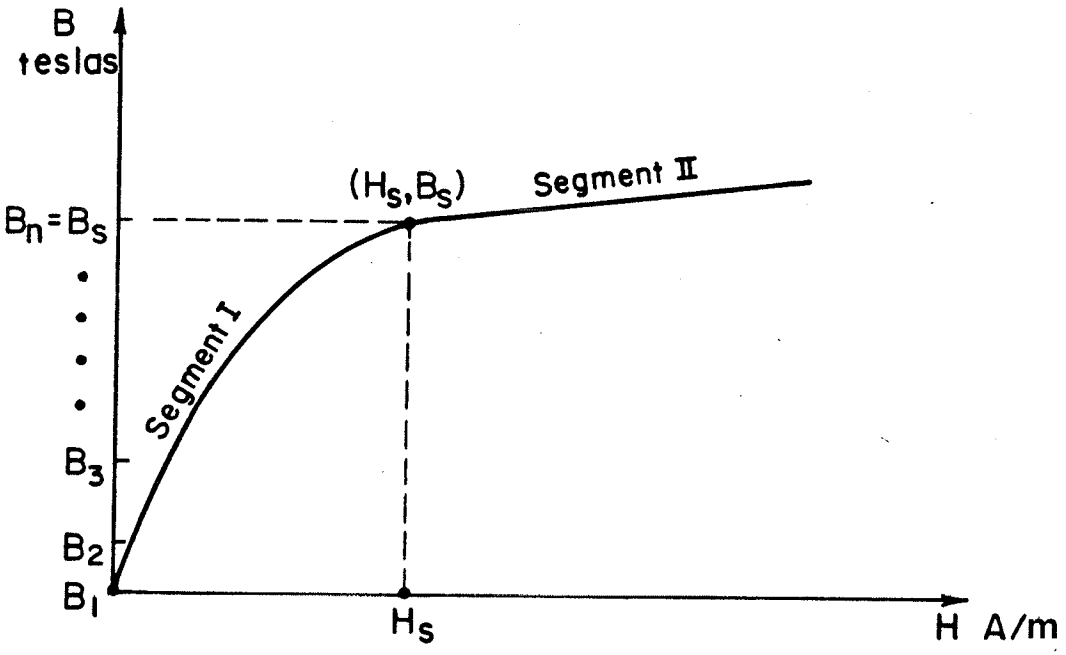

FIGURE 2.3 Typical single-valued B-H characteristic of iron.

The value of ν at $B_1 = 0$ can be determined based on an assumption that the slope (i.e. $\frac{dB}{dH}$) in the neighbourhood of B_1 is constant.

On each interval $[B_i, B_{i+1}]$, $i = 1, \ldots n-1$, $\nu(B)$ is made to agree with some polynomial P_i of the form

$$P_i(B) = a_{oi} + a_{1i}B + a_{2i}B^2 + a_{3i}B^3 ; \quad B_i \leqslant B \leqslant B_{i+1} , \tag{2.25}$$

where a_{oi}, a_{1i}, a_{2i} and a_{3i} are unknown coefficients yet to be determined. The i^{th} polynomial piece P_i is made to satisfy the conditions

$$\text{(i)} \quad P_i(B_i) = \nu(B_i) , \; P_i(B_{i+1}) = \nu(B_{i+1}) , \tag{2.26}$$

$$\text{(ii)} \quad P_i'(B_i) = S_i , \; P'(B_{i+1}) = S_{i+1} , \; i=1, \ldots n-1 , \tag{2.27}$$

Here, $S_1, \ldots S_n$ are called "free slopes". The free slopes $S_2, \ldots s_{n-1}$ are determined from the condition that the reluctivity curve $\nu(B)$ should be twice continuously differentiable meaning that $\nu(B)$ has a continuous curvature. This gives the conditions that for $i=2, \ldots n-1$,

$$P''_{i-1}(B_i) = P''_i(B_i) . \tag{2.28}$$

The remaining free slope S_1 and S_n are

$$S_1 = 0 \quad \text{and} \quad S_n = \frac{B_s - \mu_o H_s}{B_s^2} . \tag{2.29}$$

The coefficients in (2.25) can then be determined using conditions (2.26), (2.28), and (2.29). Once these coefficients have been determined, the values of $\nu(B)$ and $\nu'(B)$ are readily computed using

$$\nu(B) = a_{oi} + a_{1i}B + a_{2i}B^2 + a_{3i}B^3 \ , \ B_i \leqslant B \leqslant B_{i+1} \ , \qquad (2.30)$$

and $$\nu'(B) = a_{1i} + 2a_{2i}B + 3a_{3i}B^2 \ , \ B_i \leqslant B \leqslant B_{i+1} \ , \qquad (2.31)$$

where $i=1, \ldots n-1$.

The determination of ν and ν' in region II where $B > B_s$ is straightforward. For $B > B_s$, the line with slope μ_o has an equation given by

$$H = \frac{1}{\mu_o}(B - B_s) + H_s \ , \ B > B_s \ . \qquad (2.32)$$

Substitution of (2.32) in (2.24) yields

$$\nu(B) = \frac{B - B_s + \mu_o H_s}{B} \ , \ B > B_s \ . \qquad (2.33)$$

Differentiating (2.24) with respect to B , recognizing that $\frac{dH}{dB} = \frac{1}{\mu_o}$ for $B > B_s$, and upon substitution of (2.32), yields

$$\nu'(B) = \frac{B_s - \mu_o H_s}{B^2} \ , \ B > B_s \ . \qquad (2.34)$$

A program code is fairly easily implemented based on the reasoning given above. The program accepts 20-data points[27] (not of equal intervals) given in Table 2.1 as input data. It computes all the required coefficients which are then stored in a 2-dimensional array for interpolating the required ν and ν' values using (2.30) and (2.31). To show the powerfulness of the method, the full B-H curve using spline interpolation formulae is reproduced and is shown in Figure 2.4.

The curve in Figure 2.4 matches all the data as given in Table 2.1. It is also not as oscillatory as a single polynomial often is in the entire interval $[B_o, B_n]$.

TABLE 2.1: The H_i and B_i values for a typical soft iron.

i	H A/m	B teslas
1	0.0	0.0
2	100.00	0.70
3	200.00	1.0
4	300.00	1.125
5	400.00	1.20
6	500.00	1.25
7	600.00	1.2875
8	800.00	1.334
9	1000.00	1.3650
10	1500.00	1.430
11	2000.00	1.475
12	3000.00	1.545
13	5000.00	1.635
14	8000.00	1.715
15	10000.00	1.76
16	15000.00	1.843
17	20000.00	1.907
18	30000.00	1.98
19	40000.00	2.01
20	50000.00	2.022

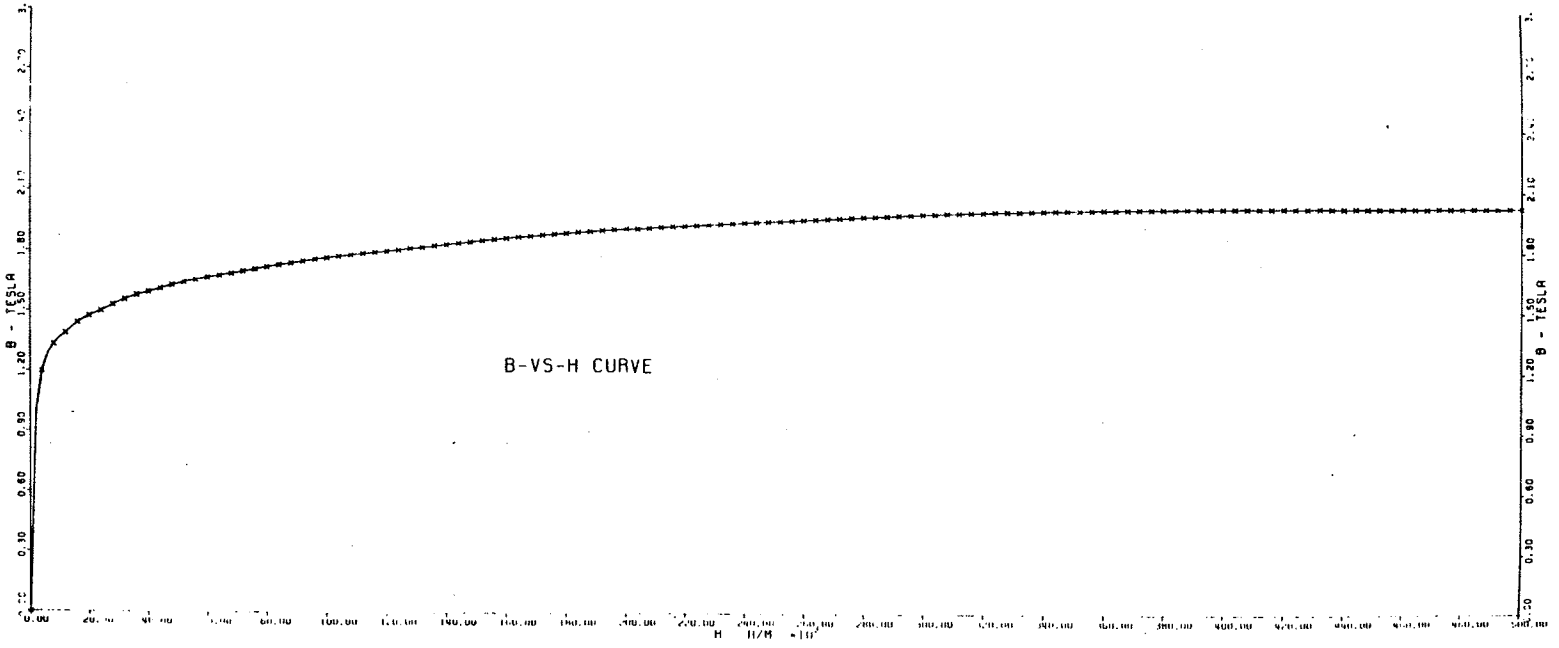

FIGURE 2.4 The B-H curve of a typical iron reproduced using spline interpolation formulae.

2.2.4 Isoparametric Representation of Elements

For a two-dimensional problem, the entries of [s] and [f] in (2.13) and that of [J] in (2.19) are all surface integrals. Undoubtedly, a meaningful solution in terms of acceptable accuracy can only be sought if those surface integrals are evaluated precisely. In general, surface integrations over elements with straight-sided boundaries are straightforward and are easily implemented in computer code. However, difficulty arises in computer code implementation if elements with curved-sided boundaries are encountered because this would mean a mathematical representation of the element is required: a very troublesome procedure. One way of overcoming this is by introducing isoparametric representation for these elements.

Figure 2.5(a) shows a local $\zeta - \eta$ coordinate system in which a simplex S with vertices (0,1), (0,0) and (0,1) is defined. The simplex S contains m node points (ζ_i, η_i), i=1, . . . m including three vertices. These node points are designated with node numbers according to a node numbering scheme shown in Figure 2.5(a). Figure 2.5(b) shows an element Ω_k of arbitrary triangular shape in R in the global x-y coordinate system. The element Ω_k also contains m specified node points of coordinates (x_i, y_i) i=1, . . . m as shown in Figure 2.5(b). A mapping of the form

$$x = \sum_{i=1}^{m} \alpha_i(\zeta,\eta)x_i$$

$$y = \sum_{i=1}^{m} \alpha_i(\zeta,\eta)y_i \qquad (2.35)$$

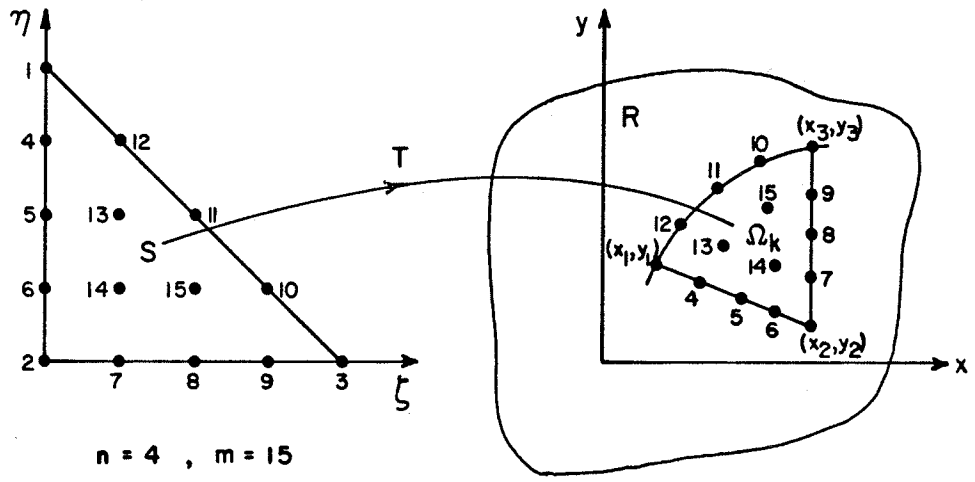

(a) A Simplex S in local $\zeta-\eta$ coordinate system.

(b) An element Ω_k of R in Global x–y coordinate system.

FIGURE 2.5 A mapping T of (2.35) from S to Ω_k.

where the shape functions $\alpha_i(\zeta,\eta)$ have the properties

$$(i)\quad \alpha_i(\zeta,\eta) = \begin{cases} 1 & \text{at } (\zeta_i,\eta_i) \\ 0 & \text{at all other nodes} \end{cases} \tag{2.36}$$

and

$$(ii)\quad \sum_{i=1}^{m} \alpha_i(\zeta,\eta) = 1 \quad \text{for all } (\zeta,\eta) \neq (\zeta_i,\eta_i)\ , \tag{2.37}$$

will map $(\zeta_i,\eta_i) \in S$ to $(x_i,y_i) \in \Omega_k$ for all $i=1, \ldots m$. It is interesting to note that for every point $(\zeta,\eta) \in S$, there exists one and only one point $(x,y) \in \Omega_k$ through the mapping (2.35).

The shape functions α_i are usually chosen to be polynomials and are determined from the Lagrange interpolation scheme[28]. Table 2.2 shows $\alpha_i(\zeta,\eta)$ for the fourth-order (i.e. n=4) polynomial approximation[29]. For two-dimensional application and n^{th} order polynomial approximation, the number of interpolation nodes, m is related to n as

$$m = \frac{1}{2}(n+1)(n+2)\ . \tag{2.38}$$

Consider now for example, that one wishes to compute numerically (2.13a), i.e.,

$$s_{ij} = \int_{\Omega_k} \nu \left(\frac{\partial \alpha_i}{\partial x}\frac{\partial \alpha_j}{\partial x} + \frac{\partial \alpha_i}{\partial y}\frac{\partial \alpha_j}{\partial y}\right) d\Omega_k\ . \tag{2.39}$$

with the mapping given by (2.35). The integration over Ω_k can be evaluated in terms of integration over simplex S thus[30]

$$s_{ij} = \int_S \nu\left(\frac{\partial \alpha_i}{\partial x}\frac{\partial \alpha_j}{\partial x} + \frac{\partial \alpha_i}{\partial y}\frac{\partial \alpha_j}{\partial y}\right)|J|\, d\zeta d\eta\ , \tag{2.40}$$

TABLE 2.2: Shape functions $\alpha_i(\zeta,\eta)$.

$L_1 = \eta$; $L_2 = 1 - \zeta - \eta$; $L_3 = \zeta$

i	n = 4
1	$\frac{1}{6} L_1 (4L_1 - 1) (4L_1 - 2) (4L_1 - 3)$
2	$\frac{1}{6} L_2 (4L_2 - 1) (4L_2 - 2) (4L_2 - 3)$
3	$\frac{1}{6} L_3 (4L_3 - 1) (4L_3 - 2) (4L_3 - 3)$
4	$\frac{8}{3} L_1L_2 (4L_1 - 1) (4L_1 - 2)$
5	$4 L_1L_2 (4L_1 - 1) (4L_2 - 1)$
6	$\frac{8}{3} L_1L_2 (4L_2 - 1) (4L_2 - 2)$
7	$\frac{8}{3} L_2L_3 (4L_2 - 1) (4L_2 - 2)$
8	$4 L_2L_3 (4L_2 - 1) (4L_3 - 1)$
9	$\frac{8}{3} L_2L_3 (4L_3 - 1) (4L_3 - 2)$
10	$\frac{8}{3} L_1L_3 (4L_3 - 1) (4L_3 - 2)$
11	$4 L_1L_3 (4L_1 - 1) (4L_3 - 1)$
12	$\frac{8}{3} L_1L_3 (4L_1 - 1) (4L_1 - 2)$
13	$32 L_1L_2L_3 (4L_2 - 1)$
14	$32 L_1L_2L_3 (4L_3 - 1)$
15	$32 L_1L_2L_3 (4L_1 - 1)$

where $|J|$ denotes determinant of the Jacobian matrix

$$J = \begin{bmatrix} \frac{\partial x}{\partial \zeta} & \frac{\partial x}{\partial \eta} \\ \frac{\partial y}{\partial \zeta} & \frac{\partial y}{\partial \eta} \end{bmatrix} . \tag{2.41}$$

The values of $\frac{\partial \alpha_i}{\partial x}$ and $\frac{\partial \alpha_i}{\partial y}$, i=1, . . . m, are easily derived from Table 2.2 by employing Chain rule. Numerical integration over simplex S for (2.40) is thus straightforward once the Gaussian sampling points on the simplex and their associated weights have been found using the product rule[31].

Clearly, the application of isoparametric representation for elements leads to algorithmic simplicity because the shape functions α_i, the Gaussian sampling points and their associated weights need to be specified only once on the simplex. This results in avoiding numerical integration performed over element Ω_k.

2.3 The Computer Program

Figure 2.6 shows the schematic structure of the program used in this study. The program is in principle derived from MANFEP but with two major changes involved, namely a modification to the MANFEP structure, and an extension of the revised MANFEP (denoted as MANFEP* in Figure 2.6).

Modification: Since MANFEP contains many subroutines and program statements that are not relevant to this study, they must be deleted for the sake of core memory saving and computing efficiency. With a very few exceptions, MANFEP also adopts call statements for almost all the data transfers between subroutines. Data transfer

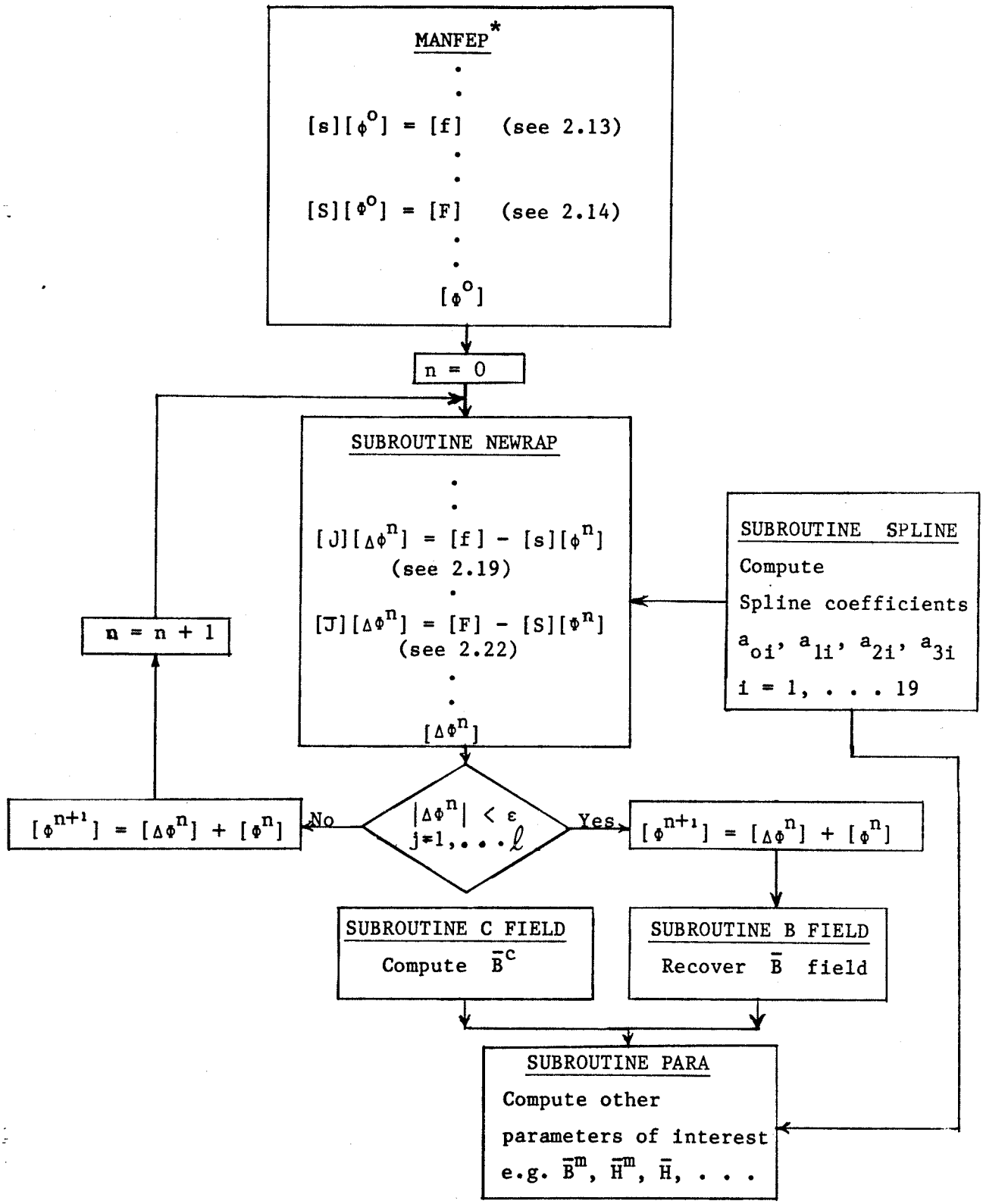

NOTE: Refer to MANFEP Programer's[17] and User's Manuals[28] for details of all subroutines in MANFEP* leading to solution $[\phi^o]$.

FIGURE 2.6: Schematic Structure of the Program

through call statements would require a huge amount of core memory allocation and therefore makes it almost impossible for the program to handle a problem of the size described in Chapter III. The revised MANFEP* uses common blocks for handling data transfer resulted in the saving of memory allocation and hence increasing the handling capability of the program. The revised MANFEP* is thus a program that does all the necessary numerical steps leading to the determination of the linear solution $[\Phi^o]$ of equation (2.14).

Extension: The linear solution $[\Phi^o]$ obtained using MANFEP* is of less interest in this study. Various subroutines have therefore been developed and incorporated into MANFEP* (see Figure 2.6) so that the resulting program can be used to study any nonlinear field problem. These subroutines were development in accordance with the mathematical reasoning given in the previous sections.

Subroutine NEWRAP in Figure 2.6 is a subprogram that actually does the Newton-Raphson iterative process. In NEWRAP, two separate orders of Gaussian quadrature schemes have been adopted for evaluating the surface integrals (2.13a) and (2.21b). A lower order of the Gaussian quadrature scheme is employed for surface integration over elements outside the iron region, and a higher order for surface integration over elements inside the iron region. This special feature offers a considerable saving in CPU time which would otherwise be very costly for the program to handle a problem of the size encountered in Chapter III.

In MANFEP*, matrix accumulation leading to (2.14) is carried out on a per element basis: the contributions (2.13) due to

an element are evaluated first, and accumulated to [S] and [F]. The accumulating process proceeds until all elements are accounted for. During the accumulating process, the trial function (2.8) of each element is checked to ensure that it satisfies the prescribed Dirichlet boundary condition (i.e. far field condition of (2.5d)). In NEWRAP, matrix accumulation leading to (2.22) is carried out in exactly the same way as in MANFEP*. Once (2.22) is created, $[\phi^n]$ is solved by the Zollenkopt bifactorization method[17] as is adopted by MANFEP*.

2.4 An Example

A two-dimensional shell-form transformer example[32] shown in Figure 2.7 has been selected for carrying out the verification check on the revised version of the modified program. The verification includes the determination of the linear as well as the nonlinear field solutions of the system.

The transformer example in Figure 2.7 consists of a pair of rectangular conductors: the conductor in the leftmost window carries a current of uniformly distributed current density J_z normally out of the paper, and the rightmost conductor, into the paper. The iron core possesses a B-H caracteristic as shown in Figure 2.4. It is desired to determine the $\bar{B}$ field of the system for a given known J_z which is 1×10^6 A/m^2 .

The governing field equation for the system is (2.5).

Since the field is quarter-plane symmetrical, the region of interest can therefore be selected in the positive quadrant and is

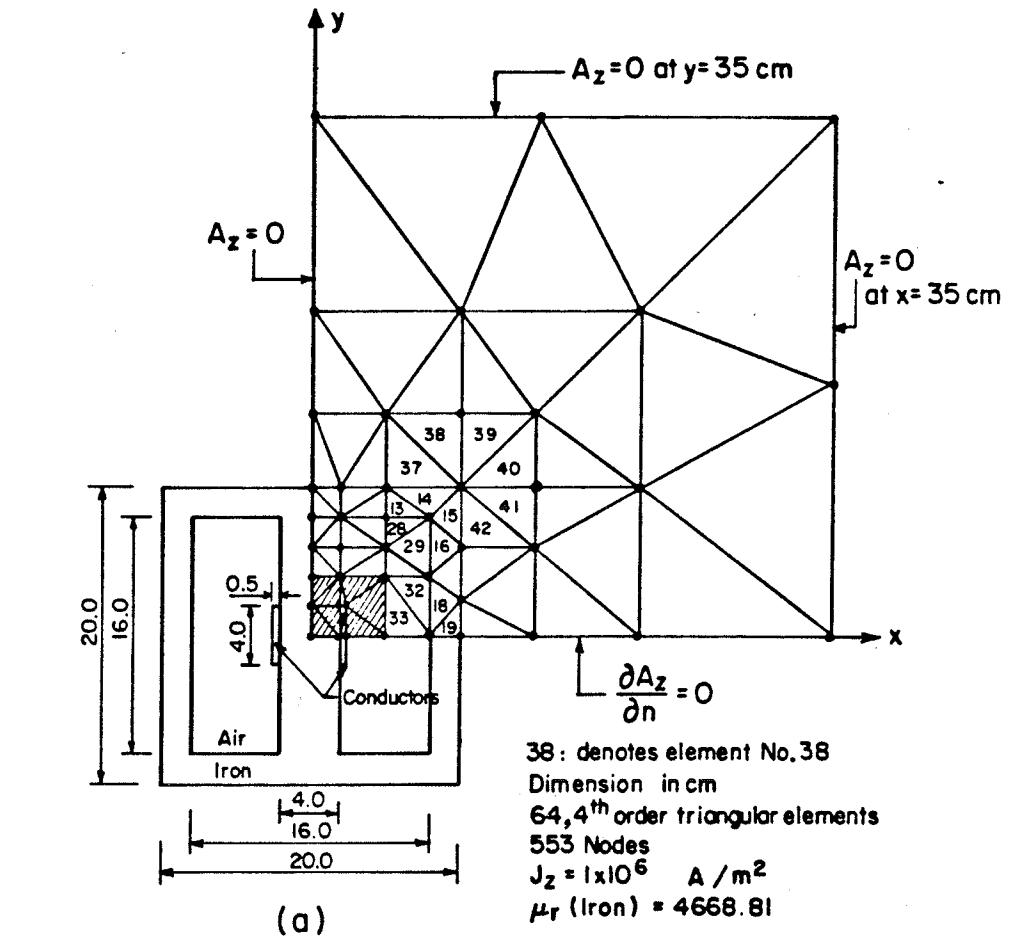

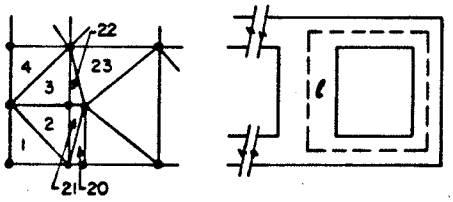

(b) Enlarged section of shaded area in (a)

(c) A closed loop ℓ for $\oint_\ell \bar{H} \cdot d\bar{\ell}$

FIGURE 2.7 A 2-dimensional transformer example.

subdivided into 64 fourth-order triangular elements with 553 nodes.

The boundary conditions applicable to this example are:

(1) at the line sections $x = 0.0$ cm , $x = 35.0$ cm and $y = 35.0$ cm , $A_z = 0$ which is a Dirichlet boundary condition; and

(2) at line section $y = 0.0$ cm , $\frac{\partial A_z}{\partial n} = 0$ which is a homogeneous Neumann boundary condition.

Of particular interest is a check in which μ_r is set to 1 in the governing field equation (2.5a). This allows checking against the results obtained using an exact equation (2.6). (Note: To obtain $\bar{B}^c$ from (2.6) for the conductor arrangement shown in Figure 2.7, a linear transformation is applied. For the rightmost conductor: $x = x' - 2.25$ and for the leftmost conductor: $x = x' + 2.25$). The results in column 2 of Table 2.3 are obtained using the modified program but with the iterative process ignored. Those in column 3 are obtained using the exact equation. It is obvious from Table 2.3 that the agreement is excellent.

Assume now that the iron has a constant relative permeability of value equal to 4668.81. This value is used in the program and the linear results obtained are shown in column 2 of Table 2.4. The results in column 3 are those computed by Zienkiewicz et al in Reference 32. Again, the agreement is excellent. The B in the core has a value 2.42 T as given in Table 2.4. This is surprisingly high and unrealistic and is no doubt due to incorrect choice of μ_r which was taken to be 4668.81.

For small magnetizing ampere-turns, an appropriate μ_r value can be derived from magnetic circuit theory using the B-H

TABLE 2.3: Comparison of $\bar{B}^c$ using equations (2.5) and (2.6).

X_{cm}	Y_{cm}	Flux density (T) (Equation 2.5 with μ_r=1)	Flux density (T) (Equation 2.6)
1.0	0.5	0.03083	0.03084
1.0	3.5	0.01174	0.01175
1.5	9.0	0.00211	0.00212
7.5	9.0	0.00131	0.00131
9.0	0.6	0.00225	0.00223
3.4	3.326	0.00849	0.00841
6.989	2.358	0.00336	0.00336
11.68	7.642	0.00093	0.00093

TABLE 2.4: Comparison of $\bar{B}$ at some typical points; μ_r = 4668.81, $J_z = 1 \times 10^6$ A/m^2.

X_{cm}	Y_{cm}	Flux density (T) (This program)	Flux density (T) (Zienkiewicz et al)
0.148	0.211	2.42	2.42
3.423	8.748	2.40	2.40
0.1479	0.2113	2.42	2.42
1.2521	0.2113	2.42	2.42
1.5268	0.2113	2.42	2.42
1.8732	0.2113	2.42	2.42

characteristic of the iron. Hence, from Figure 2.4, μ_r is found to be 2542.00. This value is fed into the program and the linear solution obtained is shown in column 3 of Table 2.5. Alternatively, μ_r value need not be predetermined; a reasonable starting μ_r value is chosen to be 3000.00. This is then fed into the program but now the iterative process is included. The set of results obtained using the iterative process is shown in column 2 of Table 2.5. The values of $\oint_{\ell} \bar{H} \cdot d\bar{\ell}$ (see Figure 2.7(c)) in each case are also determined and are included in Table 2.5.

From the viewpoint of engineering practice, the two sets of results in Table 2.5 are both acceptable to magnetic circuit designers. However, the methods of obtaining such solutions are rarely adopted by the designers since the application of simple magnetic circuit theory also predicts the same results. It would perhaps be appropriate to point out here that the use of the magnetic circuit concept is only valid for small magnetizing ampere-turns, as is encountered in practice. If the iron circuit is in a stage of deep saturation, the direct application of magnetic circuit theory would present a problem. This is the subject of further investigation in Chapter III.

Finally, iron-air interface conditions (i.e., expressions 2.5b and 2.5c) are checked. The values of B_n and H_t at various points on the iron-air interface are computed once the iterative process has been stopped. The results of B_n and H_t are shown in Table 2.6. From a closer inspection on Table 2.6, iron-air interface conditions are indeed satisfied except at points (10 cm, 10 cm) and

TABLE 2.5: Comparison of $\bar{B}$ at some typcical points.

X_{cm}	Y_{cm}	Flux density (T) (Iterative process included Starting μ_r = 3000.00)	Flux density (T) (μ_r = 2542.003 , Iterative process by-passed)
1.0	0.5	1.214	1.322
1.0	2.5	1.213	1.319
1.0	4.5	1.208	1.316
1.0	6.5	1.206	1.311
1.0	8.5	1.079	0.918
2.6	9.0	1.200	1.246
5.5	9.0	1.200	1.312
9.0	8.0	1.175	1.128
9.0	4.0	1.203	1.312
9.0	0.6	1.204	1.313
X^*_{cm}	Y^*_{cm}	$\oint_{\ell} \bar{H} \cdot d\bar{\ell}$ = 204.4 A-t	$\oint_{\ell} \bar{H} \cdot d\bar{\ell}$ = 206.3 A-t
2.059	0.5736	0.00115	0.00115
2.708	2.574	0.00339	0.00340
7.491	4.808	0.00112	0.00110
6.434	14.41	0.00031	0.00031
10.59	11.43	0.00033	0.00034
14.41	13.57	0.00021	0.00021

NOTE: Points (X_i, Y_i) are in transformer iron.

Points (X^*_i, Y^*_i) are outside the iron region.

Exact value of $\oint_{\ell} \bar{H} \cdot d\bar{\ell}$ = 200 A-t

Magnetic Circuit Theory predicts B = 1.183 T in iron.

TABLE 2.6: Normal $\overline{B}$ and Tengential $\overline{H}$ at iron-air interface

X_{cm}	Y_{cm}	Element No.	Iron B_n (T)	Air B_n (T)	Iron H_t (A/m)	Air H_t (A/m)
2.0	1.667	2	0.4338×10^{-2}		429.46	
		21		0.4338×10^{-2}		418.70
2.0	2.0	2	0.6035×10^{-2}		427.25	
		3	0.6036×10^{-2}		427.25	
		21		0.6035×10^{-2}		427.13
		22		0.6036×10^{-2}		427.13
8.0	0.0	18	-0.100×10^{-5}		-413.93	
		19	-0.156×10^{-5}		-413.93	
		32		-0.100×10^{-5}		-394.4
		33		0.172×10^{-4}		-413.3
10.0	10.0	14	0.4331×10^{-3}		0.5745×10^{-1}	
		15	0.1666		22.098	
		37		0.4331×10^{-3}		344.69
		38		0.1702×10^{-3}		135.50
		39		0.1370×10^{-3}		109.07
8.0	8.0	13	-0.2626×10^{-2}		-0.5840	
		14	-0.2046		-1775.92	
		15	-1.6218		-6338.74	
		16	-1.1881		- 380.31	
		28		-0.2625×10^{-2}		-2089.50
		29		-0.1626×10^{-2}		-1294.16

(8 cm, 8 cm) where the discontinuities of B_n and H_t occur. These points present geometry singularities. The problem can be skillfully avoided if sharp corner edges are replaced by smooth corners.

CHAPTER III

A DEEPLY SATURATED SOFT-IRON RING

This chapter examines the magnetic field behaviour of a deeply saturated soft-iron ring magnetized by a concentrated winding. The aim is to gain an understanding of how the field behaves when an iron ring is in deep saturation. Such investigation has received little attention, and the phenomenon must be fully clear prior to examining the heating problem in a transformer under GIC conditions.

3.1 Problem Geometry

Consider the two-dimensional problem of a soft-iron ring magnetized by a pair of rectangular copper bars carrying a steady-state d-c current as shown in Figure 3.1. Copper bar 1 carries a current normally into the paper, and bar 2, out of the paper. The two conductors are assumed to carry unlimited current if required and both have a relative permeability of 1. The magnetic property of the soft-iron ring is assumed to be isotropic. Furthermore, its B-H characteristic is single-valued and has the form shown in Figure 3.2. Notice in Figure 3.2 that the B-H curve in full logarithmic scale is reproduced from Figure 2.4, Section 2.2.3, Chapter II. Notice also that the saturation magnetic force H_s takes on the value of 50,000 A/m. For $H \geqslant H_s$, the slope $\frac{dB}{dH}$ is equal to μ_o. The purpose is to examine how the fields vary as a function of current density J_z which is assumed to be uniformly distributed in the conductors.

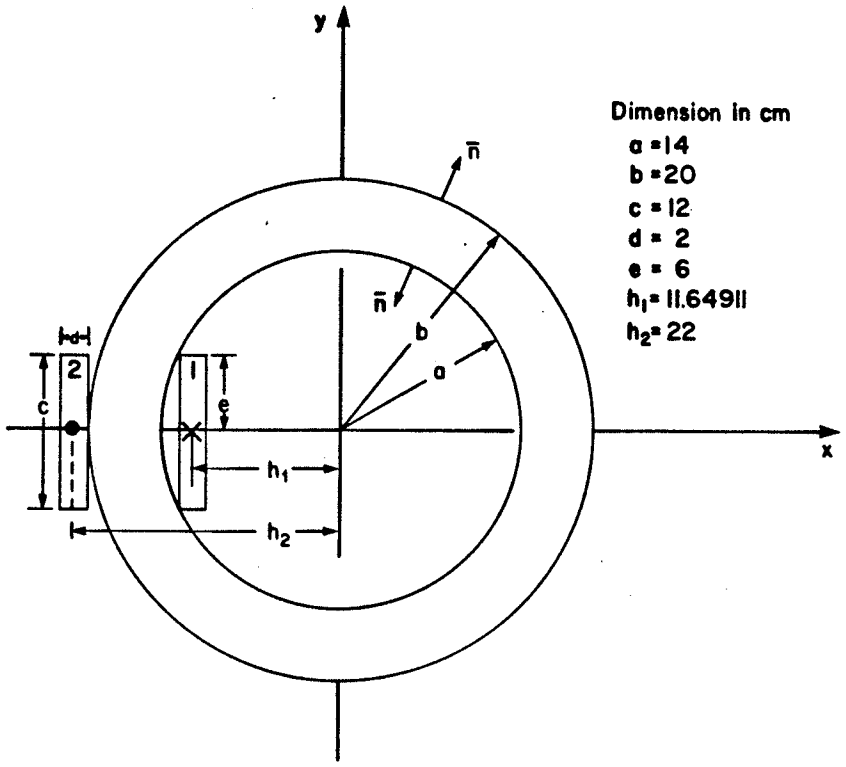

FIGURE 3.1 The two-dimensional soft-iron ring.

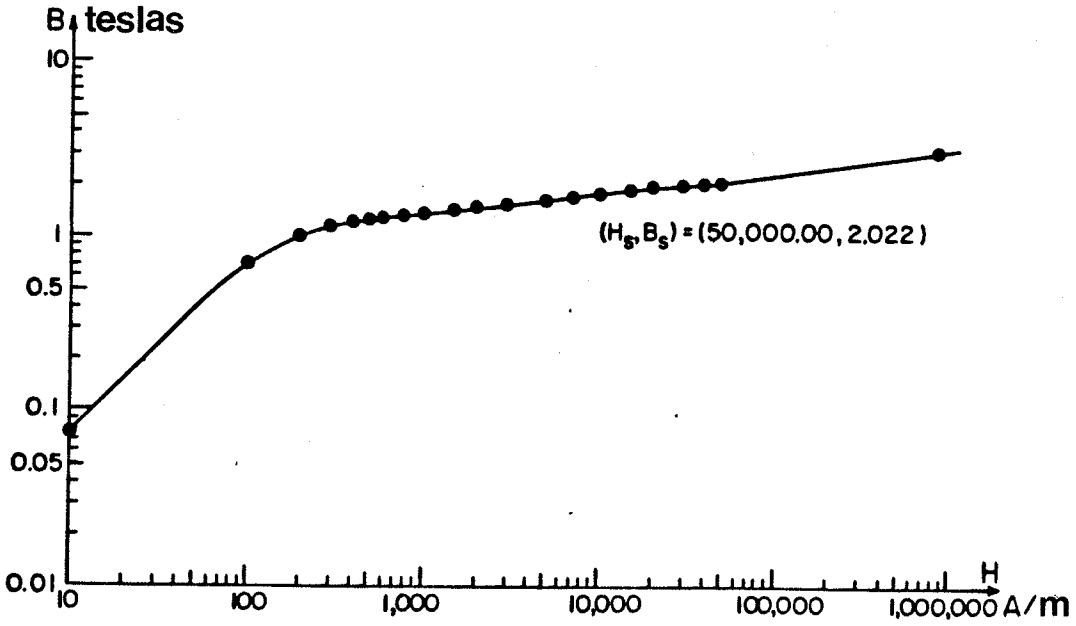

FIGURE 3.2 The B-H characteristic of a typical soft iron.

3.2 The Solution Procedure

The vector-potential field equation for the system in Figure 3.1 is

$$\nabla \cdot \nu \nabla A_z(x,y) = -\mu_o J_z(x,y) \ . \tag{3.1a}$$

The iron-air interface and the far-field conditions are

$$\bar{n} \cdot (\bar{B}_{iron} - \bar{B}_{air}) = 0 \ , \tag{3.1b}$$

$$\bar{n} \times (\bar{H}_{iron} - \bar{H}_{air}) = 0 \ , \tag{3.1c}$$

$$\bar{A} \to 0 \quad \text{at sufficient far distance from the source field.} \tag{3.1d}$$

The equations for this problem are exactly the same as those used for the transformer example described in Chapter II. Thus, no discussion of the details of the numerical procedures for this problem is required, since they are fully discussed in Chapter II. However, the following steps are taken in the process of numerical solutions for the problem.

(1) Set exit criterion ε equal to 1×10^{-6} ;

(2) Set Dirichlet boundaries (i.e. the field at infinity, essentially) at lines $x = \pm 2.4$ meters and $y = \pm 2.4$ meters (see Figure 3.3(b));

(3) Delete symmetrical line (i.e. line $y=0$ in Figure 3.3(b)) so that fields at this line are readily evaluated; and

(4) Increase the order of Gauss-point integration: this is achieved by using 6x6 Gauss points outside the iron region, and 8x8 inside the iron region.

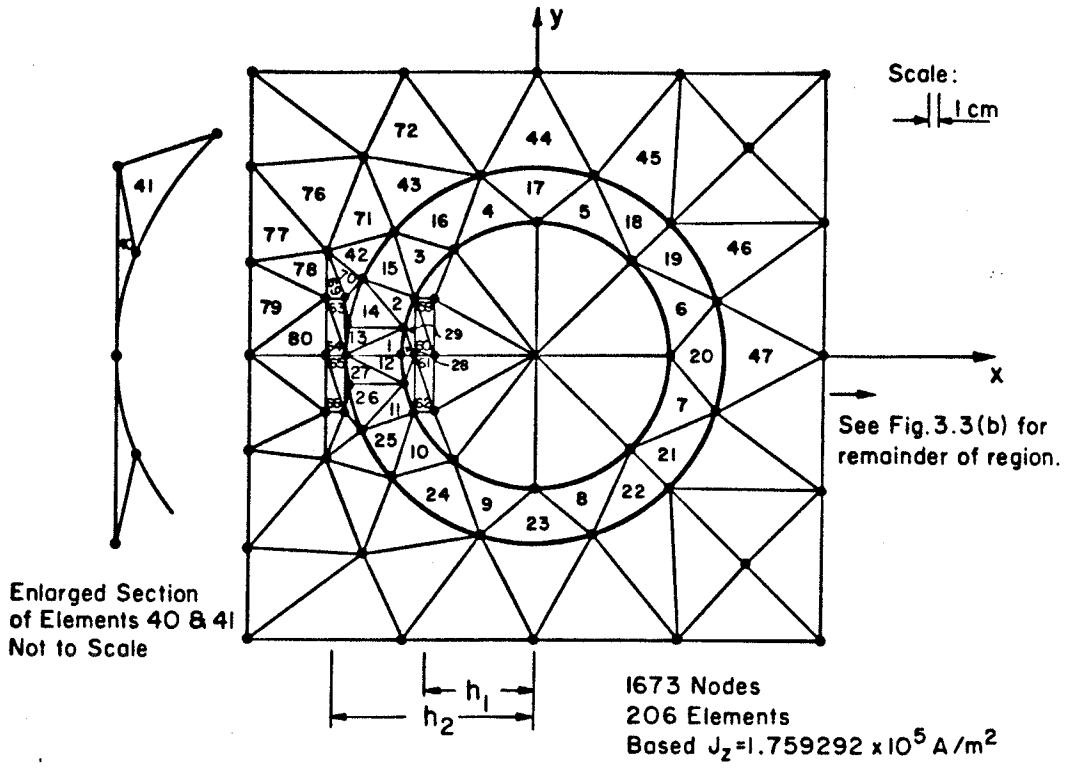

(a) The region of interest.

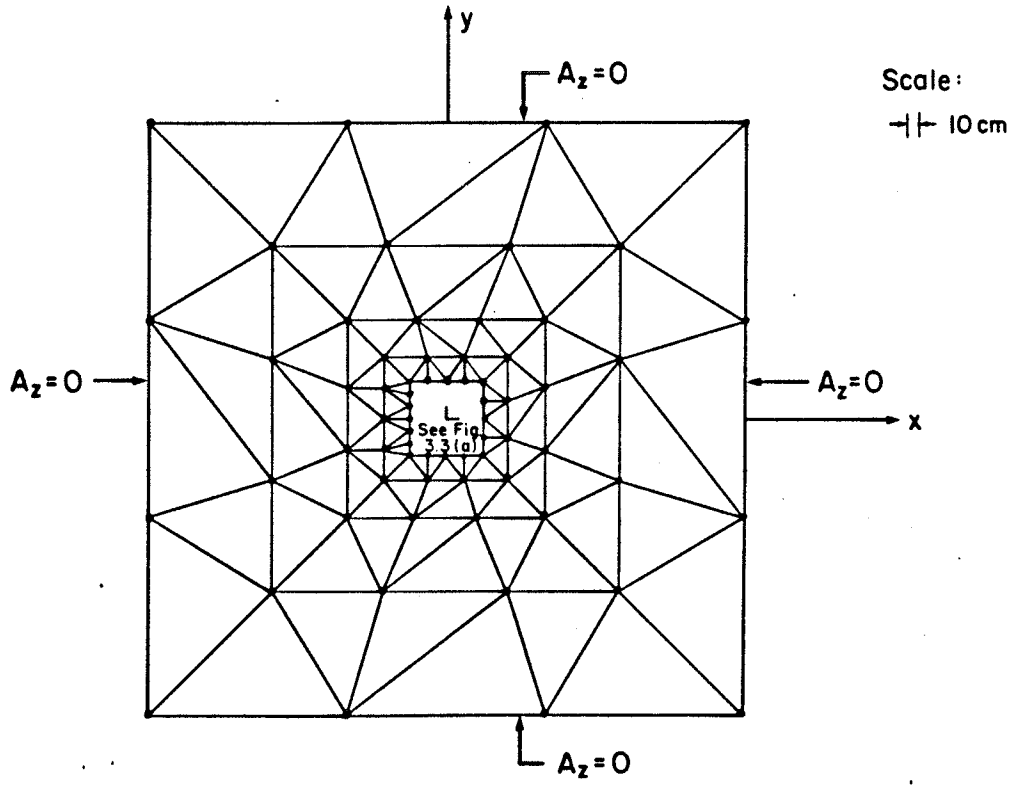

(b) Remainder of region.

FIGURE 3.3 Two-dimensional finite-element mesh.

3.3 Parameters of Interest

The field $\bar{B}^m$ due to the magnetized iron ring itself is of special interest since it is the subject of this investigation. $\bar{B}^m$ can be computed indirectly if the total field $\bar{B}$ and the field $\bar{B}^c$ (due to the current in the conductors) are known. $\bar{B}^m$ is thus given by

$$\bar{B}^m = \bar{B} - \bar{B}^c \ . \tag{3.2}$$

The field $\bar{B}$ is obtained using the nonlinear iterative process described in Chapter II, and $\bar{B}^c$ is also readily obtainable using equations (2.6a) and (2.6b) in Chpater II, with a linear transformation given by (see Figure 3.1):

$$x = x' + h_1 \tag{3.3a}$$

for conductor 1 and

$$x = x' + h_2 \tag{3.3b}$$

for conductor 2, where h_1 and h_2 are the distances for conductors 1 and 2 respectively.

The vector $\bar{H}$ can also be decomposed into two components

$$\bar{H} = \bar{H}^c + \bar{H}^m \ , \tag{3.4}$$

where $\bar{H}^c$ is the magnetic force due to the current and $\bar{H}^m$, due to the magnetized iron ring. Substitution of

$$\bar{B} = \mu_o \mu_r \bar{H} \tag{3.5}$$

into equation (3.4), yields

$$\bar{H}^m = \frac{\bar{B}}{\mu_o \mu_r} - \bar{H}^c \ . \tag{3.6}$$

Note that $\bar{B}^c$ is also defined here as

$$\bar{B}^c = \mu_o \bar{H}^c \quad . \tag{3.7}$$

Equations (3.7) is valid everywhere inside and outside the iron ring whereas the expression $\bar{B}^m = \mu_o \bar{H}^m$ is valid only outside the iron region.

3.4 Results and Discussion

The region of interest in Figure 3.1 is subdivided into fourth-order triangular elements as shown in Figure 3.3. A total of 206 elements with 1673 nodes are used in the solution process (See Figure 3.3(a) for 102 of the elements; Figure 3.3(b) for the other 104 elements). The current J_z is set at 1.7593×10^5 A/m^2. This will be called "one per-unit" current. This givesa corresponding substantially uniform flux density of value equal to 1.2 T around the inside of the ring. The computer program accepts J_z and a reasonable starting μ_r value as input data, and the solutions are obtained through a Newton-Raphson iterative process.

3.4.1 Field Inside Iron Ring

Figure 3.4 shows that the flux density B in the iron varies as a function of current density J_z. Two typical points are selected: one at point A (-16.14 cm, 0.77 cm) in element No. 1 (denoted as el) which is inside the iron surrounded by the two copper bars, the other at point B(17.15 cm, -0.69 cm) in e20 which is diametrically opposite to el . Curve A represents the flux density at point A while curve B , the flux density at point B. Note that curves A and B are obtained using a nonlinear iterative process. For

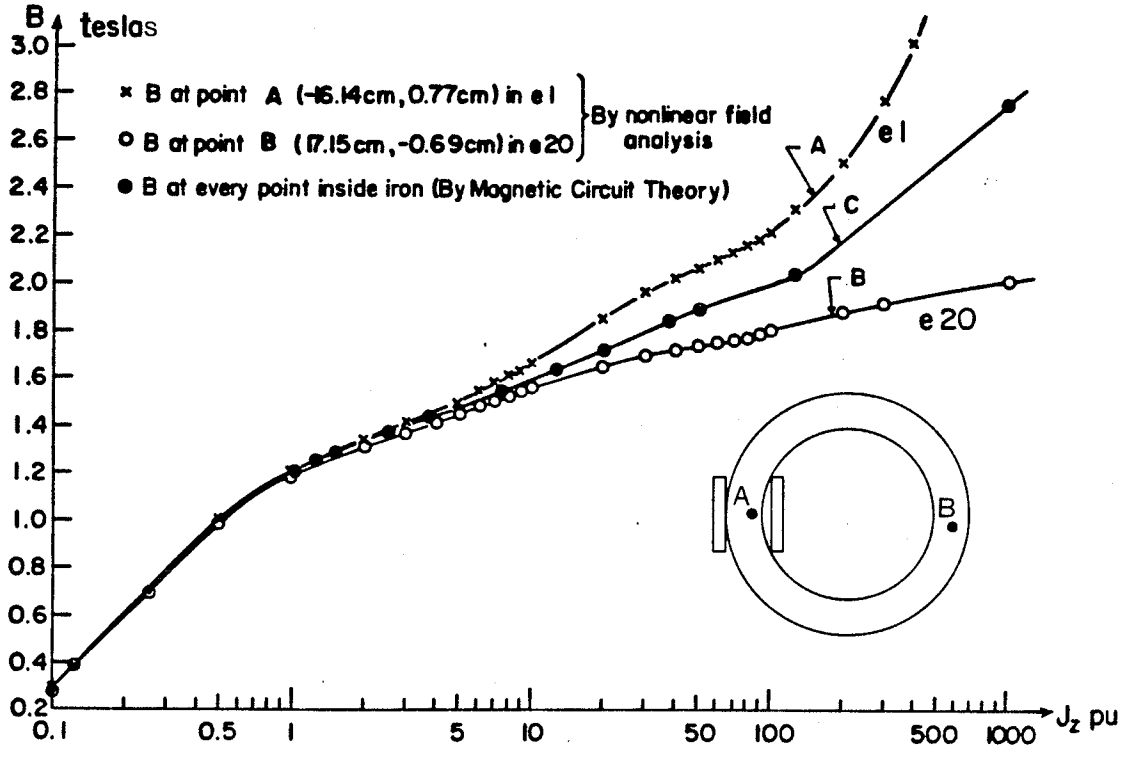

FIGURE 3.4 B versus J_z (semi logarithmic scale).

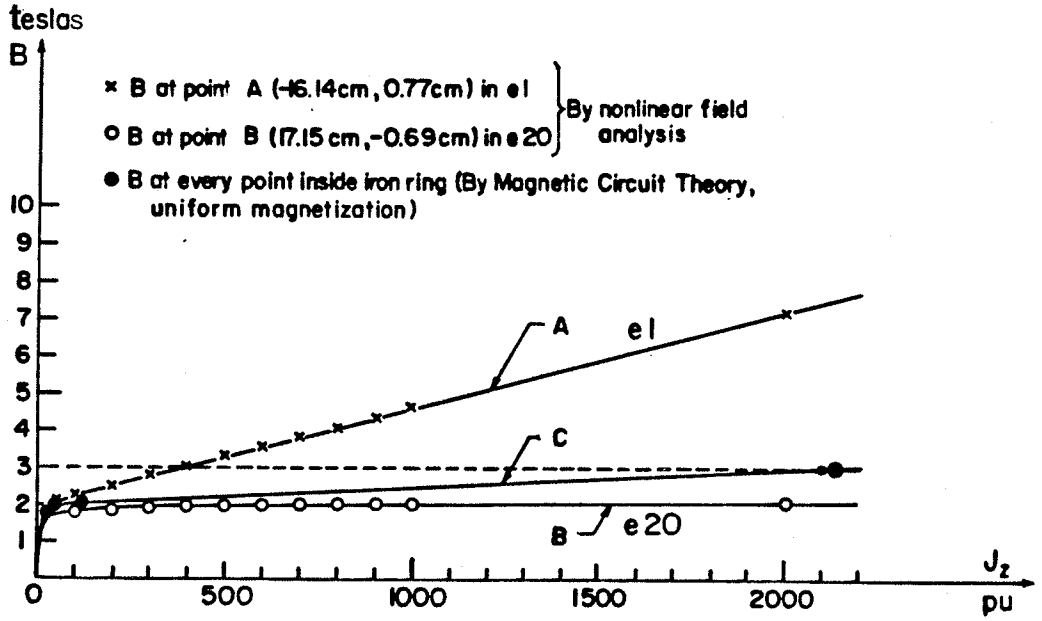

FIGURE 3.5 B versus J_z (linear scale).

comparison purposes, a curve denoted as C is derived based on magnetic circuit theory and is included in the figure. The procedures for deriving curve C are briefly described as follows:

Magnetic circuit theory is based on a conceptual assumption that the total $\bar{H}$ in the ring is uniform. Then, applying Ampere's circuital law to the ring, with dimensions as given in Figure 3.1, gives

$$H = 0.2247 \times 10^{-2} J_z \text{ A/m} . \tag{3.8}$$

For a given J_z, and from the B-H curve of Figure 3.2, the value of B in the iron ring can then be found.

It is clear from Figure 3.4 that the three curves A, B and C coincide when J_z is small, i.e., magnetizing Ampere-turns are small. However, the three curves depart from each other as J_z increases. The implication derived from curves A and B is that as the iron ring approaches deep saturation, a nonuniform saturation process appears in which the flux density B in el is no longer substantially equal to that in e20. Thus, the iron surrounded by the copper bars saturates before other parts of the iron as deep saturation approaches. To further elaborate on this important observation, two tables are prepared showing the values of H at some typical points inside the iron ring obtained through the nonlinear iterative process. Table 3.1 shows H under normal conditions where $J_z = 1$ pu, and Table 3.2, deep saturation condition where $J_z = 200$ pu.

It can be seen from Table 3.1 that the value of H remains substantially constant inside the ring for $J_z = 1$ pu. However, Table 3.2 shows that the value of H varies considerably inside the

TABLE 3.1: H at some typical points inside iron ring, J_z = 1 pu , normal condition.

Point X_{cm}	Point Y_{cm}	In Element Number	x-component H_x, A/m x 10^2	y-component H_y, A/m x 10^2	$H = \sqrt{H_x^2 + H_y^2}$ A/m x 10^2
-16.14	0.77	1	0.2046	4.2971	4.3020
-15.14	5.63	2	1.4816	3.9922	4.2583
-12.56	9.87	3	2.6265	3.3400	4.2490
- 5.53	14.71	4	4.0091	1.5068	4.2829
4.82	14.79	5	4.1196	-1.3505	4.3353
14.28	5.93	6	1.6792	-4.0176	4.3544
14.76	- 4.78	7	-1.3441	-4.1294	4.3427
5.94	-14.33	8	-4.0095	-1.6751	4.3454
- 4.53	-15.06	9	-4.0929	1.2313	4.2741
-12.10	-10.45	10	-2.7686	3.2040	4.2345
-15.02	- 5.97	11	-1.5689	3.9489	4.2492
-16.11	- 1.11	12	-0.2973	4.2960	4.3062

TABLE 3.2: H at some typical points inside iron ring, J_z = 200 pu , deep saturation condition.

Point X_{cm}	Point Y_{cm}	In Element Number	x-component H_x, A/m x 10^5	y-component H_y, A/m x 10^5	$H = \sqrt{H_x^2 + H_y^2}$ A/m x 10^5
-16.14	0.77	1	0.12778	4.33664	4.33852
-15.14	5.63	2	0.79256	2.70565	2.81934
-12.56	9.87	3	0.62365	0.76678	0.98838
- 5.53	14.71	4	0.29419	0.10726	0.31313
4.82	14.79	5	0.21747	-0.07206	0.22910
14.28	5.93	6	0.07664	-0.18349	0.19885
14.76	- 4.78	7	-0.06119	-0.18783	0.19755
5.94	-14.33	8	-0.20718	-0.08717	0.22477
- 4.53	-15.06	9	-0.29083	0.08490	0.30297
-12.10	-10.45	10	-0.57615	0.64821	0.86726
-15.02	- 5.97	11	-0.82586	2.52481	2.65645
-16.11	- 1.11	12	-0.18565	4.30751	4.31151

ring for J_z = 200 pu . Notice that the iron in the region containing elements 1, 2, 3, 10, 11 and 12 (i.e. the iron in the region surrounded by the copper bars. See Figure 3.3(a)) is in saturation conditions because the values of H in these elements are much greater than H_s (notice that H_s in Figure 3.2 takes the value of 50,000 A/m). Notice also that the iron in the region containing elements 4 to 9 is still below saturation because the values of H in these elements are less than H_s . Hence the iron surrounded by the concentrated winding always saturates before other parts of the iron as deep saturation approaches.

The term "deep saturation" is therefore adopted (and will be defined in Section 3.4.2) for the reason that it is extremely difficult to drive a closed iron circuit into <u>complete</u> saturation if it is magnetized by a concentrated winding, as is encountered in practice. Such an inference can easily be derived from Table 3.2 where the values of H in elements 6 and 7 are the lowest. Iron in this region is still well below complete saturation even for a high current density equal to 200 pu . The term "complete saturation" is defined in a conventional manner meaning that the condition $\frac{dB}{dH} = \mu_o$ is fulfilled everywhere inside the iron.

It must be pointed out here that even though the iron in the region surrounded by copper bars saturates first under the deep saturation condition, its additional increase in B must be derived from the total H <u>not</u> the additional H^c due to the additional current. When iron is magnetized by a concentrated winding, its total $\bar{H}$ must be derived from the interaction between $\bar{H}^c$ and $\bar{H}^m$.

Referring back to Figure 3.4, one clearly sees that the fields predicted by magnetic circuit theory are no longer valid because the flux density in el is not substantially equal to that in e20 . Furthermore, the flux density in el obtained by a non-linear study is higher than that obtained using magnetic circuit theory, whereas the flux density in e20 is lower than that predicted by the same theory.

The consequence of indiscriminate use of magnetic circuit theory to predict deep-saturation closed iron circuit behaviour can now be elaborated upon.

The curves in Figure 3.4 are reproduced in linear form in Figure 3.5. Now consider a case where the flux density at the point in el , for some reason, is forced to increase to 3.0 T . To establish 3.0 T at this point, curve A predicts that current density of J_z = 400 pu must flow through the copper bars. However, curve C predicts J_z = 2100 pu ! (See Figure 3.5). It is thus very obvious that an absurd value of J_z could be derived if our minds are not clear on this matter.

3.4.2 Fields Outside Iron Ring

The field outside the closed iron circuit has received little attention because it is extremely difficult to calculate. It is commonly termed as "stray field" meaning that the field wanders everywhere and is unpredictable. Since the field is highly nonuniform in nature, in what follows only one typical point at each element outside the iron ring is selected and the field is computed at those typical points only.

Figures 3.6, 3.7 and 3.8 show how flux density B at the typical points around the iron ring changes as a function of J_z. The flux density at points farther away from the ring are of no interest because their values are comparatively small and are therefore not shown here for discussion. Flux density at points inside the window of the ring is also not shown here because field in this region is of no interest in this study.

The points in Figure 3.6 are not only closer to the ring but also nearer to the copper bar, and their B values are much higher than those that are shown in Figures 3.7 and 3.8. The highest B value obtained at point E for J_z = 200 pu is 0.23 T. Such a value in practice is considered as high if it is the RMS value of an ac field, and any steel members present there would certainly no doubt be subjected to an overheating problem. However, such is not a concern because no steel members in general are allowed to be placed so close to the winding for insulation reasons.

It can be seen from Figure 3.7 and 3.8 that the values of B are small even though the points selected are near to the iron ring. Moreover, it is interesting to note that the rate-of-increase in B diminishes to a smaller near constant value as the iron ring approaches deep saturation. This contradicts a general perception that as the iron ring approaches deep saturation, more iron flux (i.e., $\bar{B}^m$) will spill out from the iron body resulting in a much higher rate-of-increase in B than the one predicted here. How has this come about?

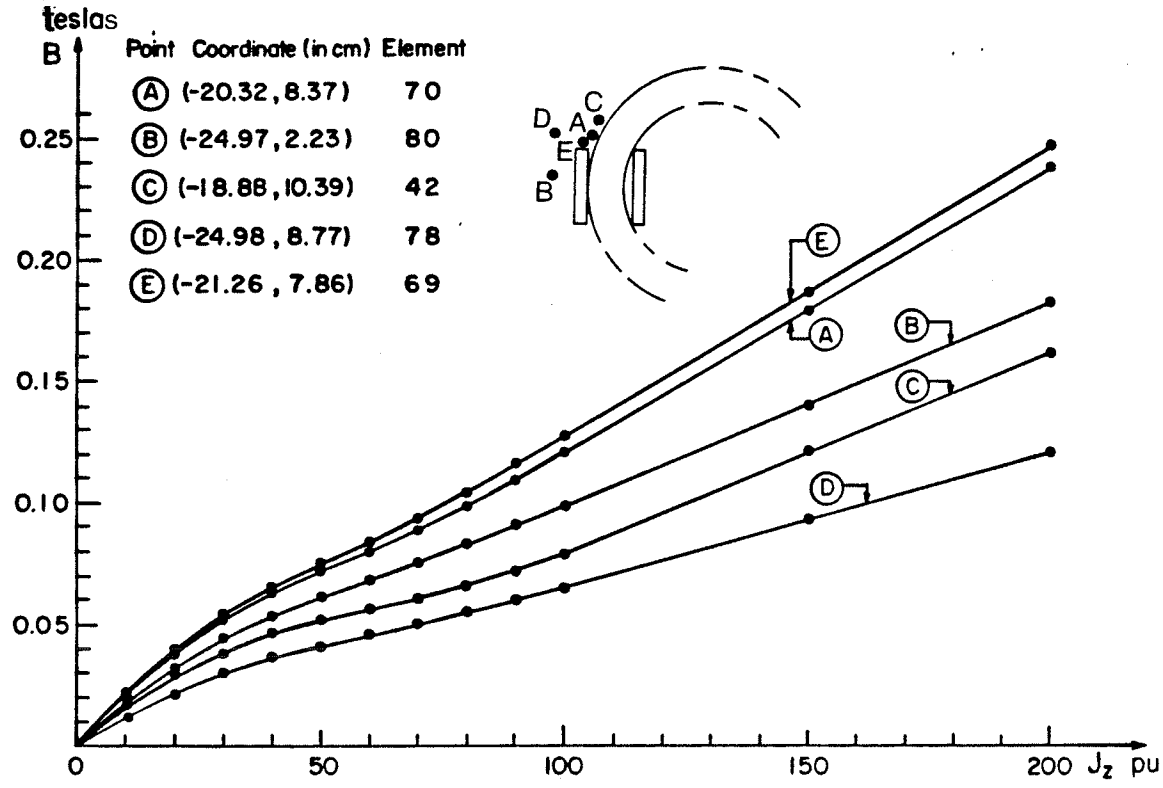

FIGURE 3.6 B versus J_z at points A, B, C, D, and E.

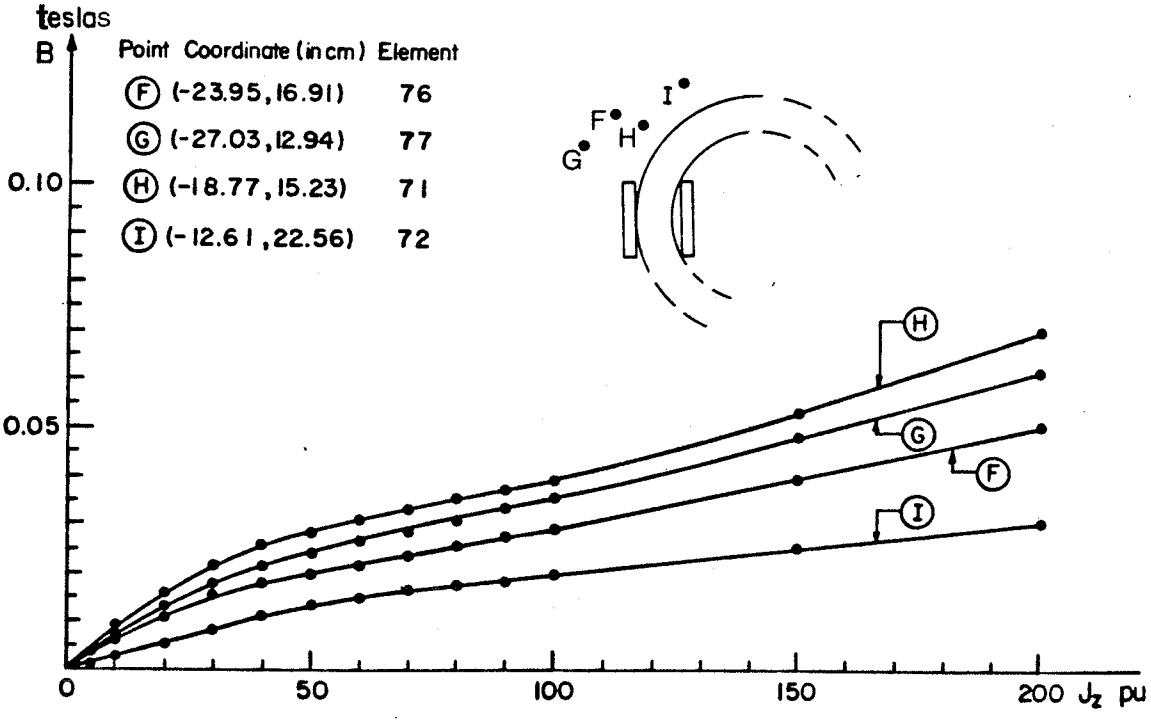

FIGURE 3.7 B versus J_z at points F, G, H, and I.

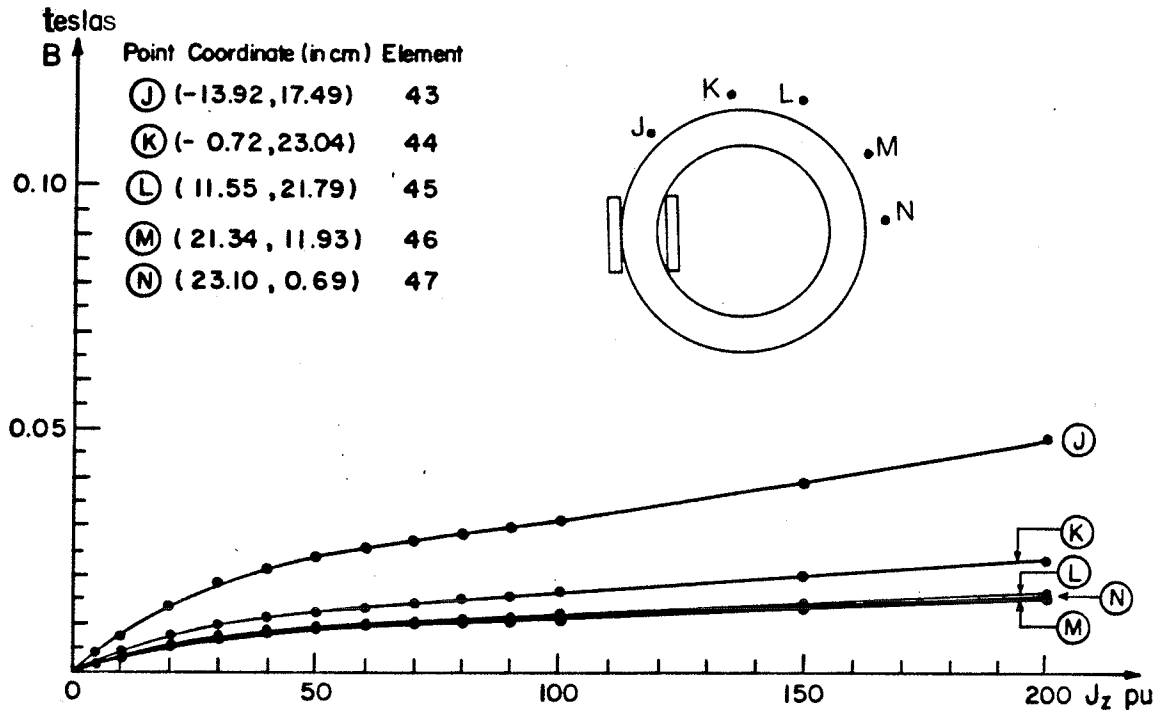

FIGURE 3.8 B versus J_z at points J, K, L, M, and N.

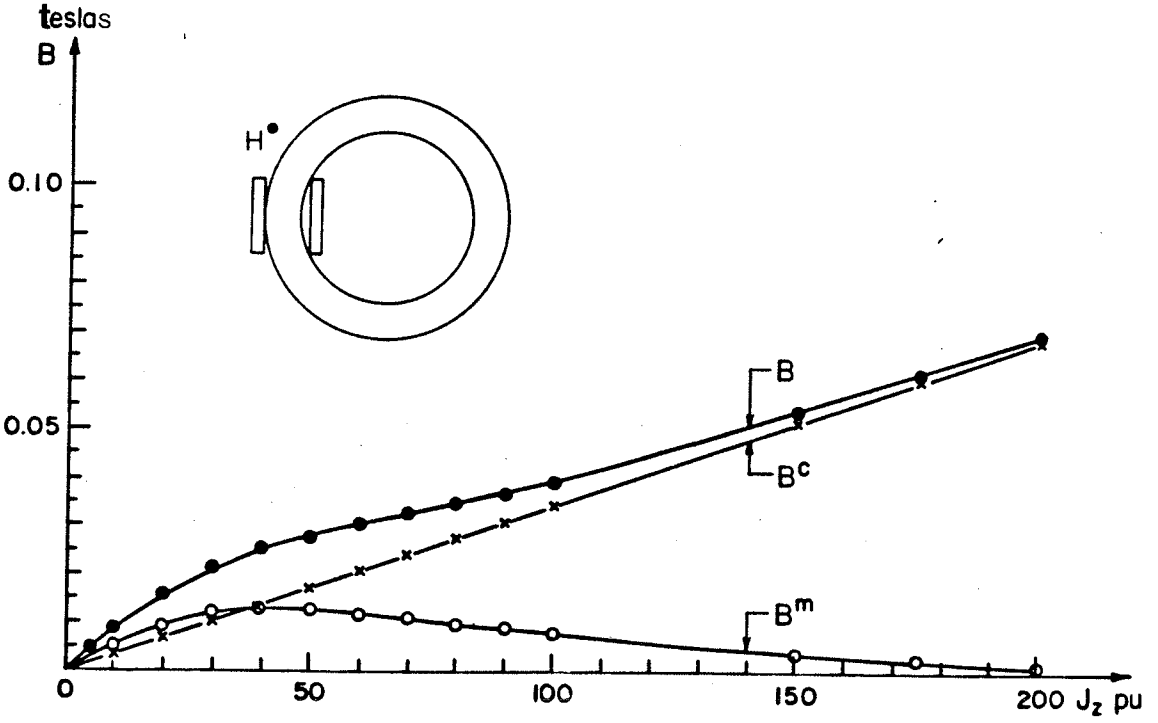

FIGURE 3.9 B , B^m , and B^c versus J_z at point H .

To explain this, let the field $\bar{B}$ at those arbitrary points either in Figure 3.7 or in Figure 3.8 be decomposed into two components $\bar{B}^c$ and $\bar{B}^m$ as given by equation 3.2. Figure 3.9 shows how the values of B, B^c and B^m vary at point H (say) as a function of J_z.

It can be seen from Figure 3.9 that B^m increases as the iron ring starts to saturate. Its value reaches a maximum of 0.013 T at J_z approximately equal to 40 pu ; then B^m <u>decreases</u> as the iron approaches deep saturation. Thus it is clear that the iron flux $\bar{B}^m$ <u>dominates</u> when iron is below deep saturation whereas current flux $\bar{B}^c$ becomes increasingly dominant when the iron is in deep saturation. Consequently, as the iron approaches deep saturation, the <u>rate-of-increase</u> in B diminishes to a smaller near constant value which is solely determined by the current in the conductors.

In view of this observation, "deep saturation" is <u>defined</u> here as follows:

> For a closed iron circuit magnetized by a concentrated winding, deep saturation refers to a magnetization stage of the iron whereby the magnitude of the iron flux B^m <u>outside</u> the iron circuit excluding the magnetizing-winding region, begins decreasing with increasing magnetizing current.

To gain a closer insight into the mechanism by which <u>any</u> deeply saturated closed iron circuit spills <u>less</u> iron flux, one recalls from fundamental electromagnetic theory that the magnetic polarization $\bar{M}$ is defined as

$$\bar{M} = \frac{\bar{B}}{\mu_o} - \bar{H} \tag{3.9}$$

At any point outside or inside the iron, the vector potential $\bar{A}$ due to the magnetized iron body is[33] (see Figure 3.1)

$$\bar{A} = \mu_o \int_V \bar{M} \times \nabla G[\bar{r}|\bar{r}] \, dv' \ , \tag{3.10}$$

where $G[\bar{r}|\bar{r}']$ is a free space Green function. The simplification of (3.10) yields

$$\bar{A} = \mu_o \int_V \nabla \times \bar{M} \, G[\bar{r}|\bar{r}'] \, dv' + \mu_o \int_S \bar{M} \times \bar{n} \, G[\bar{r}|\bar{r}'] \, da' \ , \tag{3.11}$$

and $G[\bar{r}|\bar{r}']$ has the form

$$G[\bar{r}|\bar{r}'] = \frac{1}{4\pi} \frac{1}{|\bar{r} - \bar{r}'|} \tag{3.12}$$

where $$|\bar{r} - \bar{r}'| = [(x - x')^2 + (y - y')^2 + (z - z')^2]^{\frac{1}{2}} \tag{3.13}$$

The first integration in (3.11) is to be taken over the whole volume of the iron ring whereas the second integration, the inner and outer surfaces of the ring, and $\bar{n}$ is the unit normal vector pointed outwards into the air as shown in Figure 3.1. Thus, the vector potential due to the magnetized iron ring is exactly the same as would be produced by volume and surface currents whose densities are respectively

$$\bar{J}_v = \nabla \times \bar{M} \ , \tag{3.14}$$

and $$\bar{J}_s = \bar{M} \times \bar{n} \ . \tag{3.15}$$

Substitution of $\bar{B} = \mu_o \mu_r \bar{H}$ into (3.9), yields

$$\bar{M} = (\mu_r - 1)\bar{H} = \chi \bar{H} \ , \tag{3.16}$$

by virtue of the vector indentity

$$\nabla \times \phi \bar{a} = \nabla\phi \times \bar{a} + \phi \nabla \times \bar{a} \ , \tag{3.17}$$

applying curl to equation (3.16), yields

$$\nabla \times \bar{M} = \nabla \times (\chi \bar{H}) = \nabla\chi \times \bar{H} + \chi \nabla \times \bar{H} \ . \tag{3.18}$$

Note that since $\nabla \times \bar{H} = 0$ inside the iron ring, (3.18) becomes

$$\nabla \times \bar{M} = \nabla\chi \times \bar{H} \ . \tag{3.19}$$

Now it is clear that for normal conditions, substantially constant H around the inside of the ring (see Table 3.1) implies that χ is also a constant, thus $\nabla\chi = 0$. This in turn gives $\nabla \times \bar{M} = 0$ from equation (3.19). The physical interpretation is that for the case of small magnetizing current excitation, $\nabla \times \bar{M} = 0$ and therefore $\nabla \times \bar{M}$ contributes nothing to $\bar{B}^m$. The only contribution to $\bar{B}^m$ is obviously from the term $\bar{J}_s = \bar{M} \times \bar{n}$.

Now, if iron is in deep saturation, the nonuniform H inside the iron ring (see Table 3.2) implies that χ is a function of position. It is thus clear from (3.19) that $\nabla \times \bar{M} \neq 0$. This is precisely the term $\nabla \times \bar{M} \neq 0$ that causes B^m to decrease as the iron ring approaches deep saturation.

It must be pointed out that the nonlinear iterative process as described in Chapter II takes into consideration that χ is a

function of every point in the iron ring. Though magnetic circuit theory requires that appropriate μ_r be derived from the B-H curve, it assumes the μ_r value on a one-point basis.

It would perhaps be best to examine the effect of $\nabla \times \bar{M}$ on the field $\bar{B}$ outside the iron ring. Only two extreme cases are considered; one includes $\nabla \times \bar{M}$ in the field calculations using the nonlinear iterative process, the other excludes $\nabla \times \bar{M}$, using magnetic circuit theory. Again, assume that a flux density of 2.223 tesla is, for some reason, required to be set up at point A(-16.14 cm, -0.77 cm) in el inside iron ring. Now refer to Figure 3.5, where curve A gives $J_z = 100$ pu to extablish the required flux density at this specified point, but curve C gives $J_z = 570$ pu .

Magnetic circuit theory requires that μ_r value be determined first. This is achieved by using the B-H curve of Figure 3.2. For $B = 2.223$ tesla , the corresponding μ_r is 7.9194. The two values, μ_r and J_z (i.e., $\mu_r = 7.9194$ and $J_z = 570$ pu) are used as input data in the computer program but the nonlinear iterative process is ignored. The results in column 2 of Table 3.3 are obtained from magnetic circuit theory, and the results in column 3 , from nonlinear analysis.

It can be seen from Table 3.3 that the two sets of results depart from each other considerably. The results based on magnetic circuit theory predict an extremely high field outside the iron ring, a prediction that is not confirmed by experimental evidence (Chapter IV). It must also be pointed out that the magnitude of the iron flux B^m outside the iron ring obtained using magnetic circuit theory,

TABLE 3.3: Comparison of B outside iron ring, based on B = 2.223 T at point (-16.14 cm, -0.77 cm) inside iron.

Point*	B_1 (T) (By Magnetic Circuit Theory) $\nabla \times \bar{M} = 0$	B_2 (T) (By Nonlinear Analysis) $\nabla \times \bar{M} \neq 0$	% Deviation $= 100 \times \frac{(B_1 - B_2)}{B_2}$
A	0.9713	0.1218	697.4
B	0.8216	0.0999	722.4
C	0.7323	0.0795	821.1
D	0.5600	0.0661	747.2
E	1.0027	0.1277	685.2
F	0.2762	0.0290	852.4
G	0.3218	0.0357	801.4
H	0.3941	0.0391	907.9
I	0.2092	0.0201	940.8
J	0.3306	0.0310	966.4
K	0.1678	0.0164	923.2
L	0.1148	0.0118	872.8
M	0.0993	0.0107	828.0
N	0.1032	0.0112	821.4

* Points shown are outside iron ring. For coordinates of these points, refer to Figures 3.6, 3.7 and 3.8.

increases considerably with increasing magnetizing current. Such an indication certainly violates the experimental evidence.

From the foregoing discussions, it is obvious that the use of magnetic circuit theory in studying a closed iron circuit under deep saturation conditions would result in misinterpretation of a physical process.

In general, field components are more convenient to be measured than in the field itself. Because most of the results presented in Chapter IV are in terms of field components, it would be appropriate here to examine how these field components, i.e. B_x and B_y of $\bar{B}$ outside iron ring at some typical points H and N (say), vary as a function of J_z. Figures 3.10 and 3.11 are prepared with this objective in mind.

It can be seen from Figures 3.10 and 3.11 that the direction as well as the magnitude of the field $\bar{B}$ at point H vary more drastically than that at point N. This is no doubt due to the effect of the iron flux $\bar{B}^m$ which is more significant at point H than at point N.

Figures 3.10 and 3.11 also show a common feature: the rate-of-increase of each component diminishes to a near constant which is solely dependent upon $\bar{B}^c$. This is a perfectly general conclusion which applies to any type of closed iron circuit. To prove this, a simple experiment was performed.

Figure 3.12(a) shows an experimental set-up where a d-c voltage source is used to inject current into a shell-type transformer winding. The field outside the iron core is measured using a

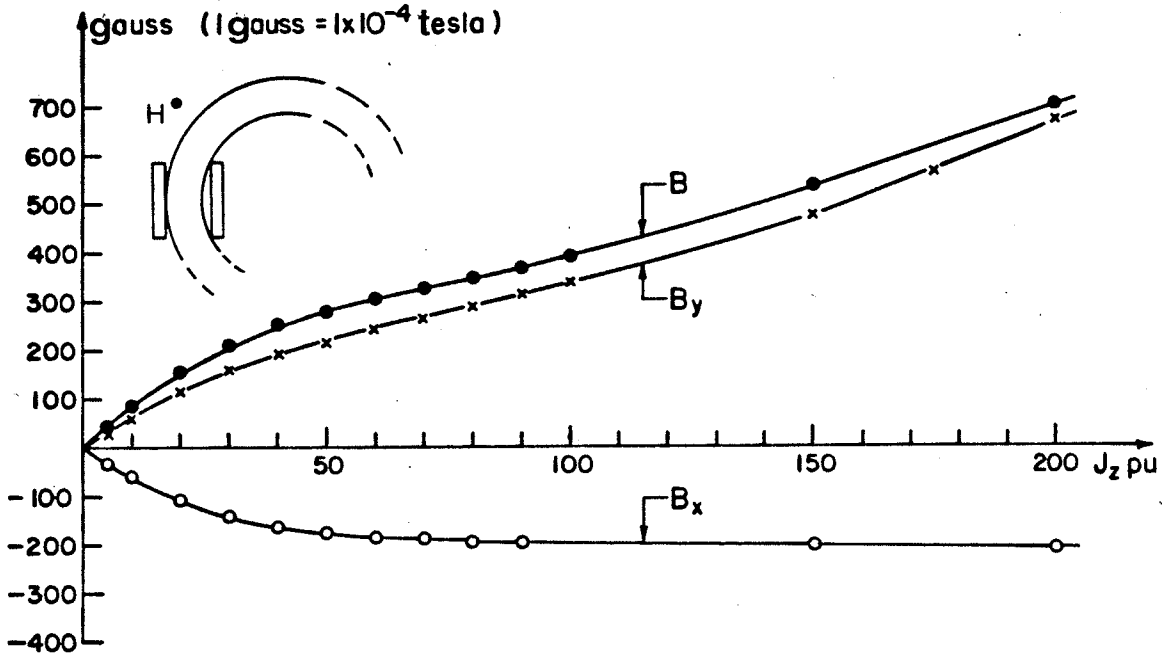

FIGURE 3.10 Components of $\bar{B}$ versus $\bar{J}_z$ at point H .

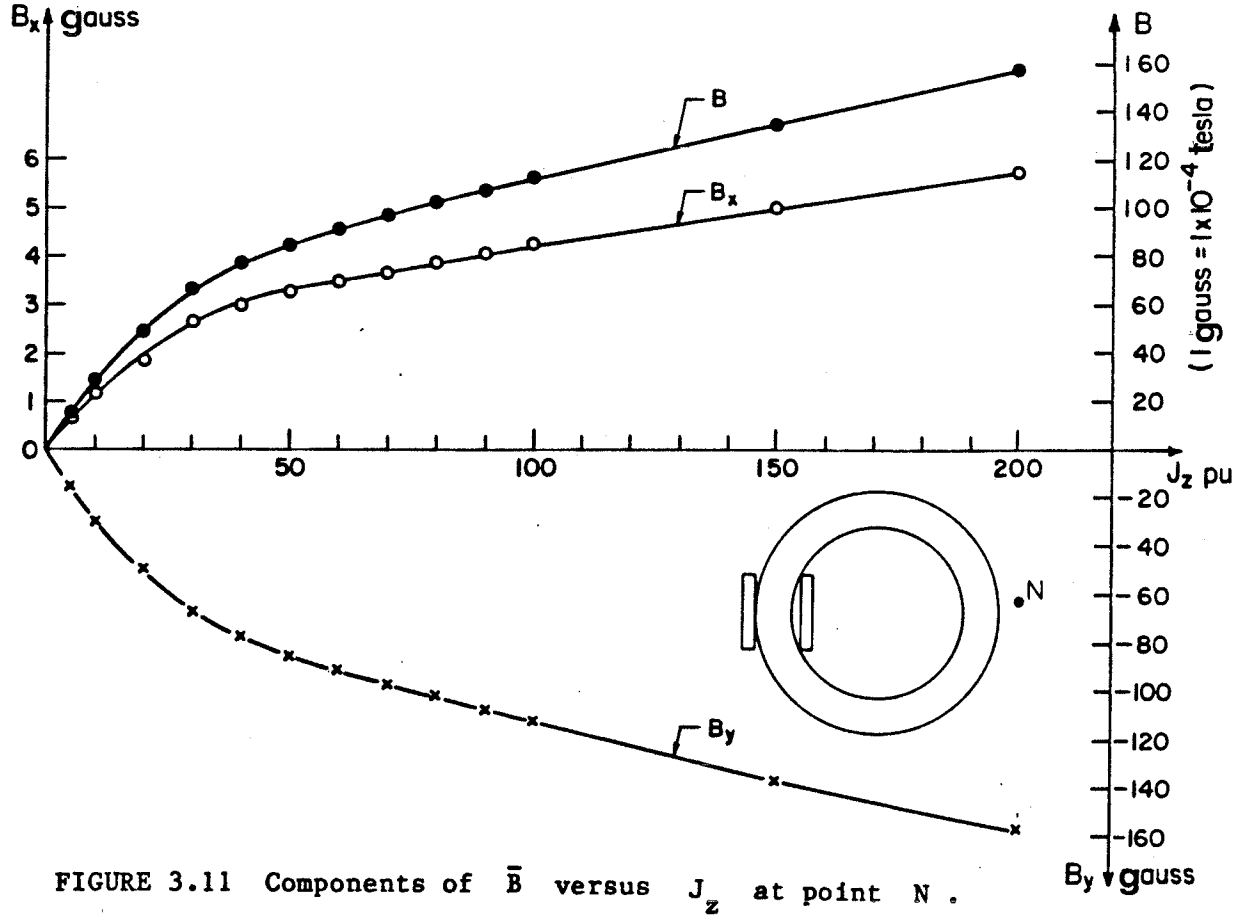

FIGURE 3.11 Components of $\bar{B}$ versus J_z at point N .

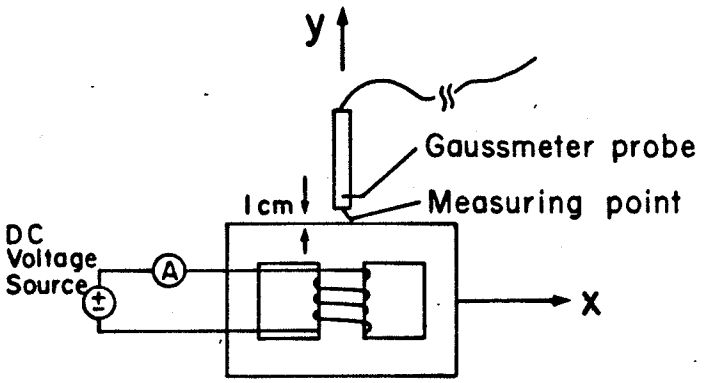

(a) Experimental set-up.

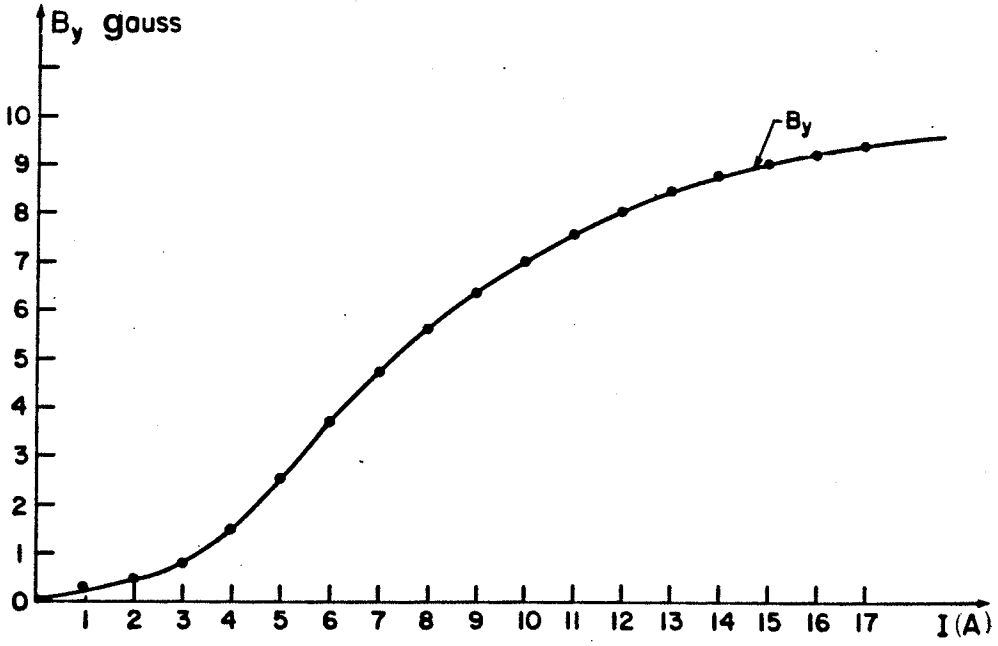

(b) Flux density B_y versus I .

FIGURE 3.12 Field behaviour outside a typical closed iron circuit.

Gaussmeter probe which is placed stationary 1 cm form the top face of the iron core. Figure 3.12(b) gives results obtained from this experiment.

Comparison of Figure 3.10, 3.11 and 3.12 indicates that curves labelled with B_y, have approximately identical behaviour except at the lower section where differences appear. This is no doubt due to slight variations in the B-H characteristic of the iron as employed in the numerical computations where the initial slope at the lower section of the B-H curve was assumed to be constant. Such an assumption however, is not true for real iron.

3.4.3 Field in Region Between Conductors and Iron

Before examining the field inside the conductors, it is necessary to investigate the field in the region between conductors and the iron body. An understanding of this will help to visualize the field in the conductors to be discussed in the next section. Two figures are prepared with this objective in mind. Figure 3.13 shows the field in the region between conductor 2 and the iron, and Figure 3.14, between conductor 1 and the iron.

It can be seen from Figure 3.13 that B^m increases with increasing J_z over the entire range of J_z. However, a cancelling effect in the vector sum $\bar{B} = \bar{B}^c + \bar{B}^m$ appears and results in $B < B^c$ over the entire range of J_z. When a conductor is placed outside and near to a closed iron circuit, this field cancelling effect will show up in the region between the conductor and the iron body, and the magnitude of the field $\bar{B}$ is always less than that of $\bar{B}^c$ produced by the current in the conductor irrespective of the magnetization state of the iron.

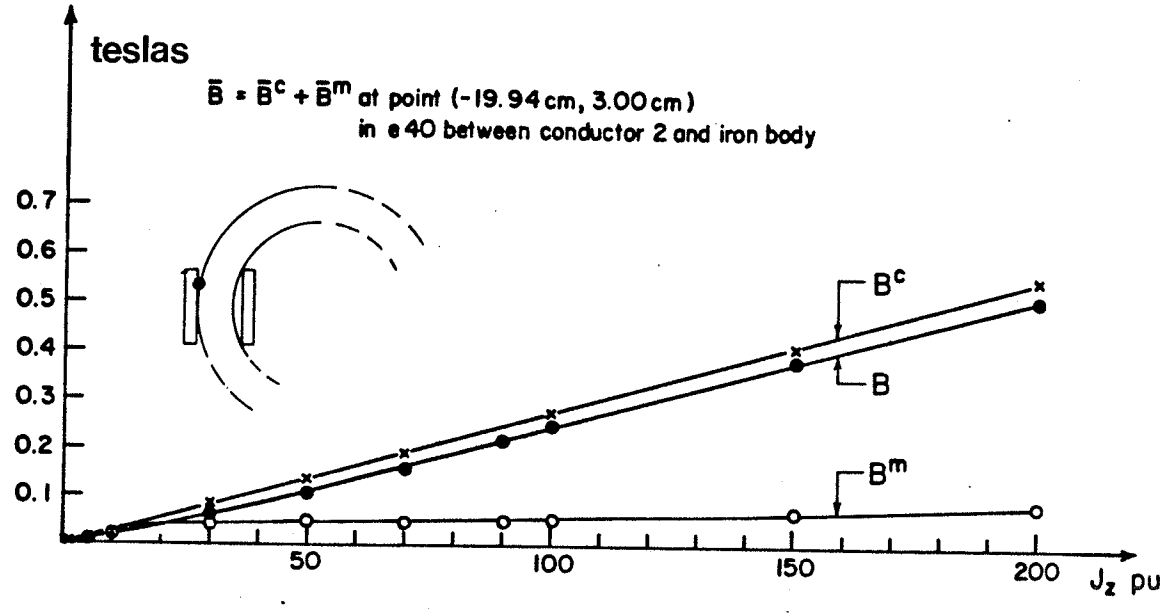

FIGURE 3.13 Field densities in region between conductor 2 and iron body.

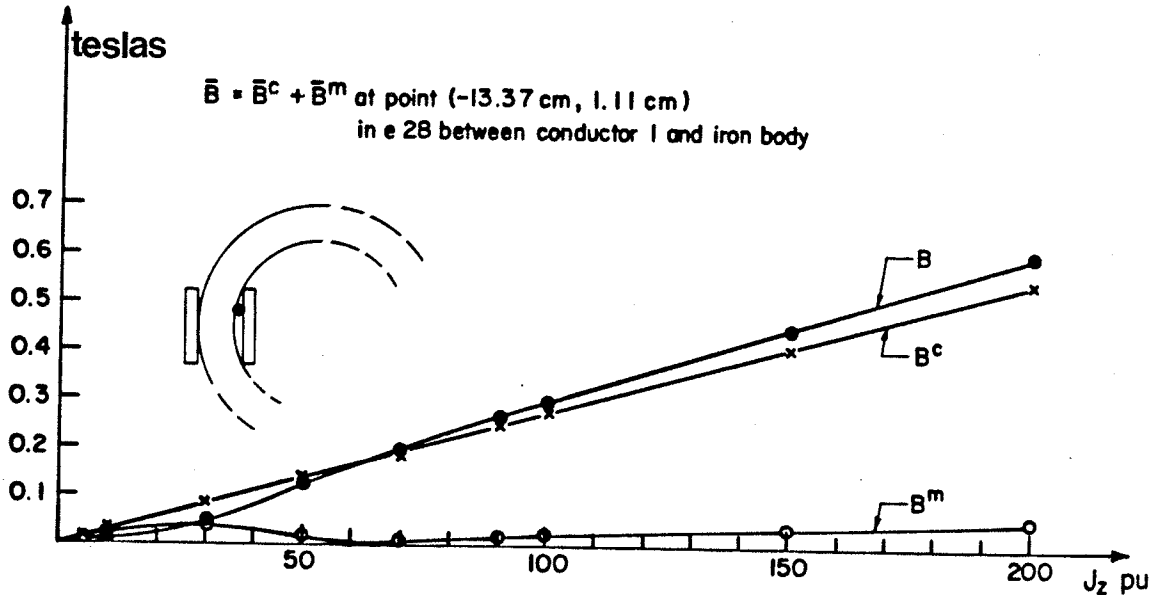

FIGURE 3.14 Field densities in region between conductor 1 and iron body.

However, Figure 3.14 shows B^m first increases with increasing J_z, and then decreases to approximately zero at J_z approximately equal to 63 pu. Within this current density range, a vector cancelling effect appears resulting in $B < B^c$. From J_z = 63 pu thereon, B^m resumes increasing with increasing J_z, but no vector cancelling effect whatever occurs. In this range, the resulting B is always greater than B^c. This again is a perfectly general statement, when the conductor is placed inside the window of and near to the closed iron circuit.

A close look at Figures 3.13 and 3.14 reveals that the field $\bar{B}$ is dominated by $\bar{B}^c$ when the iron ring is in deep saturation. To be more precise, B^m is relatively much smaller than B^c. Under deep saturation conditions one can neglect $\bar{B}^m$ without much error.

3.4.4 Field Inside Conductors

Though $\bar{B}$ is expressed as $\bar{B} = \bar{B}^c + \bar{B}^m$, it is not necessarily always true that $B > B^c$. The reason is that a vector cancellation due to $\bar{B}^c$ and $\bar{B}^m$ can occur in some region (for example, the region in between the conductors and the iron body as discussed in the previous section) resulting in $B < B^c$. One might expect a similar behaviour for the field $\bar{B}$ within the conductor regions. This will be elaborated upon hereunder.

Tables 3.4 and 3.5 show respectively the x-components and the y-components of the fields $\bar{B}^m$, $\bar{B}^c$ and $\bar{B}$ at some typical points within the conductors for the three cases where J_z = 1 pu, 30 pu and 200 pu. Table 3.6 shows the resultant fields obtained from Tables 3.4 and 3.5. A closer inspection on Tables 3.4, 3.5 and

TABLE 3.4: The x-components of the fields $\bar{B}^m$, $\bar{B}^c$ and $\bar{B}$ at some typical points within the conductors; Case (a): J_z = 1 pu , Case (b): J_z = 30 pu , and Case (c): J_z = 200 pu .

X_{cm}	Y_{cm}	In Element No.	Case	B_x^m (teslas)	B_x^c (teslas)	B_x (teslas)
			(a)	0.00025	0.00038	0.00063
-11.91	2.23	60	(b)	0.00333	0.01159	0.01492
			(c)	-0.02891	0.07727	0.04835
			(a)	-0.00025	-0.00039	-0.00065
-11.39	-2.23	61	(b)	-0.00383	-0.01193	-0.01577
			(c)	0.02396	-0.07957	-0.05561
			(a)	-0.00073	-0.00039	-0.00113
-21.26	2.23	64	(b)	-0.01706	-0.01193	-0.02899
			(c)	-0.03025	-0.07957	-0.10983
			(a)	0.00084	0.00038	0.00122
-20.74	-2.23	65	(b)	0.01965	0.01159	0.03124
			(c)	0.03554	0.07727	0.11281

TABLE 3.5: The y-components of the fields $\bar{B}^m$, $\bar{B}^c$ and $\bar{B}$ at some typical points within the conductors; Case (a): J_z = 1 pu , Case (b): J_z = 30 pu , and Case (c): J_z = 200 pu .

X_{cm}	Y_{cm}	In Element No.	Case	B_y^m (teslas)	B_y^c (teslas)	B_y (teslas)
			(a)	-0.00183	0.00129	-0.00054
-11.91	2.23	60	(b)	-0.03502	0.03880	0.00378
			(c)	0.02331	0.25871	0.28203
			(a)	-0.00178	0.00026	-0.00152
-11.39	-2.23	61	(b)	-0.03449	0.00795	-0.02653
			(c)	0.01532	0.05306	0.06838
			(a)	-0.00169	0.00026	-0.00142
-21.26	2.23	64	(b)	-0.03690	0.00795	-0.02894
			(c)	-0.048051	0.05306	0.00501
			(a)	-0.00183	0.00129	-0.00054
-20.74	-2.23	65	(b)	-0.04018	0.03880	-0.00137
			(c)	-0.05289	0.25871	0.20582

TABLE 3.6: The magnitude of the fields $\bar{B}^m$, $\bar{B}^c$ and $\bar{B}$ at some typical points within the conductors; Case (a): J_z = 1 pu , Case (b): J_z = 30 pu , and Case (c): J_z = 200 pu .

X_{cm}	Y_{cm}	In Element Number	Case	B^m (teslas)	B^c (teslas)	B (teslas)	Remark
			(a)	0.0019	0.0014	0.0002	$B < B^c$
-11.91	2.23	60	(b)	0.0352	0.0405	0.0154	$B < B^c$
			(c)	0.0371	0.2700	0.2861	$B > B^c$
			(a)	0.0018	0.0005	0.0017	$B > B^c$
-11.39	-2.23	61	(b)	0.0347	0.0143	0.0309	$B > B^c$
			(c)	0.0284	0.0956	0.0881	$B < B^c$
			(a)	0.0018	0.0005	0.0018	$B > B^c$
-21.26	2.23	64	(b)	0.0407	0.0143	0.0410	$B > B^c$
			(c)	0.0567	0.0956	0.1099	$B > B^c$
			(a)	0.0020	0.001349	0.001343	$B < B^c$
-20.74	-2.23	65	(b)	0.0447	0.0405	0.0313	$B < B^c$
			(c)	0.0637	0.2700	0.2347	$B < B^c$

3.6 reveals that a vector-cancellation effect due to $\bar{B}^c$ and $\bar{B}^m$ does occur within certain conductor regions resulting in $B < B^c$.

Figure 3.15 gives a pictorial representation of the y-components of the fields $\bar{B}^c$ and $\bar{B}^m$ derived from Table 3.5. A similar pictorial representation can also be derived from Table 3.4 for the x-components of the fields $\bar{B}^c$ and $\bar{B}^m$. However, this will not be included here for discussion.

Figure 3.15(a) shows that under the normal conditions, B_y^m opposes B_y^c in the inner as well as outer sections of the conductors resulting in $B_y < B_y^c$.

A similar observation applies to Figure 3.15(b) but now B_y^m and B_y^c increase accordingly with increasing J_z.

Figure 3.15(c) indicates that B_y^m in conductor 1 behaves in quite a different way when the iron ring is in deep saturation. Notice that B_y^m in conductor 1 reverses its <u>direction</u> resulting in $B_y > B_y^c$.

Thus, the presence of the field $\bar{B}^m$ in the conductor region causes either (i) an increase in B resulting in $B > B^c$ or (ii) a decrease in B resulting in $B < B^c$. The second phenomenon has been missed by some authors[11] when studying the eddy-current loss in conductor windings of a closed iron circuit under deep saturation conditions. Because of the phenomena (i) and (ii), the <u>net</u> increase in conductor-eddy loss due to total field $\bar{B}$ will be small under deep saturation conditions. This fact will be further borne out by experimental evidence in section 4.4.2.1, Chapter IV.

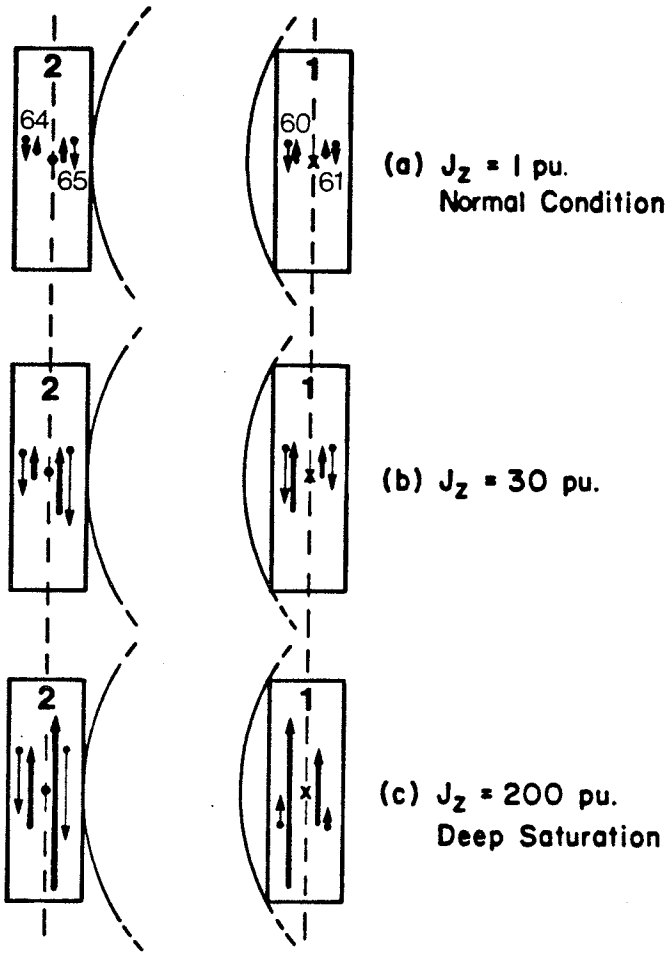

NOTES:

(1) All lengths of vectors are indicative, not to scale.

(2) For the coordinates of the points and the values of the y-components of the fields, refer to Table 3.5.

(3) Dot '•' and cross 'x' are conventional current directions.

(4) Heavy arrow " ↑ " denotes B_y^c , light arrow " ↑ " denotes B_y^m .

(5) $B_y = B_y^c + B_y^m$ within conductors .

FIGURE 3.15 Pictorial representation of B_y^c and B_y^m within conductors 1 and 2.

CHAPTER IV

EXPERIMENTAL INVESTIGATIONS

It has been shown in Chapter III that the field of a deeply saturated closed iron circuit behaves in a more peculiar way than expected. For example, iron spills less flux rather than more flux when the iron is in a deep saturation condition. Before applying the results of Chapter III, which are basically derived from dc excitation, to explain the heating problem in a transformer under a GIC condition, it is necessary that some further experimental evidence be obtained from an ac plus dc excited transformer.

This chapter therefore covers extensively the laboratory work that has been carried out on an actual 3 kVA shell-form power transformer. Experiments performed include qualitative investigation on the transformer under a GIC condition, magnetic field measurements, true power and true exciting current measurements, and temperature measurements.

4.1 Qualitative Investigation

Though special interest is directed to the transformer overheating problem, it would perhaps be best to have an overall general understanding on how a power transformer behaves under GIC conditions. In view of this, a laboratory test was performed.

Figure 4.1(a) shows the general set-up for the experiment. Transformers T1 and T2 are two identical transformers and are connected in a back-to-back arrangement. Such an arrangement facilitates a

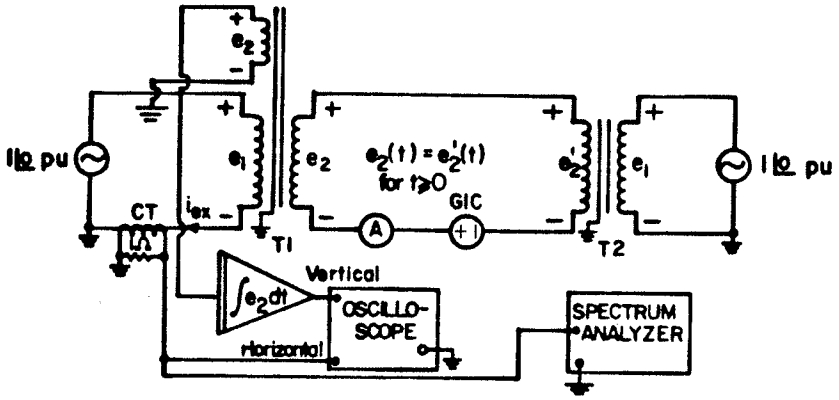

T1, T2 : Shell-Type Transformer, 3 kVA, 120/120 volts, 60 Hz.
CT : Fluke-mode CT, Frequency Response up to 1000 Hz.
(A) : DC Ammeter. Base Current = 25 A fundamental.

(a) General Set-Up

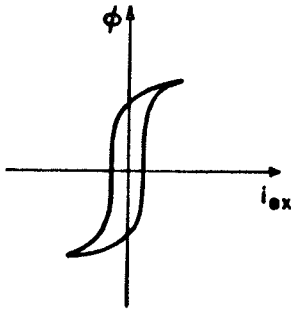

(b) Dynamic Hysteresis Loop
GIC = 0 pu

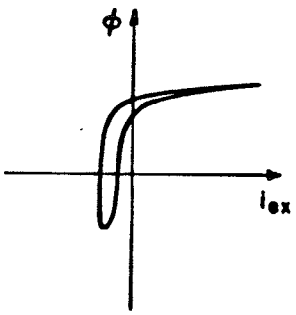

(c) Offset Dynamic Hysteresis Loop
GIC = 0.22 pu

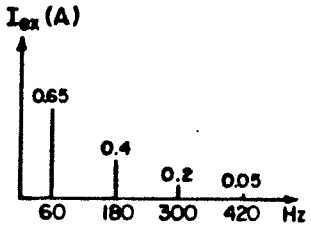

(d) Amplitude Spectrum of i_{ex}
GIC = 0 pu

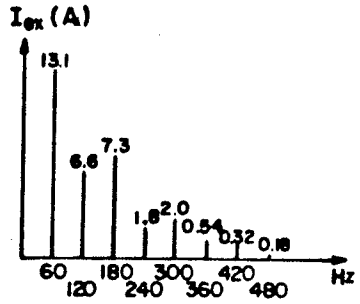

(e) Amplitude Spectrum of i_{ex}
GIC = 0.22 pu

FIGURE 4.1 Open-circuit behaviour of T1 under GIC conditions.

closed circuit loop to allow simulating a GIC condition by using a dc voltage source (denoted as GIC) connected in series with the transformer windings. T1 and T2 are energized by two identical sinusoidal voltage sources. The source impedance of each voltage source can be assumed to be small. The following are the general qualitative observations with respect to T1 at no load and under GIC conditions:

(1) The primary winding terminal voltage of T1 drops slightly when GIC is applied. The value of the voltage drop depends on the magnitude of GIC and on the source impedance.

(2) The waveform of the primary terminal voltage distorts slightly. The degree of distortion depends on the magnitude of GIC and on the source impedance.

(3) The dynamic hysteresis loop is offset. No increase in area of the loop is observed (see Figure 4.1(c)).

(4) The amplitude spectrum of the exciting current of T1 contains odd and even current harmonics (see Figure 4.1(e)).

(5) There is excessive increase in VAr demand and moderate increase in power loss. The power factor of T1 decreases considerably with increasing GIC.

(6) The true rms value of the exciting current increases with increasing GIC and the level of noise generated by the transformer also increases.

(7) No increase of temperature rise in the core is detectable.

(8) Very slight temperature rise in the primary winding is noted with increasing GIC.

(9) The core is driven into saturation during one-half of each cycle.

(10) The stray field (**ac + dc**) in air increases initially with increasing GIC, and its rate-of-increase diminishes as deep asymmetrical core saturation approaches.

(11) The ampere-turns in each set of the winding are no longer equal under GIC conditions.

(12) When fully loaded, the transformer is still functioning and is capable of delivering the required amount of power to the load. Under such conditions, slight increase in winding temperature is noted.

The observant reader may be surprised that there is no failure of the transformers in the course of the experiment. This is a very sound observation. However, an answer to this requires a little further experimental evidence as well as theoretical explanation.

The obvious effects of GIC on a transformer, as revealed by this experiment, are to cause an additional increase in exciting current and in ac plus dc magnetic field. Whereas the load current (if any) remains fairly constant as long as there is no increase in load under GIC conditions. In fact, the experiment shows that the load current reduces slightly due to a slight drop in transformer terminal voltage.

It is conceivable that any drastic increase in exciting current (especially when the transformer is at the full load condition) could cause possible overheating in the transformer windings. But this type of overheating scarcely deserves to rank as localized

overheating, since heat generated by this additional current is distributed uniformly along the complete length of the winding. It would therefore be proper to suggest that overheating in windings (if any) is permissible[10] and is quite adequately protected by existing transformer temperature relays.

In order to examine any possible localized overheating in structural parts due to an increase in magnetic field, it is convenient to separate the field outside the closed iron core into two basic components: leakage field and stray field. Leakage field is the field closely associated with the term "leakage reactance" of a transformer, and its magnitude depends on the load current through the transformer only and is derived by ignoring the magnetizing current. Stray field on the other hand is the field that is the sum of the fields due to magnetizing current and due to the magnetized iron. The stray field is the "$\bar{B}$" discussed fully in Chapter III.

Thus, the stray field and the field in the iron always exist irrespective of loading conditions of the transformer whereas the leakage field is present only when the transformer is on load. Actually, there is, of course, only one field outside the iron core when the transformer is under load, and the heating effects in structural parts must be derived from this total field. However, as has been mentioned earlier, the load current remains fairly constant under GIC conditions. It follows that the leakage field is fairly constant as well. Thus, the extent of localized heating in structural parts can be determined by examining whether the stray field could be large enough to cause a drastic increase in the total field outside the iron core.

The remainder of this chapter will therefore centre on experimental investigations on the stray field of an open circuit transformer under GIC conditions.

4.2 Experimental Apparatus

The overall experimental set-up for various measurements is shown in Figure 4.2. Figure 4.3 gives experimental circuitry of the set-up. A total of 6 single-phase, 3-kVA, 120:120 volts, shell-form transformers were used in this experiment. The GIC condition was simulated using two 300-watt dc-amplifier voltage sources, each of 20 A rating, and were connected in parallel as a unit. The unit (denoted as GIC) was then connected in series in the neutral line of the system. Figures 4.4 and 4.5 give detailed construction of the transformers T4, T5, and T6. Figure 4.6 shows detailed dimensions of T4 and point coordinates where fields were measured.

The true power P_{in}, true rms exciting current I_{ex} and GIC current I_{GIC} of T4 were measured using an unconventional watt-meter, true rms ammeter and dc ammeter respectively. All the meters were constructed using functional operational amplifier blocks that are available from an anolog computer TR 48 manufactured by Electronic Associates Incorporated. The functional blocks that performed these measurements are given in Figure 4.7. The metering signals that go to the analog computer are derived from a potential divider consisting of resistors R_1 and R_2 (see Figure 4.7(a)) and a current shunt of 0.001 Ω , 300 A of zero-inductance: resistor R_S.

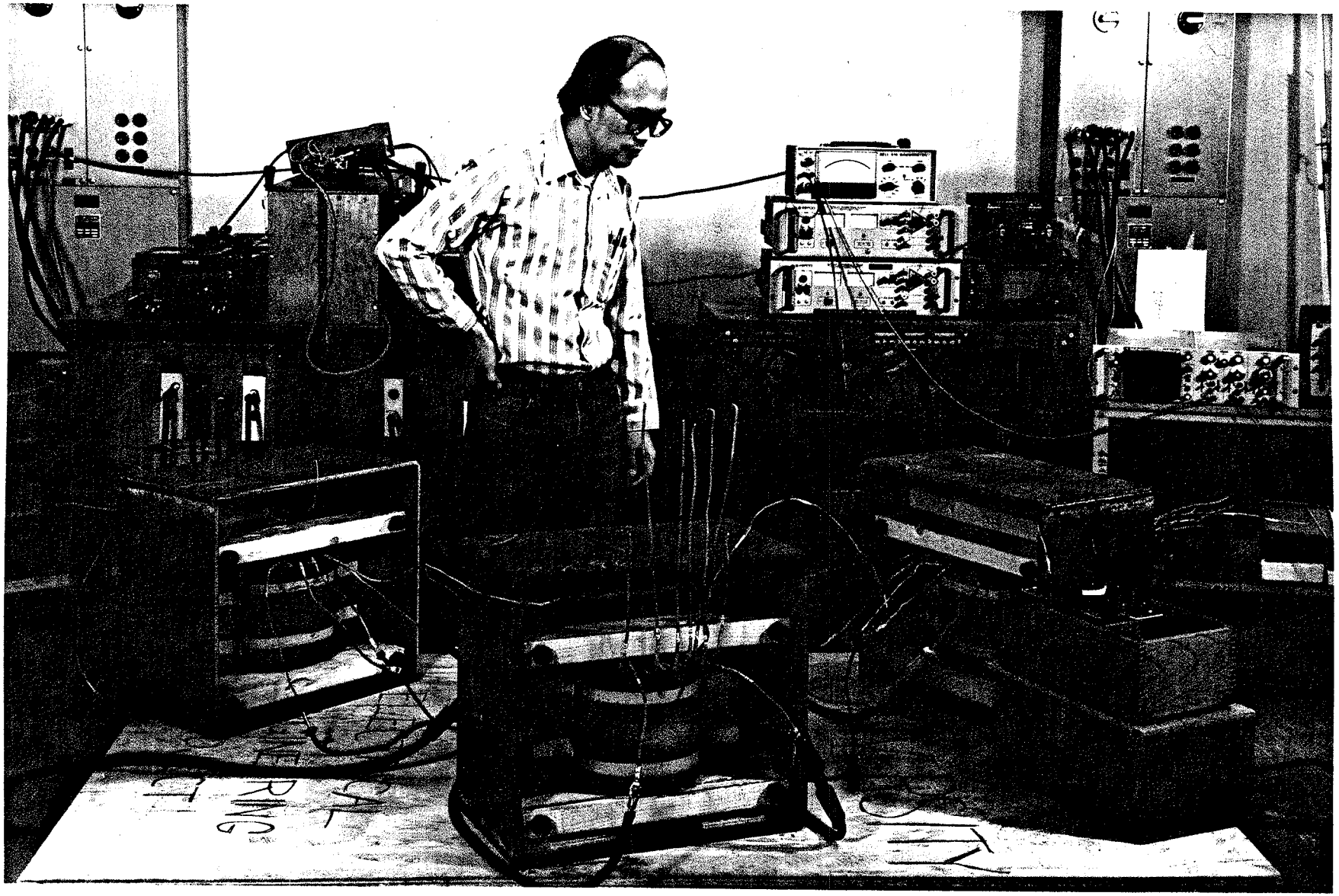

FIGURE 4.2 Photo showing overall experimental set-up.

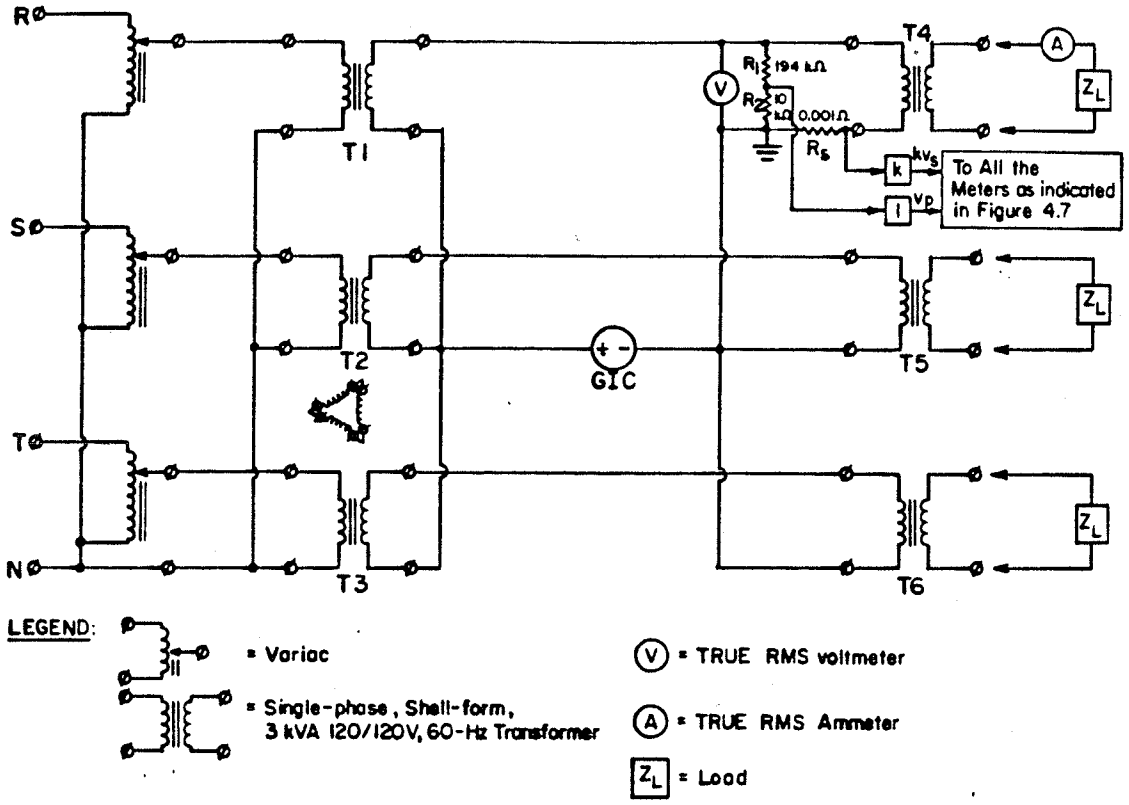

NOTE: Normal true rms exciting current of T4 = 0.42 A.

FIGURE 4.3 Circuit diagram for experimental investigations.

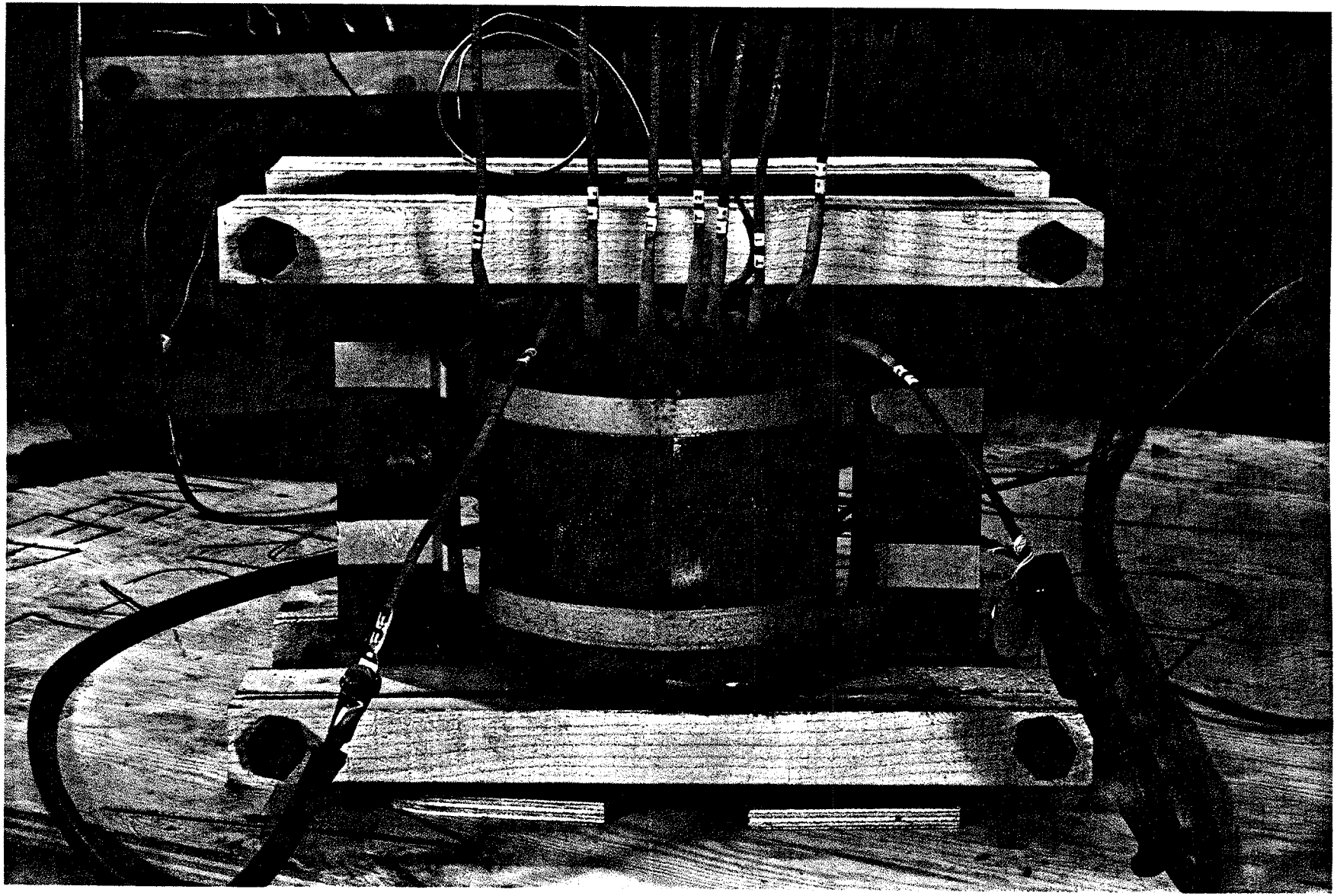

FIGURE 4.4 Photo showing construction of T4, T5 and T6. All without tie plates, base plates, bolts, nuts, clamps and tank.

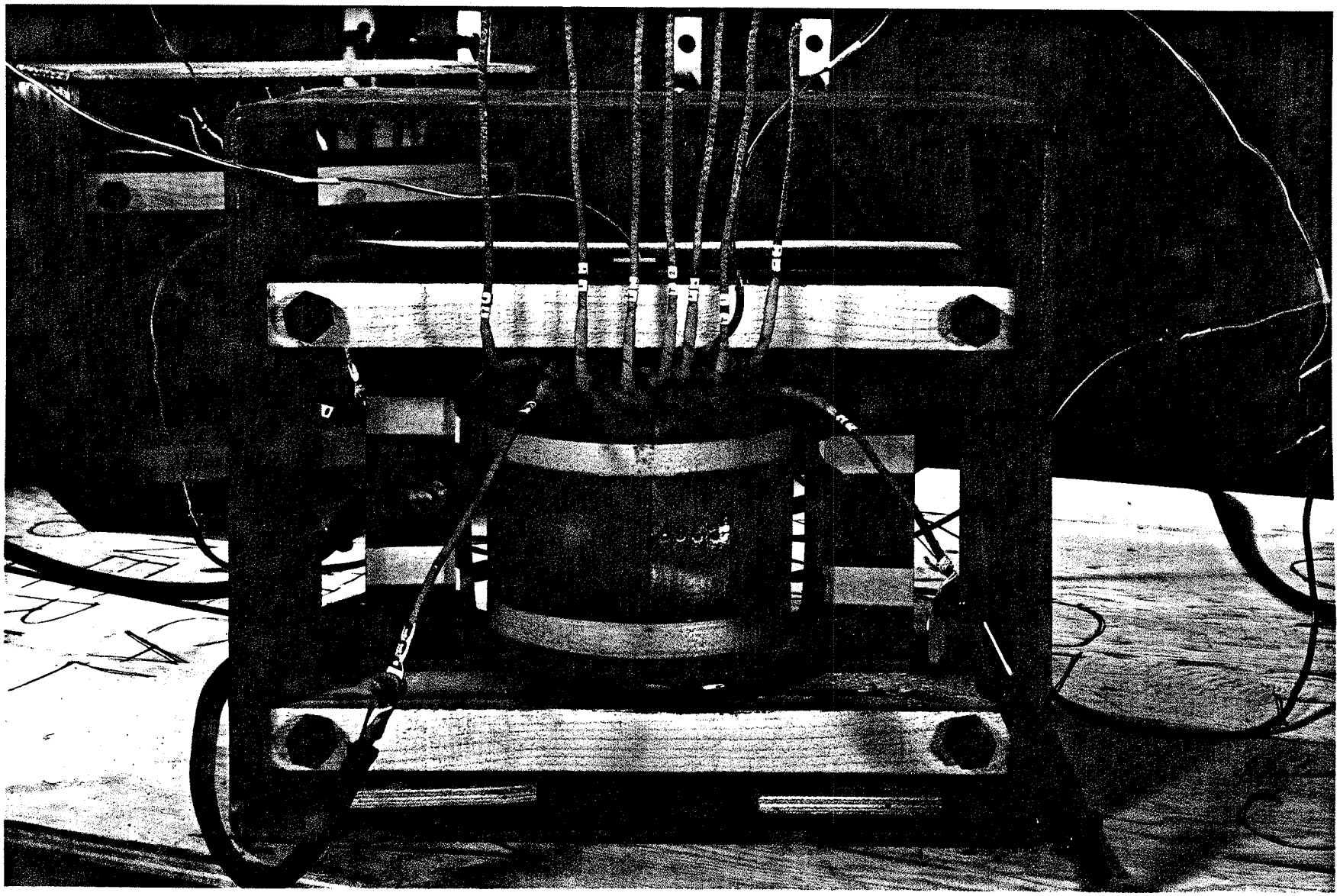

FIGURE 4.5 Photo showing tank in position. Note: Other structural members are to be added as required.

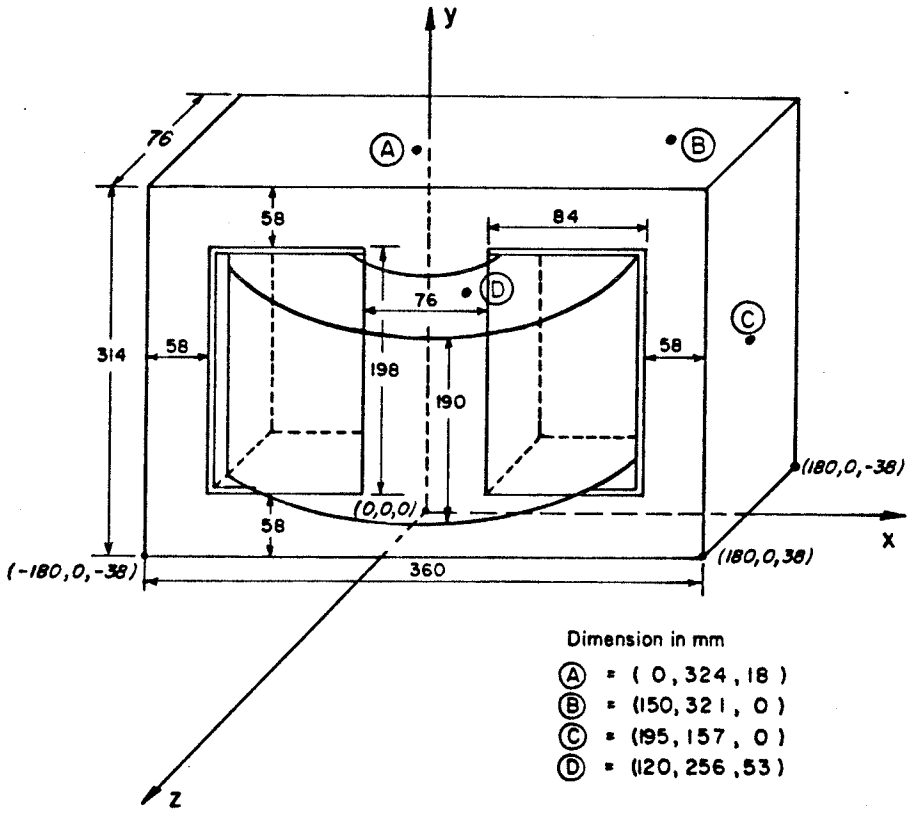

FIGURE 4.6 Detailed dimension of T4 and point coordinates for field measurements.

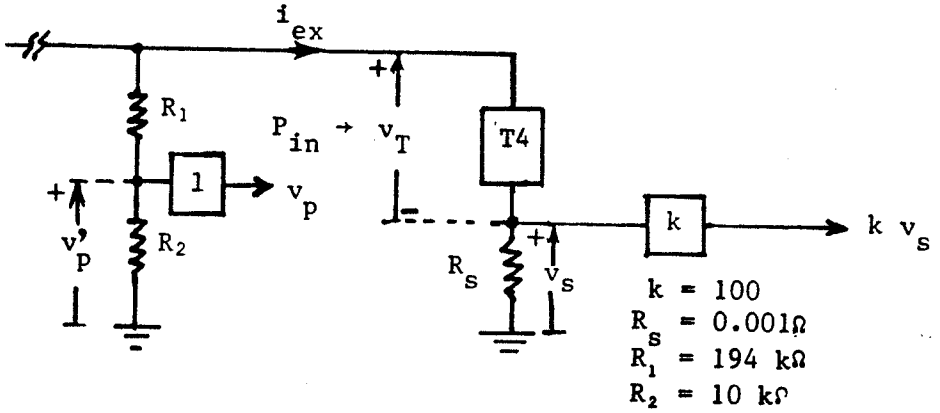

FIGURE 4.7(a) **Circuit showing signals to block diagrams** (b), (c) and (d).

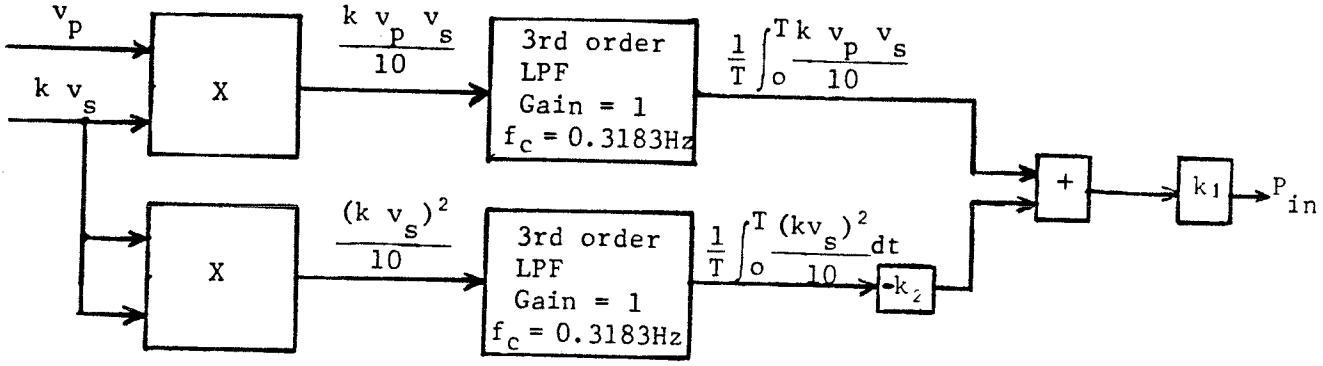

where P_{in} is total power input into transformer T4 and is given by

$$P_{in} = \frac{1}{T}\int_o^T v_T\, i_{ex}\, dt$$

$$= \frac{10(R_1 + R_2)}{k(R_2\ R_s)}\left[\frac{1}{T}\int_o^T \frac{kv_p v_s}{10}\, ds - \frac{kR_2}{R_1 + R_2}\,\frac{1}{T}\int_o^T \frac{v_s^2}{10}\, dt\right]$$

$$= k_1\left[\frac{1}{T}\int_o^T \frac{kv_p v_s}{10}\, dt - k_2\,\frac{1}{T}\int_o^T \frac{(kv_s)^2}{10}\, dt\right] \qquad (4.1)$$

where $k_1 = \dfrac{10(R_1 + R_2)}{k\ R_2 R_s}$

$$k_2 = \frac{R_s}{k(R_1 + R_2)}$$

FIGURE 4.7(b) **A wattmeter.**

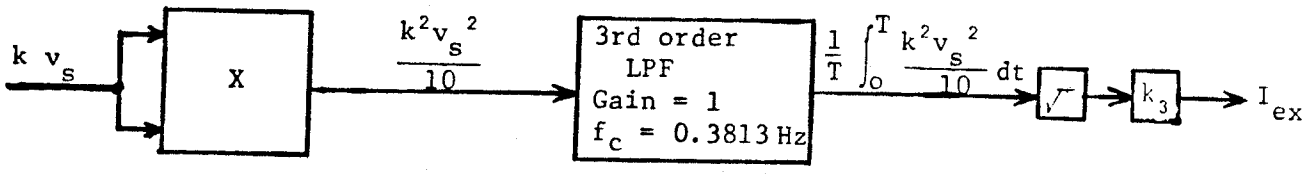

where: I_{ex} is the <u>true</u> rms of i_{ex} and is given by

$$I_{ex} = k_3 \sqrt{\frac{1}{T}\int_o^T \frac{k^2 v_s^2}{10}\,dt}$$

$$= k_3 \frac{k\,R_s}{\sqrt{10}} \sqrt{\frac{1}{T}\int_o^T i_{ex}^2\,dt}$$

$$= \sqrt{\frac{1}{T}\int_o^T i_{ex}^2\,dt} \qquad \text{if} \quad k_3 = \frac{\sqrt{10}}{k\,R_s} \tag{4.2}$$

FIGURE 4.7(c) A true rms ammeter.

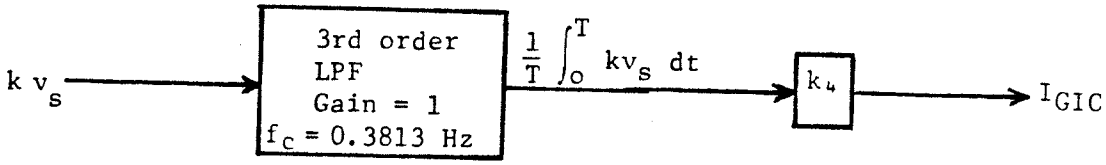

where: I_{GIC} is the magnitude of GIC current and is given by

$$I_{GIC} = k_4 \frac{1}{T}\int_o^T k v_s\,dt$$

$$= k_4 \cdot kR_s \frac{1}{T}\int_o^T i_{ex}\,dt$$

$$= \frac{1}{T}\int_o^T i_{ex}\,dt \qquad \text{if} \quad k_4 = \frac{1}{k\,R_s} \tag{4.3}$$

FIGURE 4.7(d) A dc ammeter.

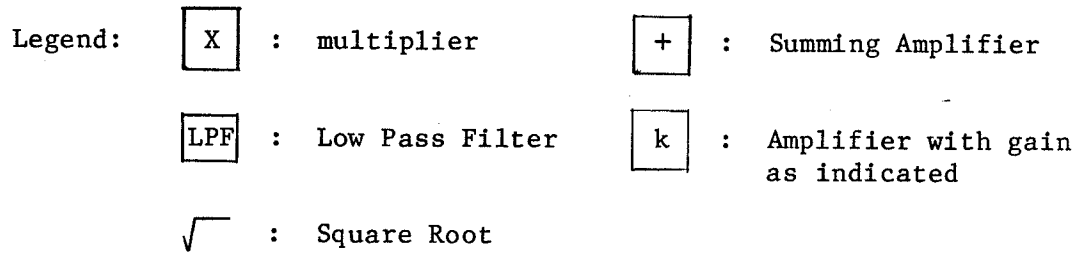

FIGURE 4.7: Block Diagrams of Instrument Meters in an Analog Computer.

The set-up in Figure 4.3 offers accurate measurements because the loading effect in the measuring circuit is minimized. Moreover, all the inherent measuring limitations (for instance, limited power factor range and frequency range of a dynamo-type wattmeter) that are associated with conventional meters are eliminated when using the measuring scheme in Figure 4.3.

All meters in the analog computer were tested and calibrated before measurements were taken. The calibration factors derived from tests are in good agreement with those derived from calculations.

Magnetic field measurements were performed using a precision magnetic measuring instrument: F. W. Bell model 610 Gaussmeter equipped with a Hall-Effect flux probe.

For magnetic field waveform recording, an external cathode-ray oscilloscope was used in connection with the Gaussmeter so that the waveform of the field could be recorded.

Temperature measurements in structural parts due to stray field and leakage field were taken using a Tektronix DM 502A auto-ranging digital multimeter equipped with the P6601 temperature probe. Two nos 325 mm x 25 mm x 13 mm hot-rolled mild steel rectangular iron bars were placed in T4 in areas where field intensity appeared to be

the highest. The arrangements of the iron bars are shown in Figure 4.8.

4.3 Method of Measurement

A 3-phase, 60-Hz, 120 volts rated ac voltage was applied to the terminals of T4, T5 and T6 whenever any measurements were performed. Once the terminal voltages of these transformers were set at 120 volts, no adjustment in terminal voltages was made over the entire process of the measurements. The GIC condition was simulated simply by varying the output of the dc voltage source.

The measurements of ac component of the magnetic field were accomplished by the following steps applicable to the gaussmeter[33]: (Assume that an ac + dc field existed at the point of measurement)

(i) Depending on the direction of the dc field component, the function switch would be either in NOR (normal) or REV (reverse) position.

(ii) If the function switch were in the correct position, the Gaussmeter panel meter would give an up-scale reading.

(iii) Reduce the reading to zero using the zero control.

(iv) Turn the function switch to the ac position to read the rms value of the ac component of the field.

Recording the waveform of the field was accomplished using external oscilloscope connected to the output jacks of the gaussmeter. A true waveform of the field would appear at the oscilloscope screen whenever the function switch was either in NOR or REV position.

Power loss measurements, the magnitude of GIC, true power and true RMS exciting current of T4 were measured using the dc

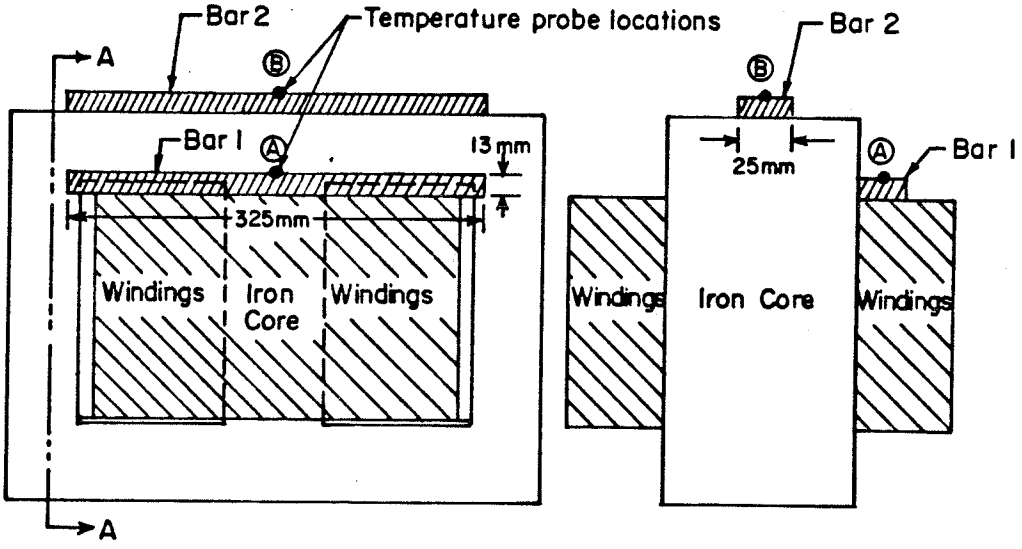

FIGURE 4.8 Arrangements of solid iron bars for temperature measurements.

ammeter, wattmeter and an ac ammeter respectively all through the analog computer.

Temperature measurements follow a straighforward procedure and will not be elaborated here.

When performing these measurements, it is important that the normal saturation behaviour of T4 be preserved and not be affected by possible different saturation taking place in T5 and T6. This is achieved using the voltage source (denoted as GIC in Figure 4.3) which has a practically zero source impedence. The zero impedance voltage source would allow zero sequence current as well as unbalance current (if any) to flow in the neutral of the system. As such, the normal saturation behaviour of T4 would in no way be affected by the presence of T5 and T6.

4.4 Results and Discussion

4.4.1 Magnetic Field Measurements

The results presented in this subsection were obtained when transformer T4 was at no load and under GIC conditions. Also T4 contained no structural parts so that field disturbances from these structural parts were minimized.

It has been mentioned in Section 4.1 that a transformer under a GIC condition establishes a stray field consisting of both ac and dc components. Here, only the ac component of the stray field will be covered in detail because it is this component of the field that causes so-called eddy current and hystereis losses in structural parts.

Figure 4.9 shows how the y-component of the ac stray field, B_y^{ac} at points A and C changes as a function of GIC. The coordinates of points A and C are given in Figure 4.6. The ac exciting current is also included in this figure. Note that x-components of the stray field at the points are not shown because their values are practically zero.

It can be seen from Figure 4.9 that at point A the stray field B_y^{ac} increases initially and then shows almost no further increase with increasing GIC. Its value at GIC = 13 A is only 5.6 gauss and the total exciting current is 1.04 pu of rated load current. A field of this magnitude would not give rise to any overheating of structural parts. This will be borne out by further experimental evidence in Section 4.4.3. A check on the magnitude of B_y^{ac} around the iron core (except in the region directly on top of the magnetizing winding and the region inside the iron window) was performed and it was found that 5.6 gauss at point A is the highest value.

In order to explain why the stray field outside the iron core cannot be high when GIC is high, some stray field waveforms B_y (note: dc component is now included) at point A were observed and are shown in Figure 4.10. The exciting current waveforms i_{ex} are also included in these figures except in Figure 4.10(b) where it is not shown for the sake of clarity. In Figures 4.10(a) and 4.10(b) the iron core is below deep saturation conditions because the magnetizing current is small, whereas in Figure 4.10(c) the iron core is in deep saturation.

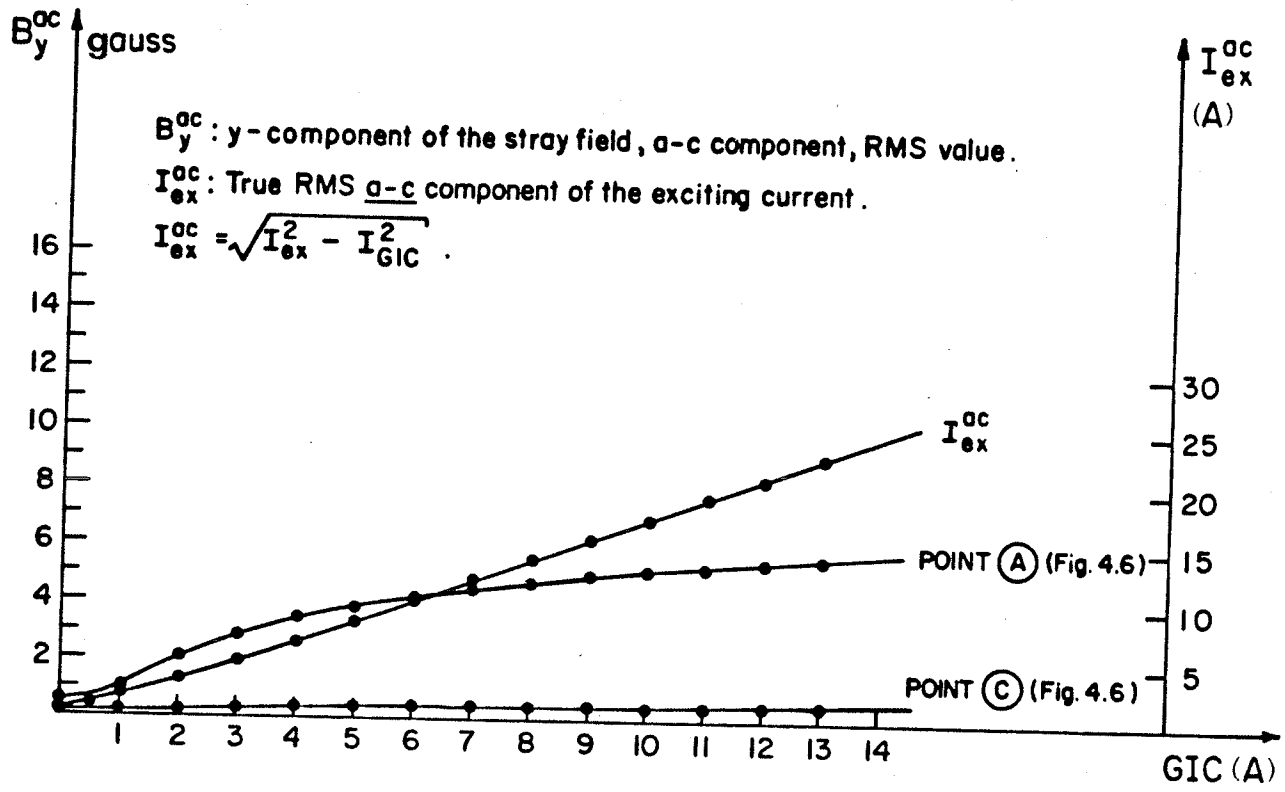

FIGURE 4.9 Stray field and exciting current of T4 under GIC conditions.

Remarks

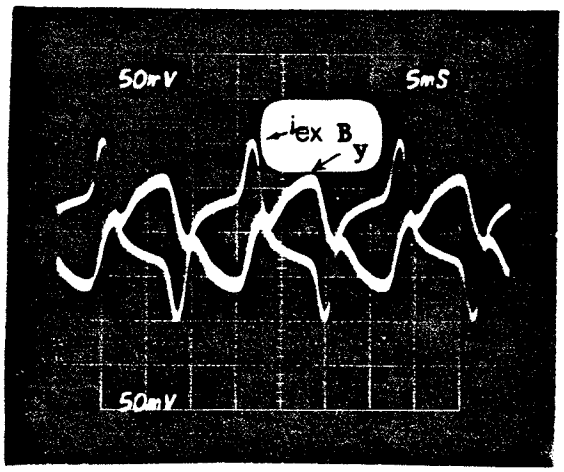

(a) i_{ex} included.

Function switch in Gaussmeter panel in NOR position.

GIC = 0 A , B_y^{ac} = 0.67 G

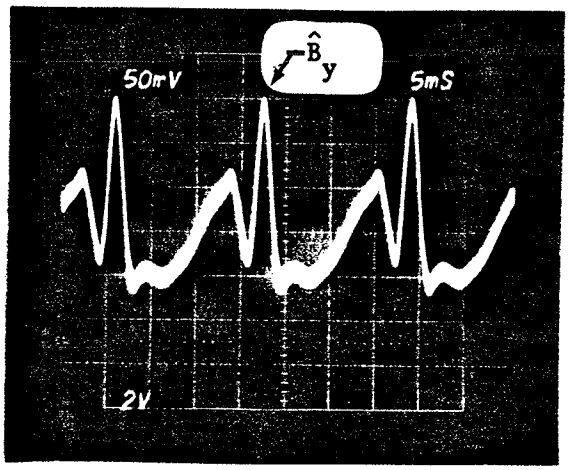

(b) i_{ex} not included.

Function switch in REV position.

GIC = 1.55 A , B_y^{ac} = 0.765 G

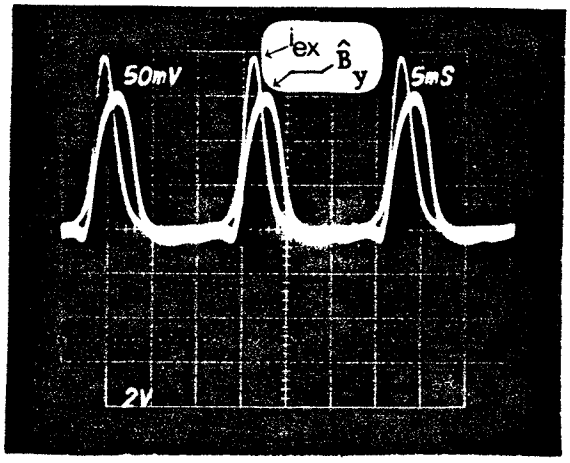

(c) i_{ex} included.

Function switch in REV position.

GIC = 13 A , B_y^{ac} = 5.6 G

NOTE: (1) Top voltage scale for B_y.

(2) Bottom voltage scale for exciting current i_{ex}.

(also applicable to Figures 4.13, 4.14 and 4.15)

FIGURE 4.10 Waveforms of B_y and i_{ex} at point A.

The important properties of the stray field outside the closed iron circuit as given in Chapter III can now be fully applied to explain the waveforms in Figure 4.10. They are summarized as follows for easy reference:

(i) When the iron core is below deep saturation, B^m is dominant over B^c (Recall that $\bar{B}_m = \mu_o \bar{H}^m$ and $\bar{B}_c = \mu_o \bar{H}^c$ outside the iron core).

(ii) When the iron core is in deep saturation, B^m decreases to a negligible value.

(iii) Because of properties (i) and (ii), the rate-of-increase in stray field B (where $\bar{B} = \bar{B}^c + \bar{B}^m$) diminishes to a near constant which is solely dependent upon B^c as the iron core approaches deep saturation.

(iv) The iron in the region surrounded by the magnetizing winding saturates before other parts of the iron.

(v) Once the iron in the region surrounded by the magnetizing winding has been saturated, any additional increase in H there must still be derived from the interaction between $\bar{H}^c$ and $\bar{H}^m$, not from $\bar{H}^c$ only.

Now refer to Figure 4.10. The waveform of the stray field B_y of a below-deep-saturation iron core are complicated as can be seen from Figures 4.10(a) and 4.10(b). Clearly the iron field $\bar{B}^m$ must dominate the current field $\bar{B}^c$ to cause such complicated waveforms. Such waveforms are not however of concern here because their magnitudes are extremely small (i.e. $B_y = 0.67$ G in Figure 4.10(a) and $B_y = 0.76$ G in Figure 4.10(b)).

Note that the exciting current waveform i_{ex} in Figure 4.10(b) was not recorded. However, knowing that GIC = 1.55 A in Figure 4.10(b) and that GIC = 13 A in Figure 4.10(c), one can readily observe from Figure 4.9 that the rms value of the ac component of the exciting current I_{ex}^{ac} in Figure 4.10(b) is about one-tenth of that for Figure 4.10(c) (i.e. I_{ex}^{ac} for Figure 4.10(b) is equal to 2.25 A , and I_{ex}^{ac} for Figure 4.10(c), 22.5 A). This clearly infers that the peak value of the magnetizing current for Figure 4.10(c) is very much greater than that for Figure 4.10(b). Such an inference leads to

$$\hat{B}_y^c \text{ [for Figure 4.10(c)]} >> \hat{B}_y^c \text{ [for Figure 4.10(b)]} , \qquad (4.4)$$

where $\hat{B}_y^c$ denotes the peak value of the y-component of the field $\bar{B}^c$ due to the peak value of the magnetizing current.

Notice that the maximum value of B_y (denoted as $\hat{B}_y$) in Figure 4.10(c) is about the same as that in Figure 4.10(b), i.e.

$$\hat{B}_y \text{ [in Figure 4.10(c)]} \simeq \hat{B}_y \text{ [in Figure 4.10(b)]} . \qquad (4.5)$$

Since the condition $\hat{B}_y = \hat{B}_y^c + \hat{B}_y^m$ must hold, and from (4.4) and (4.5), one concludes that

$$\hat{B}_y^m \text{ [in Figure 4.10(c)]} << \hat{B}_y^m \text{ [in Figure 4.10(b)]} . \qquad (4.6)$$

Since the x-components of $\bar{B}^c$ and $\bar{B}^m$ at point A are practically zero, the expression (4.6) means that closed iron core spills less iron flux rather than more flux when the iron is in a deep saturation condition and hence is a result of property (ii).

Because of properties (i) and (ii), the peak value of the stray field B_y increases very little with increasing GIC.

Another important factor that prevents the stray field from increasing drastically is due to a much slower increase in biasing flux density B_{dc}^{I} (see Figure 4.11) when GIC is high. Before elaborating further on this important concept, a brief comment on Figure 4.11 will be necessary.

Figure 4.11 shows how the stray field waveform B_o can be constructed graphically with the help of the B-versus-I curves. The B-versus-I curves for this particular transformer must be derived based on a similar study for the iron ring discussed in Chapter III, because the two have different core configurations and material characteristics. For qualitative analysis, though, there is no doubt that the behaviour of the curves will be similar. Note that core loss current has been omitted for the sake of simplicity.

It is interesting to note from Figure 4.11 that the magnetizing current waveform is derived from the B_I waveform through the use of the B_I-versus-I curve (lower section of Figure 4.11) whereas the stray field waveform is derived from the magnetizing current waveform through the use of the B_o-versus-I curve. Another interesting point is that the point P (corresponds to B_{dc}^{I}) coincides with Q (corresponds to I_{GIC}) only and that R (corresponds to B_{dc}^{o}) coincides with S (corresponds to I_{GIC}) only when B_{max} is zero. Earlier literature[1,7] assumes that P and Q coincide while Aubin and Bolduc[12] pointed out that point P cannot be readily inferred from point Q (but no further explanation was given by

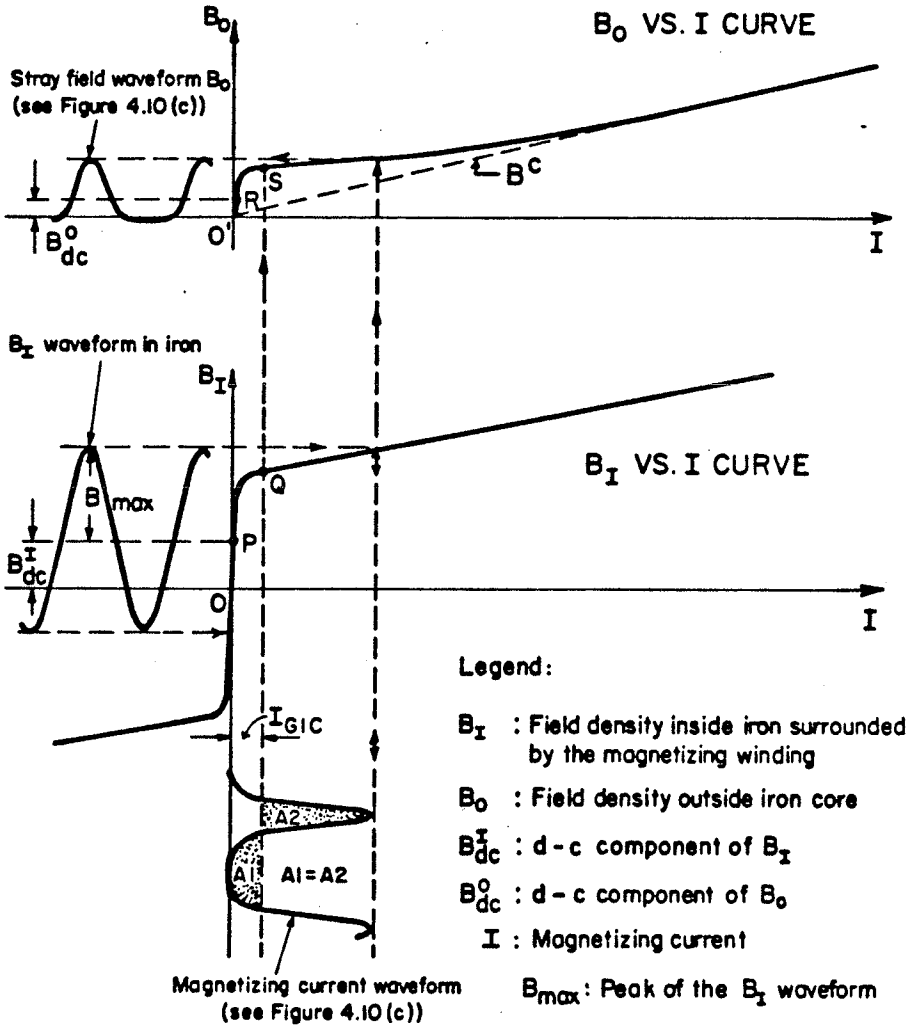

FIGURE 4.11 Graphical method of constructing stray field waveform (Qualitative).

them). A recent paper by Emanuel[35] gives an expression to determine point P for a CT with steady-state dc biasing. Thus, for steady-state conditions, the point P establishes itself at the level for which the dc component of the magnetizing current equals the magnitude of the GIC, I_{GIC} :

$$\frac{1}{T}\int_0^T N_1 (i_{ex} - i_c)\, dt = N_2 I_{GIC} , \qquad (4.7)$$

Where N_1 is the number of turns of the winding in which the exciting current i_{ex} and core loss current i_c flow, and N_2 is the number of turns of winding in which the GIC flows. For the circuit arrangements of Figure 4.3, $N_1 = N_2$, thus (4.7) becomes

$$\frac{1}{T}\int_0^T (i_{ex} - i_c)\, dt = I_{GIC} \qquad (4.8)$$

Now it is clear from expression (4.8) and Figure 4.11 that once iron in the region surrounded by the concentrated magnetizing winding has been saturated (i.e. property (iv)), a further slight increase in the biasing flux B_{dc}^I will cause a very large single-sided magnetizing current and thus its d-c component fulfills the requirement of equation (4.8). This means that a very large GIC amphere-turns ($N_2 I_{GIC}$) will cause only a small increase in B_{dc}^I .

Thus, once the iron in the region surrounded by the magnetizing winding has been saturated, the biasing flux B_{dc}^I increases in a very much slower manner with increasing GIC. Accordingly, the exciting current increases only moderately with increasing GIC as can be seen from Figure 4.9. It must be pointed out here that the magnitude of the exciting current would be extremely

high if one failed to take into account

- Properties (iv) and (v), and

- that P does not coincide with Q in Figure 4.11.

It is now very clear from Figures4.9, 4.10 and 4.11 that the stray field outside the iron core can never be high even if GIC has caused an increase in exciting current to a level which is equal to 1 pu (rated load current as base). An immediate question is: What if GIC Ampere-turns is so high that it causes the exciting current to exceed more than 1 pu rated load current?

An answer to this question is that the ac stray field still remains fairly small as can be inferred from Figure 4.12. The ac stray field waveform now moves further upwards and remains there as a result of properties (i), (ii) and (iii). This point is illustrated in Figure 4.12.

It must, however, be pointed out that exciting current of magnitude higher than 1 pu would certainly give rise to an immediate system operating problem[2,15] which will not be discussed here. Moreover, winding overheating may present a problem if the transformer is under full load conditions. Note that exciting current of magnitude equal to or less than 1 pu does not necessarily imply that there is no system operating problem or winding overheating because the RMS value of the sum of the exciting current and the load current may be greater than 1 pu. Here "1-pu exciting current" is adopted as a guideline meaning that no structural parts overheating whatever occurs in a transformer under a GIC condition if exciting current is below 1 pu. This important observation will be borne out by further experimental evidence in Sections 4.4.2 and 4.4.3.

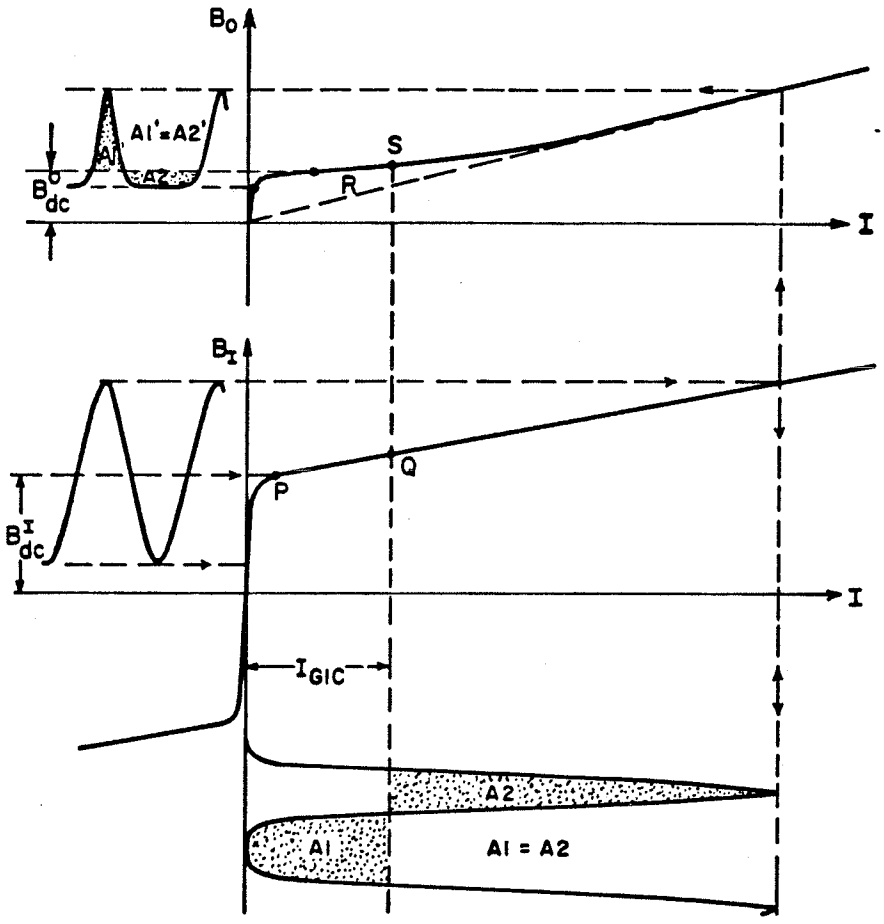

Note : For legend refer to Figure 4.11

FIGURE 4.12 Stray field waveform B_o under extremely high GIC conditions (an unrealistic assumption).

For completeness, Figures 4.13, 4.14 and 4.15 show the stray field waveform B_y at points B, C and D respectively. In all the cases, the rms values of the B_y^{ac} are small (even at point D where B_y^{ac} is 38.0 G at GIC = 13 A). Such a small stray field, when added to the leakage field, certainly would not cause structural parts overheating. The temperature measurements in Section 4.4.3 will confirm this.

4.4.2 Power Loss Measurements

The foregoing section shows that the ac stray field outside the iron core T4 under GIC conditions is small in magnitude. It also indicates that the field is not only nonuniform but also nonsinusoidal, and moreover, it contains a dc component. There is no doubt that existing available methods for computing eddy-current losses in solid iron (most of them based on an assumption that the field is uniform and sinusoidal) like those given by Tudbury[36], Agarwal[37], Stoll[38] and Lim and Hammond[39] cannot be applied to compute the losses in structural parts under such non-sinusoidal and nonuniform conditions. In view of the difficulty in computing these losses, two further experiments were performed to check the extent of heating effects in structural parts due to the nonsinusoidal field.

4.4.2.1 Power Losses in Core and Windings

Power losses in iron core P_{co} (due to eddy current and hysteresis losses) and power losses in conductor windings P_{es} (due to eddy current and skin effect only) are measured as a whole in this test. They are given by the expression

$$P_{co} + P_{es} = P_{in} - R_1 I_{ex}^2 \quad \text{(at no load)} \tag{4.9}$$

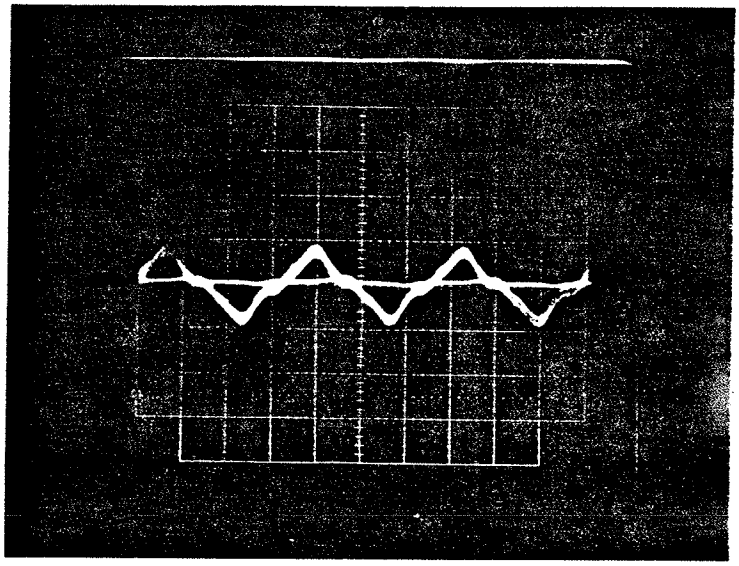

(a) GIC = 0 A , B_y^{ac} = 0.2 G , i_{ex} not included.

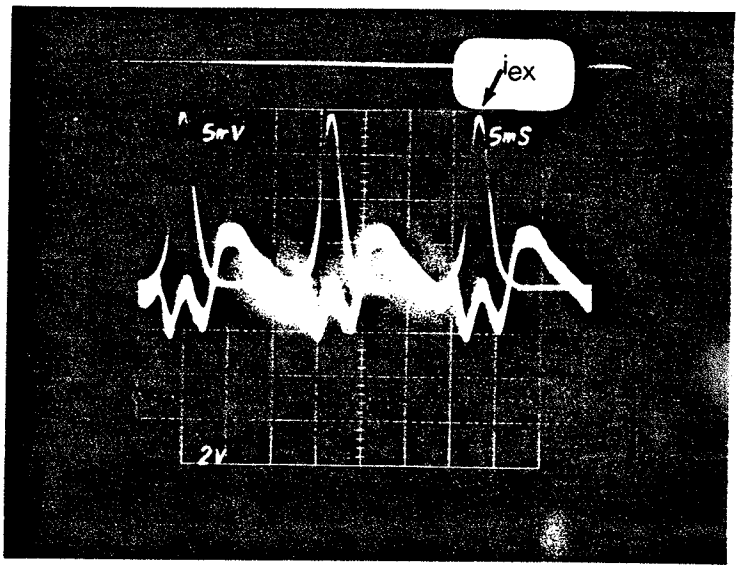

(b) GIC = 13 A , B_y^{ac} = 0.36 G , i_{ex} included.

FIGURE 4.13 B_y waveforms at point B.

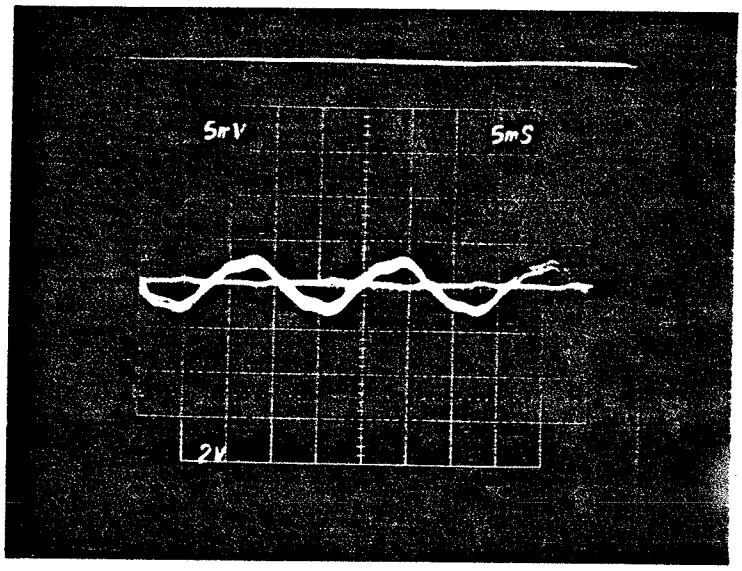

(a) GIC = 0 A , B_y^{ac} = 0.2 G , i_{ex} not included.

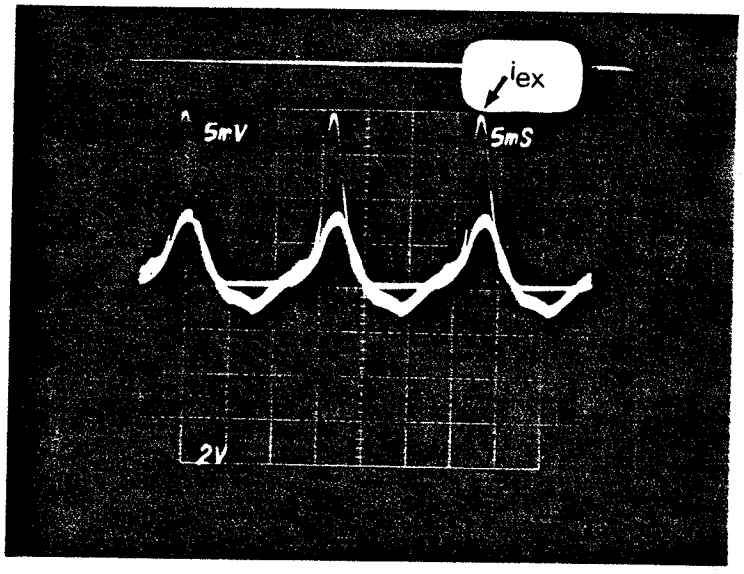

(b) GIC = 13 A , B_y^{ac} = 0.33 G , i_{ex} included.

FIGURE 4.14 B_y waveforms at point C.

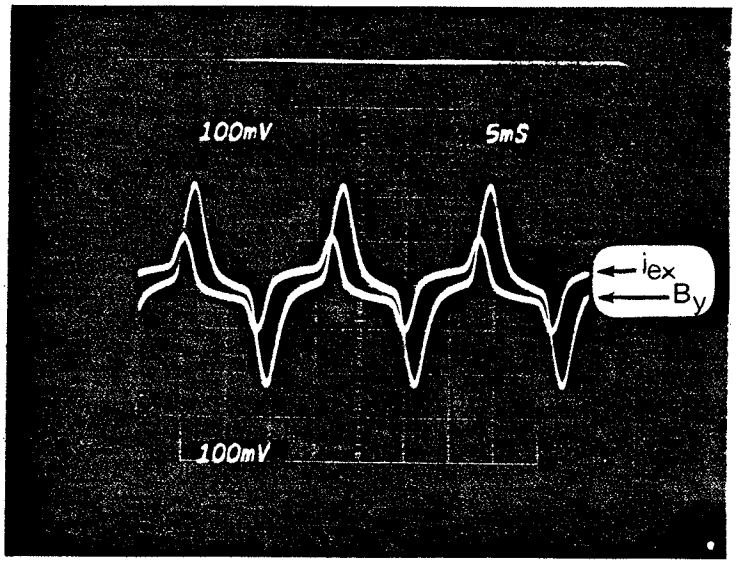

(a) GIC = 0 A , B_y^{ac} = 0.95 G , i_{ex} included.

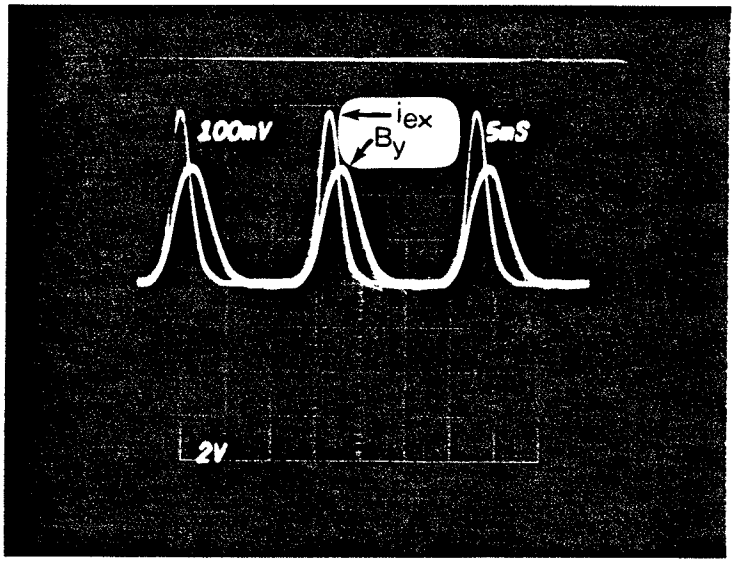

(b) GIC = 13 A , B_y^{ac} = 38.0 G , i_{ex} included.

FIGURE 4.15 B_y waveforms at point D near the magnetizing winding.

where P_{in} is the real power into the transformer T4, I_{ex} is the total true rms exciting current, and R_1 is the dc resistance of the primary winding. Here R_1 takes the value of 0.056 Ω when measured with a Wheastone Bridge.

The test circuitry is shown in Figure 4.3. All structural parts in transformers T4, T5 and T6 were taken out (see Figure 4.4). While varying the GIC current, the values of P_{in}, I_{ex} and I_{GIC} were read from respective meters on the analog computer.

Figure 4.16 shows the results of the test. Three curves representing P_{in}, $R_1 I_{ex}^2$ and $P_{co} + P_{es}$ as a function of I_{GIC} are plotted in Figure 4.16. It can be seen from Figure 4.16 that $P_{co} + P_{es}$ increases only slightly with increasing GIC. For instance, $P_{co} + P_{es}$ = 20.31 watts at GIC = 0.0 Amp, and $P_{co} + P_{es}$ = 28.69 watts at GIC = 13 A in which case I_{ex} = 1.04 pu (25 A as base). This immediately leads to the following conclusions:

(a) No overheating whatever occurs in the transformer core under a GIC condition.

(b) Losses in the winding due to eddy current and skin effect slightly increases with increasing GIC.

(c) The I^2R loss in the winding increases considerably when GIC is high.

It is clear that total power losses in the windings due to items(b) and (c) above will present a winding overheating problem if GIC is extremely high.

4.4.2.2 Power Losses in Structural Tank

In this laboratory test, the experimental details were all the same as that of the foregoing section except that the iron tanks

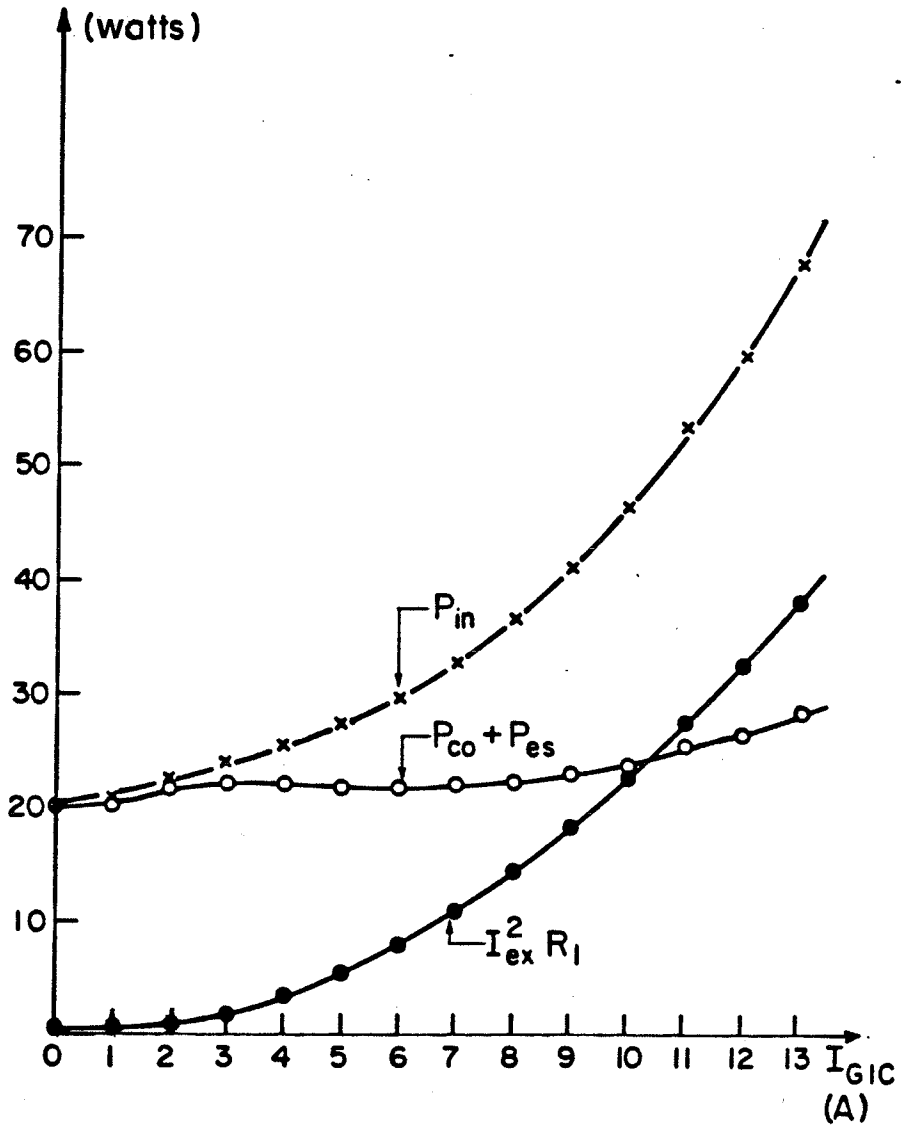

FIGURE 4.16 Power losses versus I_{GIC}.

were restored in original position for transformers T4, T5 and T6 (see Figure 4.5). The power losses in structural tank P_t together with the P_{co} and P_{es} are measured as a whole in this test. The expression is

$$P_t + P_{co} + P_{es} = P_{in} - R_1 I_{ex}^2 \quad \text{(at no load)} \tag{4.10}$$

Figure 4.17 presents a result obtained from the test. The curve $P_{co} + P_{es}$ in Figure 4.16 is included in Figure 4.17 for comparison purposes.

It is rather surprising from Figure 4.17 that the total power losses in structural tank hardly show signs of increasing with increasing GIC. How has this come about?

The reasons are straightforward and are given as follows:

(a) The stray field outside the iron core is small as has been indicated in Section 4.4.1.

(b) The stray field contained a dc component which (according to Woods' study on eddy-current losses in solid iron with DC offset[40]) tends to move the region of operation of the B-H curve into a partially saturated condition where the slope of the B-H curve is smaller and the effective skin depth is greater. The effect of the dc component is therefore to decrease slightly the power losses in the structural tank.

Other structural parts like clamps, tie-plates, bolts and nuts were restored to replace the wooden clamps in transformers T4, T5 and T6.

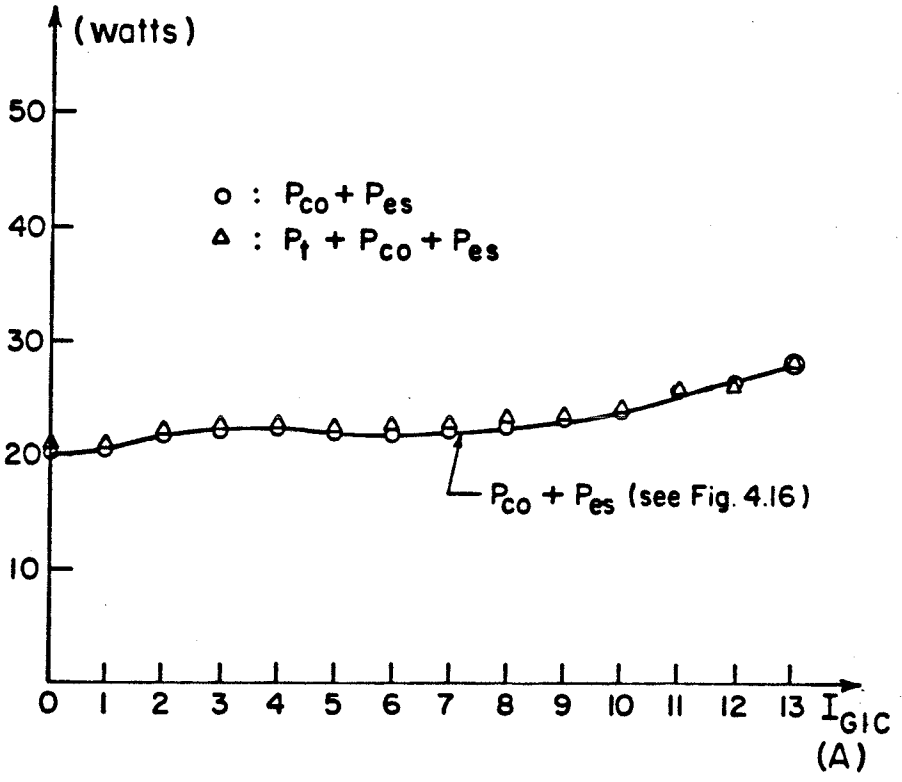

FIGURE 4.17 Power losses in transformer tank.

The test was then carried out with no load. It was noted from the wattmeter that the P_{in} readings showed very little change from the earlier set of P_{in} readings when the wooden clamps in the transformers were in place. The results obtained from the test were almost the same as those shown in Figure 4.17 and are therefore not shown here for further discussion.

The experimental evidence given in this section leads to conclude that overheating in structural parts under a GIC condition hardly exists because the power losses in these parts do not show any sign of increasing.

4.4.3 Temperature Measurements

As a final check and also for record purposes, the temperature measurements on structural parts were carried out in order to check the overall effect of the total field (i.e., stray field + leakage field) on structural part overheating.

A worst condition is selected where the two iron bars have the arrangement shown in Figure 4.8. Bar 1 is on top of the winding and bar 2, on top of the iron core. The points A and B in Figure 4.8 where temperatures were taken are the hottest temperature spots. Temperatures were taken while T4, T5 and T6 were fully loaded with a resistive load (power factor = 1.0) and the GIC was set at 13.0 A (a deep saturation condition). The total true rms current entering T4 primary winding was 36.89 A .

Table 4.1 shows the results obtained from the test. The two iron bars were exposed to the total field for about 85 minutes and the temperature for bar 1 increased from 24.4 °C to 33.0 °C whereas

bar 2 increased from 24.4 °C to 27.0 °C. Notice that the temperature rise as shown in Table 4.1 was solely due to the heating effect derived from the total field. The heating due to conduction and radiation from the core and windings were observed not to be the sources of the heating that caused the temperature rise in the iron bars.

It is rather surprising that the two iron bars are not overheated even under such unrealistic conditions.

TABLE 4.1: Temperatures at points A and B in Figure 4.8

Time: A.M.	9.40	10.15	10.20	10.50	11.05
Temp. at point A in °C	24.4	26.3	27.7	32.1	33.0
Temp. at point B in °C	24.4	24.4	25.6	26.0	27.0

CHAPTER V

DEVELOPMENT OF A PROTECTIVE DEVICE

It has been shown in Chapter IV that power transformer overheating of structural metal parts due to asymmetrical core saturation caused by GIC, is extremely unlikely. The chapter also shows that a normal operating power transformer shows signs of stress when subjected to GIC, e.g. a possible increase in winding temperature, an increase in exciting current containing odd and even harmonic components, and an increase in Var demand. Undoubtedly, they are all derived from one source, that is, asymmetrical core saturation due to GIC in the windings.

Many papers[2,15,41] have reported system operating problems due to GIC. One such problem is the misoperation of protection schemes, e.g. an overcurrent relay, installed to sense zero sequence 60-Hz current, could misoperate and cause an undesirable tripout under severe GIC conditions. Again, there is no doubt that the deep asymmetrical core saturation must cause this system operating problem.

It is therefore desirable to design a device to detect the level of asymmetrical core saturation for system operation purposes. In general, a system operator is only concerned with the harmful effects due to GIC on his operating system, not on the magnitude of the GIC. A device based on this viewpoint will enable him to judge whether or not system disturbances are due to GIC so that remedial measures could be taken before system integrity is jeopardized. This

information will also enable him to decide on the posibility of fast restoring of the disturbed system (if any) to its normal operating condition. On the other hand, the device can also assist him to immediately turn on a preventive device or to immediately block any mal-tripping arising from the disturbances, if necessary.

5.1 Indirect Measurement

At present, a common method used for detecting the presence of GIC involves a direct measurement method where the magnitude of the GIC is recorded by an expensive set-up. The set-up calls for, for example, a shunt or a Hall-Effect device to be installed in series with the neutral of the system or a dc-transducer in series with one of the three phase lines. Such an arrangement requires much modification and cabling work and down time for installation. The device described here, however, does not employ the direct measurement method. Instead, the device is a self-contained unit, that is connected directly in the existing CT secondary circuits (see Figure 5.1).

5.2 The Basic Idea

A unique symtom of asymmetrical core saturation caused by GIC is pronounced second harmonic (120 Hz) content in the exciting current for a sufficiently long time. Figure 5.2 shows a typical waveform and spectrum of the exciting current taken from a laboratory test. In an actual transmission system, the path that allows GIC to flow in it always consists of some highly inductive elements (e.g.

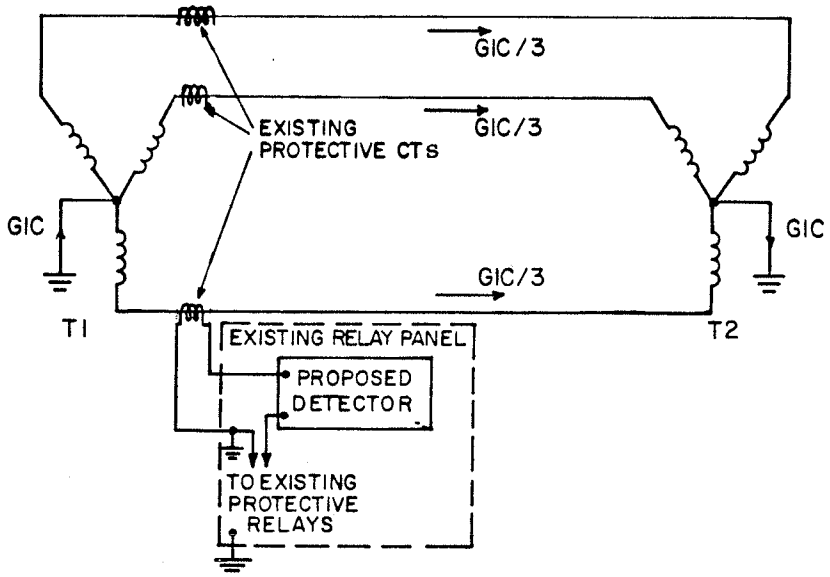

FIGURE 5.1 Arrangements of the proposed detector.

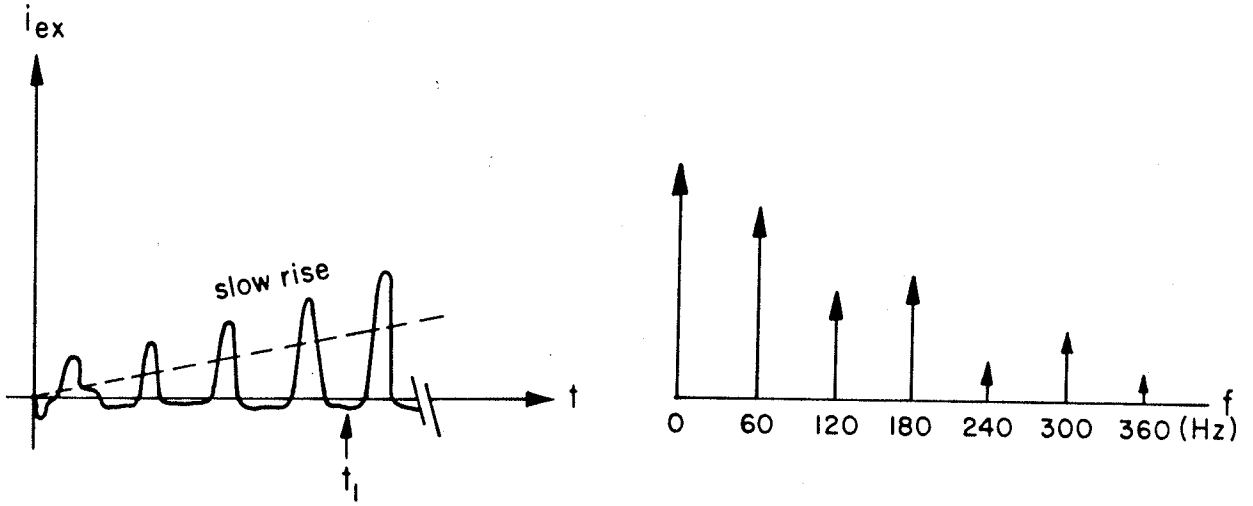

(a) Exciting current waveform

(b) Exciting current spectrum (at time t_1)

FIGURE 5.2 Exciting current under GIC conditions.

the inductances of the high voltage windings of the transformers and the inductance of the transmission line), so the rate-of-rise of GIC in such a path would tend to be slow, and a spectrum close to that of Figure 5.2(b) exists for some time (of the order of minutes).

Hence, the presence of sufficiently high second-harmonic current for a sufficiently long time means two things have occurred in the system: (1) the transformers are in deep asymmetrical core saturation conditions, and (2) a severe GIC is present.

For a typical system as shown in Figure 5.1, the presence of sufficiently high second harmonic current for a sufficiently long time is readily observable at the secondary circuit of the existing relaying CTs located on the high-voltage side of the power transformers. Thus the proposed device, shown in Figure 5.1, can be connected in series with the existing secondary relay circuit to sense the second harmonic current flowing in one phase of the line. This in turn detects the level of asymmetrical core saturation and hence indicates (indirectly) the presence of the GIC in the system.

5.3 Harmonic Currents in the Secondary Relay Circuit

Since the device is to be connected in series with the existing secondary relay circuit, it is perhaps worth examining all the possible sources of generation of harmonic currents that are to appear in the secondary relay circuit under various operating conditions.

TABLE 5.1: Possible Sources of Current Harmonics in the Secondary Circuit of Relaying CTs on the Line Side of Power Transformers.

Source	Harmonic	Magnitude	Duration
CT nonlinearity	odd	negligible	continuous
Transformer inrush	odd & even	high	severalseconds
CT saturation symmetrical fault	odd	low	fault clearing time
CT saturation asymmetry fault	odd & even	low	fault clearing time
HVDC System nearby	odd	low	continuous
CT saturation due to GIC	odd & even	low	as long as GIC
Power transformer saturation due to GIC	odd & even	high	as long as GIC

Table 5.1 shows other sources of even harmonic currents, including in each case second harmonic current. The other occurrence that leads to high second harmonic content is transformer inrush, but discrimination can be accomplished on the basis of time duration since GIC is sustained for much longer times than inrush.

Figure 5.3 shows the proposed level and time duration settings of the device. The x% and y cycles in Figure 5.3 are not fixed values but are system dependent. The values of x and y should be derived from system studies based on system parameters and transformer data obtained from the manufacturers.

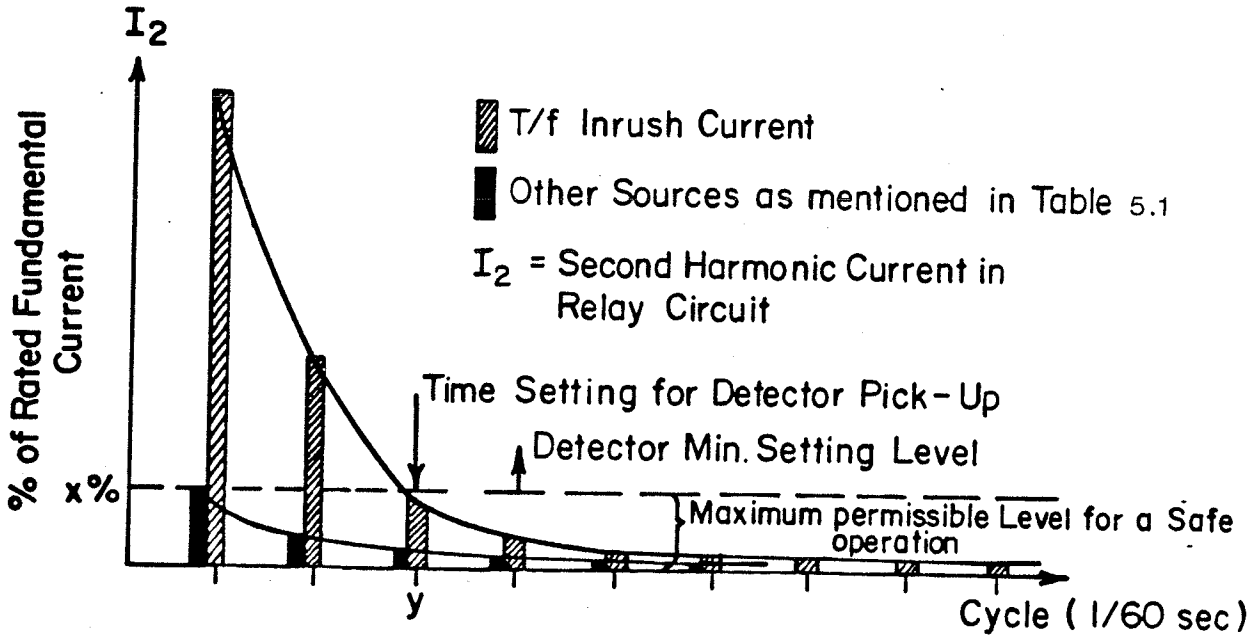

FIGURE 5.3 Proposed level and time settings of the detector.

5.4 Device Implementation

The principal current that flows in the secondary relay circuit under normal operating conditions is the fundamental rated load current. It is very likely that GIC-induced 2nd harmonic current is lower than the fundamental current (Note that the fundamental current also increases for a typical system if GIC $\neq$ 0). A transducer must therefore, be designed to produce sufficient voltage output from the GIC-induced 2nd-harmonic current while suppressing the fundamental component as well as other current harmonics which may be present: See Table 5.1. Moreover, the transducer must not saturate under all operating conditions.

The constructed transducer circuit that meets these requirements is shown in Figure 5.4. The toroidal core in Figure 5.4 offers the best magnetic efficiency of all possible core configurations since it has a uniform cross-sectional area and no air gap. The high turns ratio of the toroidal CT ensures sufficient voltage output while offering a very low input impedance as seen by the secondary relay circuit. Because of the absence of an air gap in the toroidal core, the transducer may saturate under very high level GIC or in-zone fault conditions. To prevent this from occuring, a 120-Hz parallel-tuned circuit is added. The parallel tuned circuit presents a very low burden to the toroidal CT at fundamental frequency and frequencies above 180 Hz . A voltage limiter is added to absorb transient spikes and also is a back-up to prevent saturation of the core.

Figure 5.5 shows the results obtained from primary injection tests on the transducer circuit. True RMS meters were used to monitor the I_p and V_o .

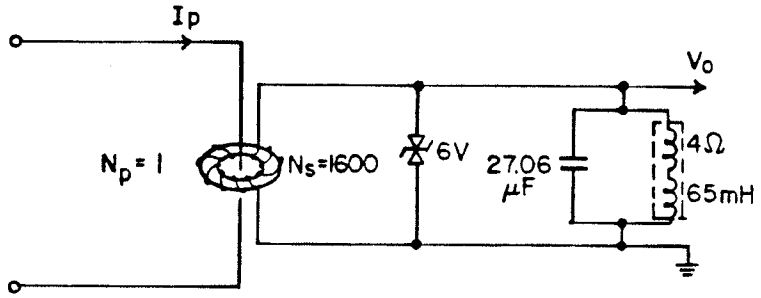

FIGURE 5.4 A Transducer circuit

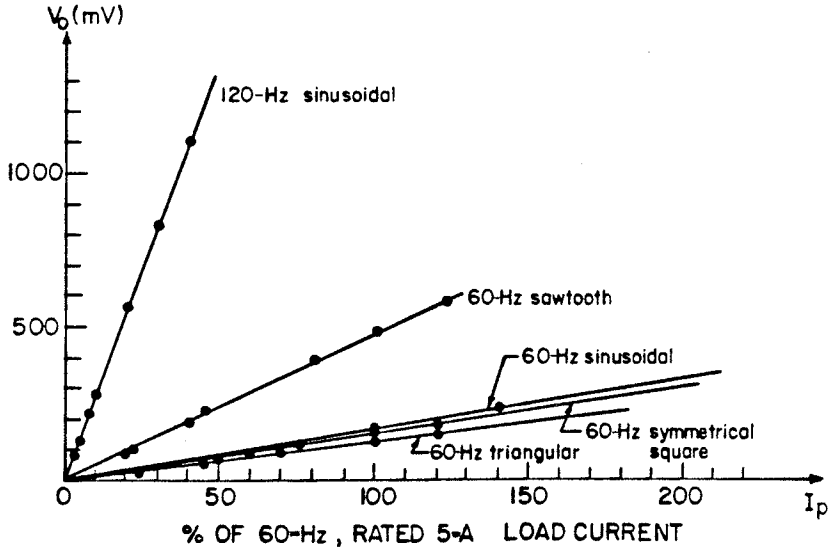

FIGURE 5.5 True rms I_p versus true rms V_o for circuit in Figure 5.4.

The tranducer responds linearly even with I_p = 100% purely sinusoidal 120 Hz for which V_o = 2.699 volts (not shown in Figure 5.5). Several waveforms were included to further check the linearity of the circuit. The results in Figure 5.5 indicate that the transducer in Figure 5.4 can be regarded as a linear device and can be calibrated to measure the magnitude of the second harmonic current in the line.

Figures 5.6 and 5.7 show a single-phase overall block diagram of the device and its detailed circuitry respectively. The output V_o from the tranducer is fed into an amplifier and then into three successive Biquad filters[42,43]. The Biquad filter is an easily tuned and stable device which ensures reliability and stability. The second harmonic current from the last stage of the filter circuit is then rectified using a full-wave rectifier.

In the final stages the second harmonic amplitude setting is defined, say 5% of the load fundamental current level, and its critical duration is defined, say 5 seconds. This last setting is to override transformer inrush.

5.5 Testing

5.5.1 Laboratory

Figure 5.8 shows two aspects of the initial testing.

With switch S1 in position 2, the sensitivity of the device to second harmonic current content was determined. The calibration curve is shown in Figure 5.9. The second function generator was used to inject a very high 60-Hz component to ensure that this did not

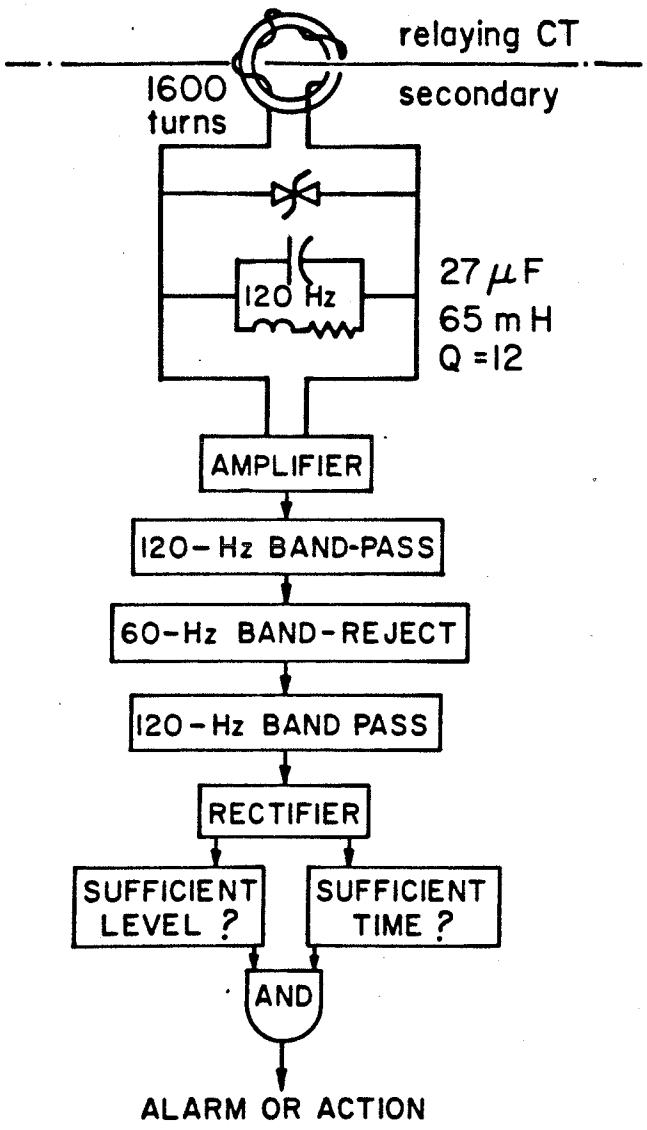

FIGURE 5.6 Detection scheme.

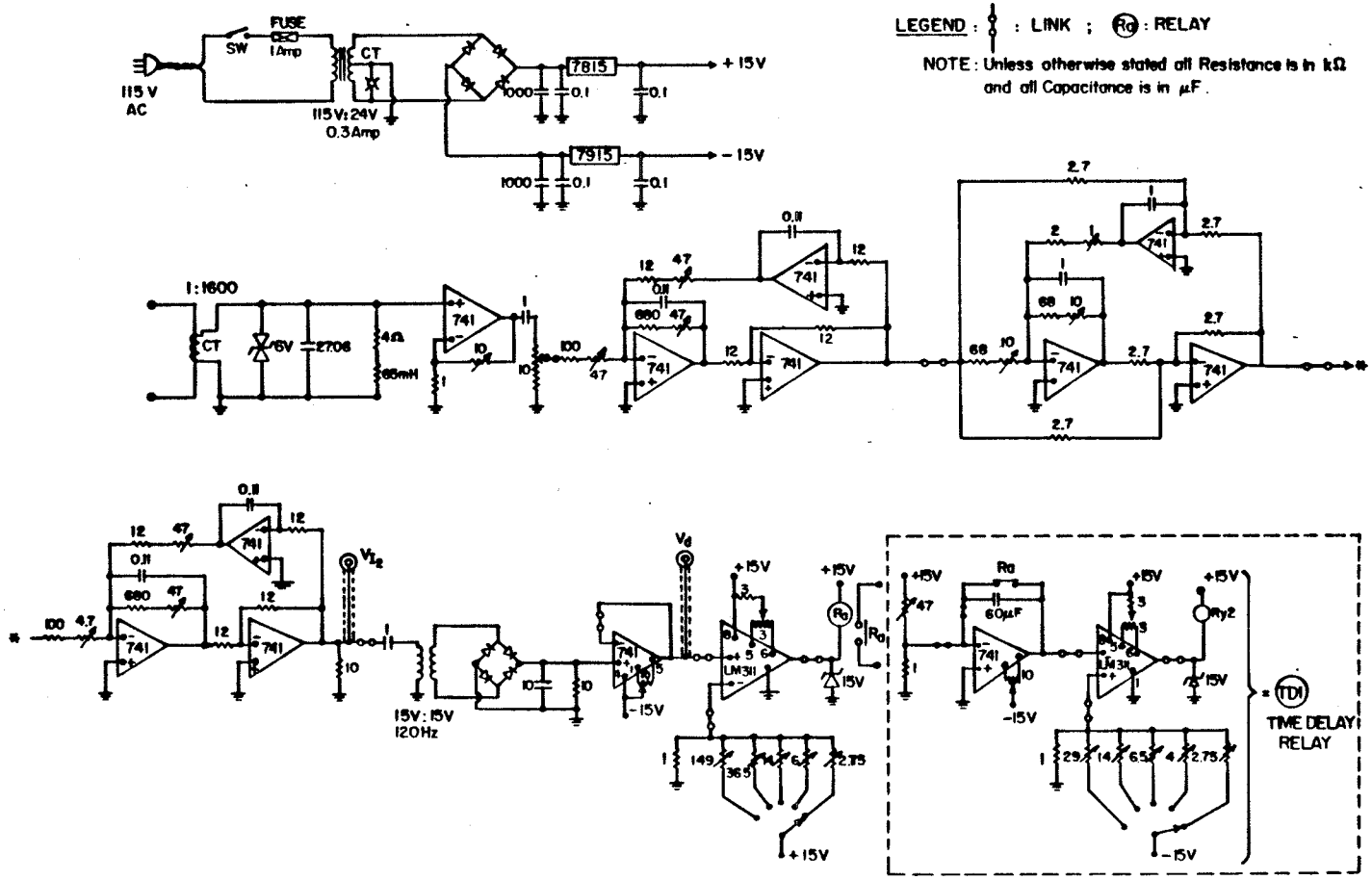

FIGURE 5.7 Detailed circuitry of the detector.

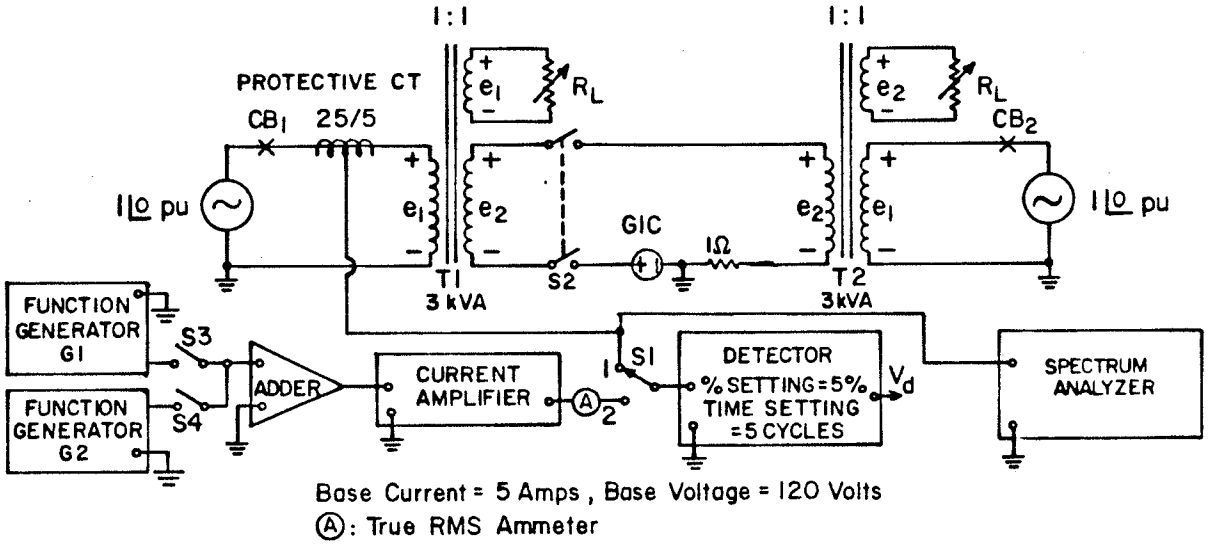

FIGURE 5.8 Test set-up for the detector.

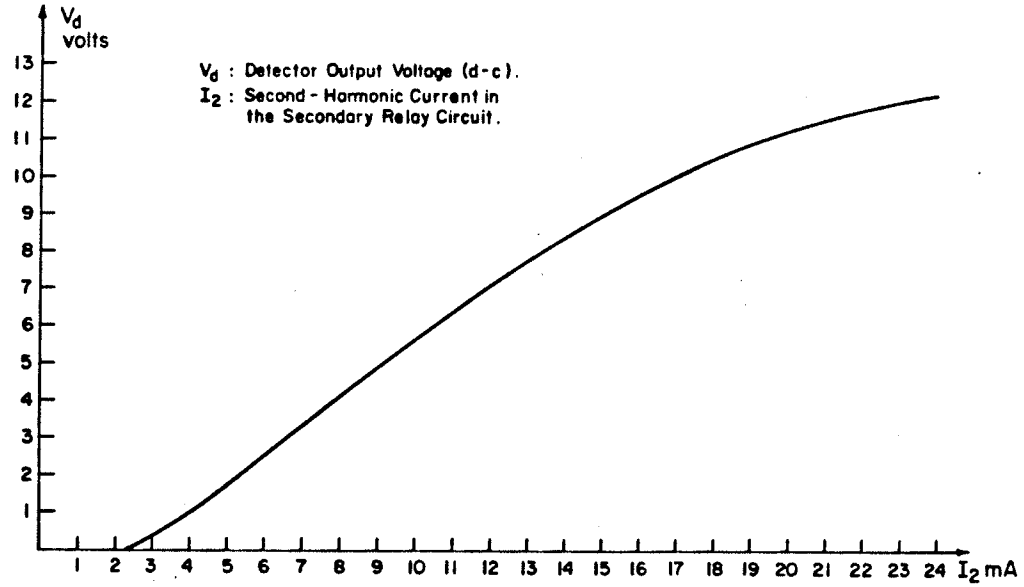

FIGURE 5.9 Input-output characteristic curve of the detector.

affect the output even though the 120-Hz component was very small. The observation was that the 60-Hz current had no detectable effect.

With switch S2 in position 1, a situation closer to reality was simulated, and, in fact, it was this circuit (except that all three phases were used) that lead to the idea initially. As expected, when the GIC series dc source was energized, a detector output appeared.

Table 5.2 shows other conditions simulated. In each case, the detector functioned as expected.

5.5.2 Field

On January 15, 1982, the device was installed in a secondary relaying circuit from the high side of an autotransformer at the Winnipeg end of the 500-kV Winnipeg to Duluth transmission line. The device dc output voltage V_d was fed to one channel of a continuously running chart recorder. The other channel was connected to a direct measurement scheme[15]: a current shunt in the transformer neutral. On February 2, 1982, there was a severe GIC storm. The device responded about three times, but only when the transformer neutral GIC was so severe that the GIC channel pen was driven off-scale.

Since then, two changes have been made: the second-harmonic detector sensitivity has been increased four-fold, and the GIC channel sensitivity has been decreased two-fold.

On March 2, 1982, there was a moderate GIC storm, and the detector responded as expected. Simultaneous recordings of GIC and V_d (i.e. detector dc output voltage which is a function of 2nd-harmonic current I_2 in the secondary relay circuit; see calibration curve in Figure 5.9), as recorded by the detector from 02:00 to 11:00

TABLE 5.2: Test Results of the Set-Up in Figure 5.8.

No.	Case Description	Detector Status
	S1 in position 2, S3 closed, S4 open	
1	G1 = 60-Hz square wave, A = 1.2 pu	No Pick-Up
2	G1 = 60-Hz triangular wave, A = 1.2 pu	No Pick-Up
3	G1 = 60-Hz sawtooth, A = 1.2 pu	No Pick-Up
	S1 in position 2, S3 and S4 closed	
4	G1 = 60-Hz sinusoidal, G2 = 120-Hz sinuisoidal $A = [(98\%\ G1)^2 + (20\%\ G2)^2]^{\frac{1}{2}} = 1$ pu	Pick-up
	S1 in position 1	
5	S2 and CB2 open, $R_L = 0$, CB1 on and off many times	No Pick-Up
6	S2, CB1 and CB2 closed, $R_L = 0$, GIC = 0.12 pu	Pick-Up
7	S2, CB1 and CB2 closed, $R_L = 1.0$ pu, GIC = 0.12 pu	Pick-Up
8	S2, CB1 and CB2 closed, $R_L = 1.0$ pu, GIC = 1.0 pu	Pick-Up

(Manitoba Standard Time) on March 2, 1982, are displayed in Figure 5.10.

In Figure 5.10, some typical GIC peak values (marked with the symbol as ∇) and their corresponding V_d values (marked with Δ) are selected in order to form Table 5.3 for easy reference. Included in Table 5.3 are the RMS values of I_2 and I_2^S . Note that I_2 is the 2nd-harmonic current in the secondary relay circuit and is derived from the calibration curve in Figure 5.9. Where as I_2^S is the high-voltage line-side 2nd-harmonic current and is also readily computed using the expression $I_2^S = nxI_2$, where $n = 2000/5$ is the turn ratio of the CT to which the detector was connected.

Figure 5.10 shows that the correlation between the occurrence of the GIC activity and that of the pronounced 2nd-harmonic current is excellent. Since the installation of the detector, this GIC/2nd-harmonic current correlation has been checked very well whenever a GIC storm occurred.

Figure 5.10 indicates that the 2nd-harmonic current in the system under a GIC condition is sufficiently high and is detectable.

A closer inspection of Figure 5.10 or Table 5.3 reveals that the relationship of the magnitude of the 2nd-harmonic current and that of the transformer-neutral GIC is quite complicated. For example, GIC = 28.0 A and 54.0 A (see cases 5 and 6 in Table 5.3) give I_2 greater than 24.0 mA (the symbol ">" in Table 5.3 means "greater than"). While on the other hand, GIC = 51.0 A (see case 9) gives I_2 = 22.8 mA . Similar observation applies to cases

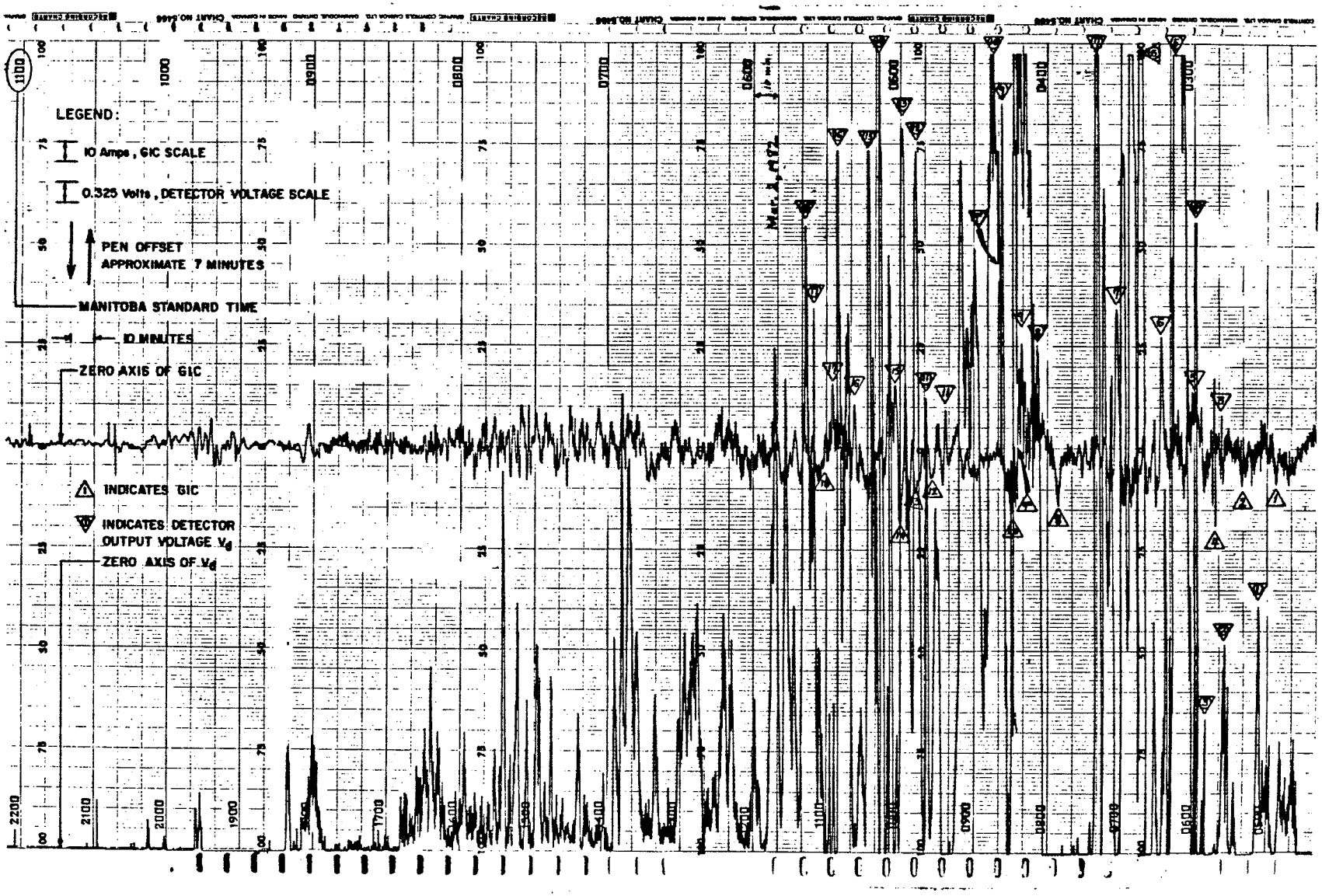

FIGURE 5.10 Correlation between GIC in transformer neutral and 2nd-harmonic current in the secondary relay circuit. Measured at Dorsey station on March 2, 1982.

TABLE 5.3: GIC and 2nd-harmonic current data (March 2, 1982), derived from Figures 5.10 and 5.9.

Case	Manitoba Std. Time	GIC (A)	V_d (V)	I_2 (mA,rms)	I_2^S (A, rms)
1	02:26	-18.0	3.97	7.8	3.12
2	02:40	-18.1	3.35	7.0	2.80
3	02:48	16.0	2.15	5.5	2.20
4	02:52	-38.0	10.14	17.2	6.88
5	03:00	28.0	>12.80	>24.0	>9.60
6	03:14	54.0	>12.80	>24.0	>9.60
7	03:32	68.0	>12.80	>24.0	>9.60
8	03:55	-28.0	9.75	16.4	6.56
9	04:11	51.0	12.03	22.8	9.12
9*	04:13	0	9.46	15.9	6.36
10	04:14	-32.0	>12.80	>24.0	>9.60
11	04:42	18.0	7.28	12.3	4.92
12	04:47	-14.0	11.25	20.0	8.00
13	04:54	-20.0	11.64	21.3	8.52
14	05:00	-36.0	>12.80	>24.0	>9.60
15	05:02	30.0	11.25	20.0	8.00
16	05:18	21.0	11.25	20.0	8.00
17	05:28	31.0	8.71	14.6	5.84
18	05:32	-10.0	10.04	17.0	6.80

NOTE: $I_2^S = n \times I_2$, where n is CT ratio,
here $n = 2000/5 = 400$.

15, 16 and 17. Aspens and Akasofu[44] in their investigation on 3rd-harmonic current in tertiary windings of power transformer under GIC conditions, have presented similar results for the GIC/3rd-harmonic current correlation. But this point has not been mentioned and explained by them in their paper. One reason for such a complicated relationship is no doubt due to the fact that GIC is not a pure dc. The other is that the biasing flux, which is due to the GIC, tends to lag behind the GIC because of the hysteresis effect of the iron core.

Another interesting observation, that derived from Figure 5.10 and Table 5.3, is case 9* which gives I_2 = 15.9 mA for GIC = 0 A. This is, of course, due to the fact that the biasing flux in the iron does not go to zero (because of the remanence effect of the iron) though GIC goes to zero (because the actual GIC is not a pure dc). The discussion suggests that the more appropriate approach for detecting the asymmetrical core saturation is by measuring directly the 2nd-harmonic current content in the system. Thus, the method of direct measuring the transformer-neutral GIC seems to be less attractive from the asymmetrical-core-saturation viewpoint.

At present, the detector was set at its highest sensitive range. From Table 5.3, it is clear that the 2nd-harmonic current I_2 of RMS value greater than 24.0 mA has occurred very frequently and a higher I_2 current (say above 100 mA) would perhaps be of paramount interest because its presence infers deep asymmetrical core saturation which could lead to a system operating problem.

In order to show that the rate-of-rise of 2nd-harmonic current is slow and that the current also persists for a sufficiently

long time, a Hewlett-Packard dual-channel high-speed recorder was used to monitor the GIC and V_d . The recorder is automatically started up with a speed 1 mm/sec upon receiving a remote triggering signal from the detector whenever the detector dc output voltage V_d exceeds 1 volt.

Figure 5.11 shows one of the typical results recorded under a GIC condition. Notice that the time required for increasing V_d from 1 volt to its first peak value is approximately 1 minute 50 seconds. Subsequent field results reveal similar observation, that is, the time required for increasing V_d from 1 volt to its first peak is in the order from 1 to 2 minutes.

It can also be seen from Figure 5.11 that the 2nd-harmonic current persists for a time period for about 7 minutes 5 seconds (from 1 volt pick-up to 1 volt drop-off). Of course, I_2-persistence periods longer than 7 minutes 5 seconds are very common (this can be seen from Figure 5.10). Subsequent results from the field also reveal this observation. They are, however, not to be presented here because these recording charts are too lengthy to be formed into a figure.

Since the installation of the detector, the device has been performing satisfactorily. The results always show that the GIC/2nd-harmonic-current correlation is excellent. This fact suggests that the detection of asymmetrical core saturation, caused by near-dc GIC, by magnitude and time discrimination of 2nd-harmonic current sensed in the line CTs would appear to be a practical, indirect method.

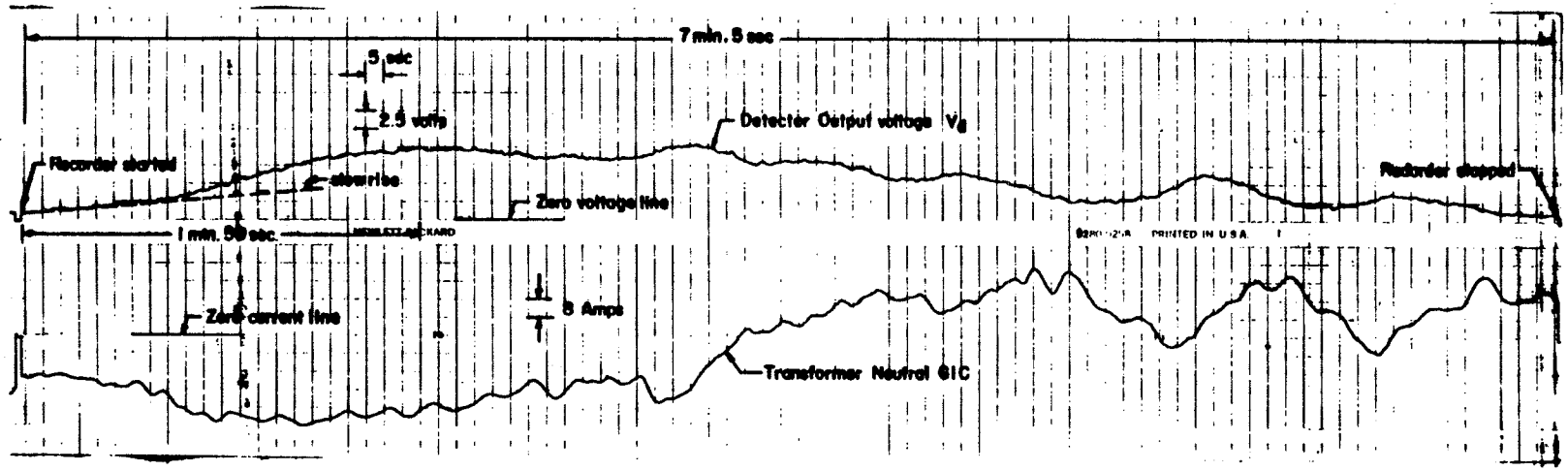

FIGURE 5.11 High-speed recording chart showing the rate-of-rise of 2nd-harmonic currents (measured at Dorsey station on July 14, 1982).

CHAPTER VI

CONCLUSIONS

6.1 General Conclusion

The central topic of this thesis has been the examination of localized overheating in structural metal parts in power transformers due to asymmetrical core saturation caused by GIC. The power transformers addressed here are designed to specific Standards. This means that they must operate satisfactorily under all permissible operating conditions (including permissible overexcitation and overloading as recommended in References 45 and 10) without exceeding a specified temperature rise or causing any localized overheating problem. For such a transformer, it is concluded that:

> Power transformer overheating of structural metal parts due to asymmetrical core saturation caused by GIC, is extremely unlikely. If GIC were to increase indefinitely (an unrealistic assumption), overheating in the windings (due to high exciting current) would present a dominant heating problem well before overheating in structural parts. For a power transformer with typical temperature ratings of normal: 90 °C, alarm: 110 °C, and trip: 140 °C, the temperature relaying scheme would be adequate for transformers in GIC areas.

This conclusion is based on extensive experimental evidence and detailed follow-up theoretical explanations. Detailed conclusions

will be given in the next section in order to substantiate the conclusion made above.

6.2 Detailed Conclusions

(1) The numerical methods used in the field calculations are not new. What is new is the application of available methods to the detailed investigation of a nonlinear field problem: a problem which has received very little attention and whose physical nature has not been explored in detail. The success of nonlinear field calculations for such an investigation necessitates

   (a) the use of the high order elements;

   (b) the modelling of the B-H characteristic to high fidelity;

   (c) the use of a vector-potential field formulation (resulting in simplicity of the finite-element algorithm);

   (d) the use of the fast convergence Newton-Raphson iterative process; and

   (e) the skillful decomposing of the total field into two components so that the field due to the iron itself can be examined in detail.

(2) The process of magnetization of a closed iron circuit with concentrated magnetizing winding is nonuniform. This nonuniform magnetizing process becomes increasingly pronounced when the magnetizing ampere-turns is high. Under

such a condition, the effect of the equivalent volume current density $\bar{J}_v$ (defined as $\nabla x\bar{M}$) on the magnetic field behaviour of the iron circuit becomes increasingly significant. Consequently, the iron spills less iron flux when the magnetizing ampere-turns is high.

(3) The term "deep saturation" is defined in Chapter III, page 62. For the fields <u>outside</u> the iron circuit excluding the magnetizing-winding region, it is shown that when the iron circuit is below a deep saturation condition, the iron field $\bar{B}^m$ is dominant, while on the other hand, the magnetizing-current field $\bar{B}^c$ becomes increasingly dominant when the iron is in a deep saturation condition. Thus, the rate-of-rise of the magnitude of the total field $\bar{B}$ (with respect to the magnetizing current) diminishes to a near constant which is solely determined by that of the magnetizing-current field $\bar{B}^c$ when the iron is deeply saturated.

(4) The iron surrounded by the concentrated magnetizing winding saturates before other parts of iron when deep saturation approaches. Though the iron in this region has been saturated, it does not behave like an "air core" because $\bar{H}^c$ always interacts with $\bar{H}^m$ irrespective of how deeply the iron is magnetized.

(5) Under the deep saturation conditions, the saturation curve that is derived from Magnetic Circuit Theory, should no longer be applied to a study of a closed iron circuit. To do so results in overestimation of the magnetizing current

This point has been illustrated in Chapter IV, page 58.

(6) The magnitude of the total field $\bar{B}$ is highly nonuniform in the conductor region. In certain areas in the conductor region, $\bar{B}^m$ interacts with $\bar{B}^c$ resulting in $B > B^c$ (note that $\bar{B} = \bar{B}^c + \bar{B}^m$). On the other hand, in other areas in the conductor region, $\bar{B}^m$ interacts with $\bar{B}^c$ to yield $B < B^c$. Thus, in studying the conductor eddy-current loss, one should take into acount the vector cancelling effect due to $\bar{B}^m$ in certain areas of the conductor region.

(7) When an operating power transformer with concentrated windings is under a GIC condition, the nonlinearity of the iron is important. The biasing flux B^I_{dc} should not be derived directly from the magnitude of GIC (i.e. point p $\neq$ point Q in Figure 4.11, page 101).

(8) When the GIC has caused the iron within the magnetizing winding to saturate, any further increase in GIC does not cause further increase in the biasing flux. To put this more simply, this means that the biasing flux "saturates". Hence, the "saturated" biasing flux increases very little even if GIC increases to a much higher level.

(9) The "saturation" of the biasing flux and the nonlinearity of the iron cause a <u>moderate</u> increase in the magnetizing current under GIC conditions (see Figure 4.9, page 96). Should the "air core" concept be applied, the magnetizing

current for the transformer in this study would be: $\frac{120}{2 \times 60 \times 0.5 \times 10^{-3}} = 636.6$ A ! which is approximately 28 times of the exciting current for GIC = 13 A . (The air-core inductance of the winding is 0.5 mH which was obtained when the iron core was taken apart).

(10) The "saturation" of the biasing flux, the nonlinear behaviour of the iron, and the peculiar deep-saturation phenomenon of the iron cause the ac stray field in air near the iron to show almost no sign of increasing (see Figure 4.9, page 96).

(11) The stray field of a power transformer due to asymmetrical core saturation is completely different from that due to overexcitation. For the case of deep asymmetrical core saturation, the stray field is a single-sided waveform containing a dc component. The effect of this dc component on eddy-current loss in solid iron plates is not the subject of this investigation since this has been examined in detail by Woods[40].

(12) The measure of power loss for a power transformer with no load under GIC conditions must be exercised with great care. The use of CTs and a conventional dynamo-type wattmeter is not appropriate for performing such a measurement. This is due to the fact that the exciting current contains very high harmonic currents, and also the power factor is extremely low.

6.3 Conclusion Regarding the Saturation Detector

A device for detecting the level of asymmetrical core saturation of power transformers and hence indirectly indicating the presence of GIC has been developed and put under test on the Manitoba Hydro System. Field results show that the GIC/2nd-harmonic correlation is excellent. It can thus be concluded that the detection of near-dc GIC by magnitude and time discrimination of second harmonic current sensed in the line CTs would appear to a practical, indirect method. Furthermore, the simplicity and the ease of installation of this indirect device makes it perhaps more attractive than GIC direct detection schemes.

REFERENCES

1. EPRI Research Project 1205-1, Phase 1 Report, "Investigation of Geomagnetically-Induced Currents in the Proposed Winnipeg-Duluth-Twin Cities 500 kV Transmission Line", June 15, 1979.

2. Boteler, D. H. Watanabe, T., Shier, R. M., and Horita, R. E., "Characteristic of Geomagnetically-Induced Currents in the B.C. Hydro 500 kV System", IEEE Trans., vol. PAS-101, pp. 1447-1456, 1982.

3. Albertson, V. D. and Van Vaelen, J. A., "Electric and Magnetic Fields at the Earth's Surface Due to Auroral Currents", IEEE Trans., vol. PAS-89, pp. 578-584, 1970.

4. Albertson, V. D., Thorson, J. M., and Miske, S. A., "The Effects of Geomagnetic Storms on Electrical Power System', IEEE Trans., vol. PAS-93, pp. 1031-1037, 1974.

5. Albertson, V. D., Thorson, J. M., Clayton, R. E., and Tripathy, S. C., "Solar-Induced-Currents in Power Systems: Causes and Effects", IEEE Trans., vol. PAS-92, pp. 471-477, 1973.

6. Albertson, V. D., Kappenman, J. C., Mohan, N., and Skarbakka, G. A., "Load Flow Studies inthe Presence of Geomagnetically-Induced Currents", paper no. F79-702-2 presented at the PES Summer Power Meeting, Vancouver, Canada, July 1979.

7. Mohan, N., Kappenman, J. G., and Albertson, V. D., "Harmonics and Switching Transients in the Presence of Geomagnetically-Induced Currents", paper no. F79-694-1 presented at the PES Summer Power Meeting, Vancouver, Canada, July 1979.

8. Kappanman, J. G., Albertson, V. D., and Mohan, N., "Current Transformer and Relay Performance in the Presence of Geomagnetically-Induced Currents", paper no. 80 SM646-0, presented at the PES Summer Meeting, Minneapolis, Minnesota, July 1980.

9. Mohan, N., Albertson, V. D., Speak, T. J., Kappenman, K. G., and Bahrman, M. P., "Effects of Geomagnetically-Induced Currents on HVDC Converter Operation", IEEE Trans., vol. PAS-101, pp. 4413-4418, 1982.

10. ANSI C57.92 (1962), "Guide for Loading Oil-immersed Distribution and Power Transformer".

11. Alexander, G. W., Corbin, S. L., and McNutt, W. J., "Influence of Design and Operating Practices on Excitation of Generator Step-Up Transformers", IEEE Trans., vol. PAS-85, pp. 901-909.

12. Aubin, J. and Bolduc, L., "Behaviour of Power Transformers Submitted to Solar Induced Currents", paper presented to CEA of IREQ, Toronto, March 15, 1978.

13. Takeda, G., "Solar Induced Currents and Heating of Metallic Parts", Technical Report submitted to Manitoba Hydro, Winnipeg, August 1979.

14. Hammond, P., "Leakage Flux and Surface Polarity in Iron Ring Stampings", Proc. I.E.E., Monograph No. 115, 102C, pp. 138-147.

15. Roik, J. N., "Dorsey Station 500 kV Protection", paper presented to CEA, Toronto, March 16, 1981.

16. Silvester, P. P., "The Fundamental Equations of Electric and Magnetic Fields", in Finite Elements in Electrical and Magnetic Field Problems, Chari, M. V. K. and Silvester, P. P. (eds.), pp. 48, New York: Wiley & Sons, 1980.

17. Stevens, W. N. R. and Wexler, A., "MANFEP Programmer's Manual", TR80-3, Department of Electrical Engineering, The University of Manitoba, 1980.

18. Tay, H. C. and Swift, G. W., "An Indirect Method of Detecting GIC", Canadian Electrical Association Spring Meeting, Montreal, March 15, 1982.

19. Stratton, J. A., Electromagnetic Theory, McGraw-Hill, 1941, Section 4.1, pp. 225-226.

20. Hague, G., The Principles of Electromagnetism Applied to Electrical Machines, New York: Dover Publications, 1962, pp. 280-282.

21. Zienkiewicz, O. C., The Finite Element Method in Engineering Science, 2nd-Edition, McGraw-Hill, 1971, Chapter 3, pp. 33-47.

22. Simkin, J. and Trowbridge, C. W., "On the Use of the Total Scalar Potential in the Numerical Solution of Field Problems in Electromagnetics", Int. J. Num. Meth. Eng., vol. 14, pp. 423-440, 1979.

23. Wexler, A., Finite Elements for Technologists, Lecture notes for a course given in the Polytechnic of Central London, Chapter 6, pp. 21-26, 1974.

24. Silvester, P. and Chari, M. V. K., "Finite Element Solution of Saturable Magnetic Field Problems", I.E.E. Trans., vol. PAS-89, pp. 1642-1651, 1970.

25. Silvester, P., Cabayan, H. S., and Browne, B. T., "Efficient Techniques for Finite Element Analysis of Electric Machines", IEEE Trans., vol. PAS-92, pp. 1274-1281, 1973.

26. De Boor, C., A Practical Guide to Splines, New York: Springer-Verlag, 1978, Chapter IV, pp. 49-59.

27 Smith, R. J., Circuits, Devices, and Systems, Second-Edition, Wiley and Sons, 1971, pp. 483.

28. As Reference 23, Chapter 6, pp. 15-21.

29. Friedman, M., Richards, D. J., Stevens, W. N. R., and Wexler, A., MANFEP User's Manual, TR79-1, Department of Electrical Engineering, The University of Manitoba, 1979, p. 17.

30. Kreyszing, E., Advanced Engineering Mathematics, Fourth-Edition, Wiley and Sons, 1979, pp. 419-421.

31. Stroud, A. H. and Secrest, D., Gaussian Quadrature Formulas, Prentice-Hall Inc., Englewood Cliffs, N.J., 1966, pp. 40-44.

32. Zienkiewicz, O. C., Lyness, J., and Owen, D. R. J., "Three-Dimensional Magnetic Field Determination Using a Scalar Potential — A Finite Element Solution", IEEE Trans. on Magnetics, MAG-13, pp. 1649-56.

33. Stratton, J. A., Electromagnetic Theory, New York: McGraw-Hill, 1941, Section 4.10, pp. 242-243.

34. F. W. Bell Inc., Model 610 Gaussmeter Operating and Maintenance Manual.

35. Emanuel, A. E., "Current Transformer Performance with Steady-State DC Biasing", IEEE Trans. on Magnetic, vol. MAG-16, pp. 1278-1282, 1980.

36. Tudbury, C., "Electromagnetics in Induction Heating", IEEE Trans. on Magnetic, vol. MAG-10, pp. 694-697, 1974.

37. Agarwal, P. D., "Eddy-Current Losses in Solid and Laminated Iron", AIEE Trans., vol. 78, pt.I, pp. 169-181, 1959.

38. Stoll, R. L., The Analysis of Eddy Currents, Oxford University Press, 1974.

39. Lim, K. K. and Hammond, P., "Universal Loss Chart for the Calculation of Eddy-Current Losses in Thick Steel Plates", Proc. I.E.E., vol. 117, (4), pp. 857-864, 1970.

40. Woods, E. J. "Eddy Current Losses in Solid Iron with DC Offset", IEEE Trans, vol. PAS-100, pp. 2241-2248, 1981.

41. Albertson, V. D. and Thorson, J. M., "Power System Disturbances During a K-8 Geomagnetic Storm: August 4, 1972", IEEE Trans., vol. PAS-93, pp. 1025-1030, 1974.

42. Tow. J., "A Step-by-Step Active Filter Design", IEEE Spectrum, vol. 6, no. 12, pp. 64-68, December 1969.

43. Johnson, D. E., Introduction to Filter Theory, Prentice-Hall Inc., Englewood Cliffs, N. J., 1976, Chapter II, pp. 225-257.

44. Aspnes, J. D. and Akasofu, S. I., "Effect of Solar Induced Current on Autotransformer Tertiary Windings", paper no. 81-SM-318-5 presented at the IEEE PES Sumer Meeting, Portland, Oregon, July 1981.

45. ANSI C57.12.00-1973, "General Requirements for Distribution, Power and Regulating Transformers".